Flecker, R., Ducassou, E., Williams, T., and the Expedition 401 Scientists
Proceedings of the International Ocean Discovery Program Volume 401
publications.iodp.org

Site U1385[1]

R. Flecker, E. Ducassou, T. Williams, U. Amarathunga, B. Balestra, M.A. Berke, C.L. Blättler, S. Chin, M. Das, K. Egawa, N. Fabregas, S.J. Feakins, S.C. George, F.J. Hernández-Molina, W. Krijgsman, Z. Li, J. Liu, D. Noto, F. Raad, F.J. Rodríguez-Tovar, F.J. Sierro, P. Standring, J. Stine, E. Tanaka, M. Teixeira, X. Xu, S. Yin, and M.Z. Yousfi[2]

[1] Flecker, R., Ducassou, E., Williams, T., Amarathunga, U., Balestra, B., Berke, M.A., Blättler, C.L., Chin, S., Das, M., Egawa, K., Fabregas, N., Feakins, S.J., George, S.C., Hernández-Molina, F.J., Krijgsman, W., Li, Z., Liu, J., Noto, D., Raad, F., Rodríguez-Tovar, F.J., Sierro, F.J., Standring, P., Stine, J., Tanaka, E., Teixeira, M., Xu, X., Yin, S., and Yousfi, M.Z., 2025. Site U1385. In Flecker, R., Ducassou, E., Williams, T., and the Expedition 401 Scientists, Mediterranean–Atlantic Gateway Exchange. Proceedings of the International Ocean Discovery Program, 401: College Station, TX (International Ocean Discovery Program). https://doi.org/10.14379/iodp.proc.401.105.2025
[2] **Expedition 401 Scientists' affiliations.**

Contents

Keywords
International Ocean Discovery Program, IODP, *JOIDES Resolution*, Expedition 401, Mediterranean–Atlantic Gateway Exchange, Earth Systems Models, Site U1385, Messinian Salinity Crisis, Messinian, Tortonian, Miocene, Pliocene, hemipelagite, precession, Atlantic, Portuguese margin, Principe de Avis Plateau

Core descriptions

Supplementary material

References (RIS)

MS 401-105
Published 7 July 2025

Funded by NSF OCE1326927, ECORD, and JAMSTEC

1. Background and objectives

Site U1385 (37°34.2849′N, 10°7.5616′W) was first drilled during Integrated Ocean Drilling Program Expedition 339 (Figure **F1**) to provide a marine reference section of Pleistocene millennial climate variability. Five holes were cored (Holes U1385A–U1385E) to a maximum penetration of 151.5 meters below seafloor (mbsf) using the advanced piston corer (APC) system (Expedition 339 Scientists, 2013) (Figure **F2**). The record extends to 1.45 Ma (Marine Isotope Stage 47) with an average sedimentation rate of 11 cm/ky (Hodell et al., 2015).

Site U1385 (37°34.0128′N, 10°7.6580′W) was reoccupied during International Ocean Discovery Program (IODP) Expedition 397 (2022) to deepen the sequence to 400 mbsf, just above the Miocene/Pliocene boundary (~5.3 Ma) (Hodell et al., 2023). Five more holes were cored (Holes U1385F–U1385J) ~500 m from the Expedition 339 location (Figure **F2**) using the extended core barrel (XCB) system. During Expedition 397, Site U1385 was part of a four site depth transect designed to capture and reconstruct water mass changes during the Pliocene and Pleistocene (Figure **F3**) (Hodell et al., 2023). Results from Site U1385 demonstrate that the Iberian margin yields long, continuous records of millennial Pliocene–Pleistocene climate variability permitting

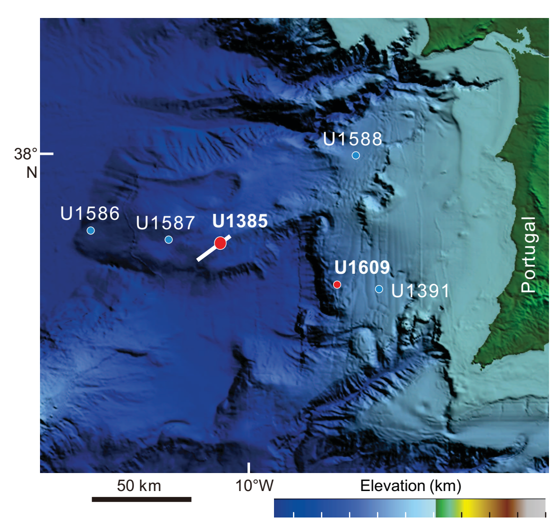

Figure F1. Bathymetric location map, Sites U1385 and U1609 with nearby sites from Expeditions 339 and 397. White line = location of seismic profile in Figure F3.

detailed land–sea comparisons (Hodell et al., 2023). The two deeper water sites, U1587 and U1586, also recovered Late Miocene successions (Hodell et al., 2023).

Expedition 401 used the same Site U1385 designation, coring two holes, U1385K and U1385L. We distinguish between the intervals recovered during the different expeditions by prefixing U1385 with the expedition number if the hole letter is not included: Sites 339-U1385, 397-U1385, and 401-U1385. Holes U1385K and U1385L are located ~20 m east of Expedition 397 Holes U1385I

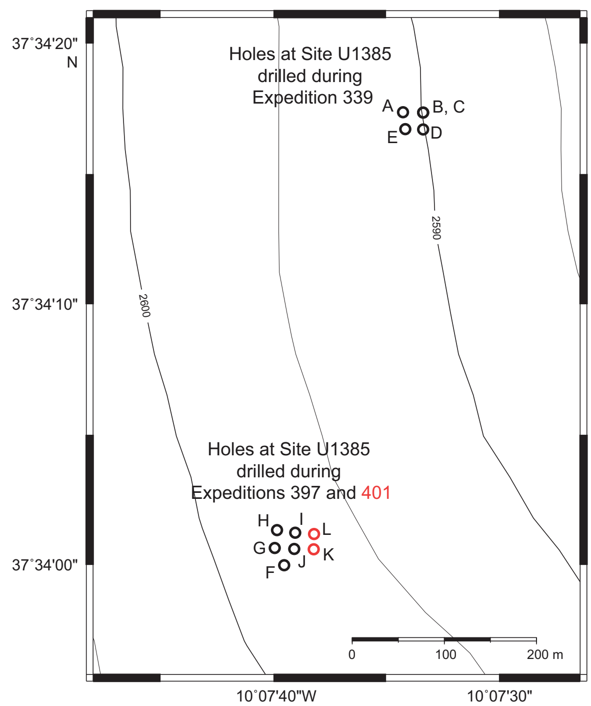

Figure F2. Locations of Site U1385 holes drilled during Expeditions 339 (Holes U1385A–U1385E), 397 (Holes U1385F–U1385J), and 401 (Holes U1385K and U1385L).

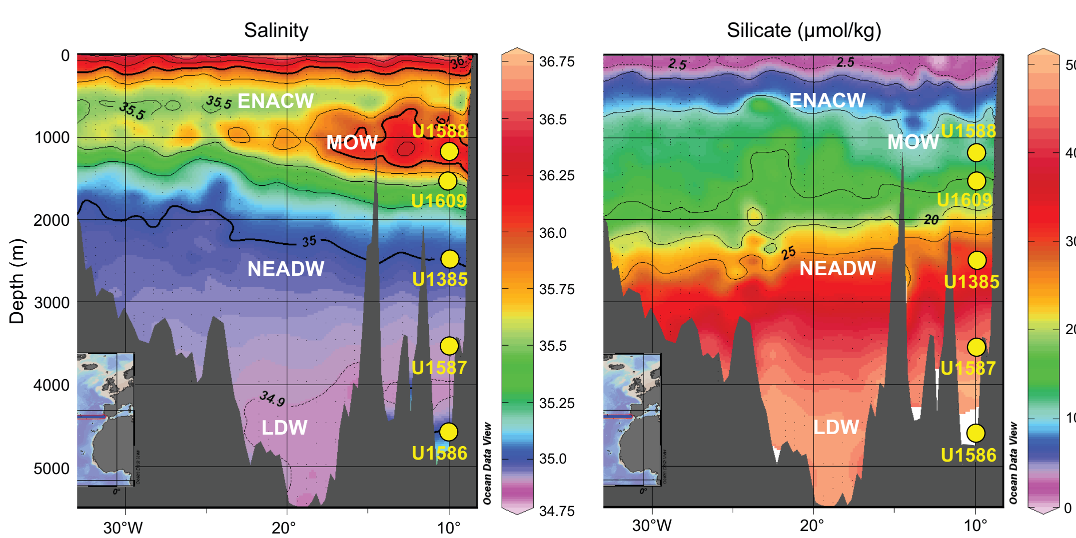

Figure F3. Salinity and silicate profiles on World Ocean Circulation Experiment (WOCE) Line A03 (36°N) showing Sites U1385 and U1609 as well as Expedition 397 site locations on Iberian margin relative to each identified subsurface water mass. Tongue of high salinity water between ~800 and ~1300 m is MOW. High Si (>35 µmol/kg) below 3000 m represents contribution from Lower Deep Water (LDW) sourced from Southern Ocean. Water masses do not have clearly defined boundaries but rather consist of series of core layers bordered by transition (mixing) zones between adjacent layers. ENACW = East North Atlantic Central Water. Figure modified after Hodell et al. (2024a).

and U1385J, respectively (Figure **F2**). The approximate water depth is 2584 meters below sea level (mbsl), determined by precision depth recorder, placing it in the core of Northeast Atlantic Deep Water (NEADW) today (Figure **F3**).

1.1. Objectives

Extending Site U1385's remarkable sediment archive back into the Late Miocene was one of the primary goals of reoccupying this location during Expedition 401. Equivalent-aged sediments recovered at the deeper Site U1587 (Hodell et al., 2023) can be traced upslope on the seismic profile to Site U1385. These Late Miocene sediments at Site U1587 display well-developed precessional cyclicity (Hodell et al., 2024b). However, the poor carbonate preservation at this greater water depth (3480 m) means that high-resolution carbonate-based proxy records cannot be generated (Hodell et al., 2023). The shallower water depth at Site U1385 (2590 m) likely offers better carbonate preservation, making generating these essential proxy records possible.

Site U1385 is the deepest site cored during Expedition 401 (Figure **F3**). It is located on an elevated ridge, minimizing the chances of disturbance by downslope transport. In combination with Site U1609 and the two deeper water Expedition 397 sites, U1587 and U1586 (Figure **F1**), the Late Miocene records from Site U1385 complete a depth transect equivalent to the Pliocene–Pleistocene transect generated by Expedition 397 (Figure **F3**). The objective was to drill a single hole (U1385K) to recover the deeper part of the section below Site 397-U1385 to the late Tortonian (Figure **F4**) by washing down to 385 mbsf (just 15 m above 400 mbsf) and then recovering a further 503 m (30 + 473 m) of sediment to reach the drilling target depth of 873 mbsf. However, negligible recovery over the Miocene/Pliocene boundary interval in Hole U1385K meant that an additional hole, U1385L, was required to obtain the desired record.

The specific objectives of Site 401-U1385 were as follows:

- To document the nature, amplitude, and pacing of climate cycles in the Atlantic before, during and after the Messinian Salinity Crisis and
- To reconstruct water mass variability during this time period.

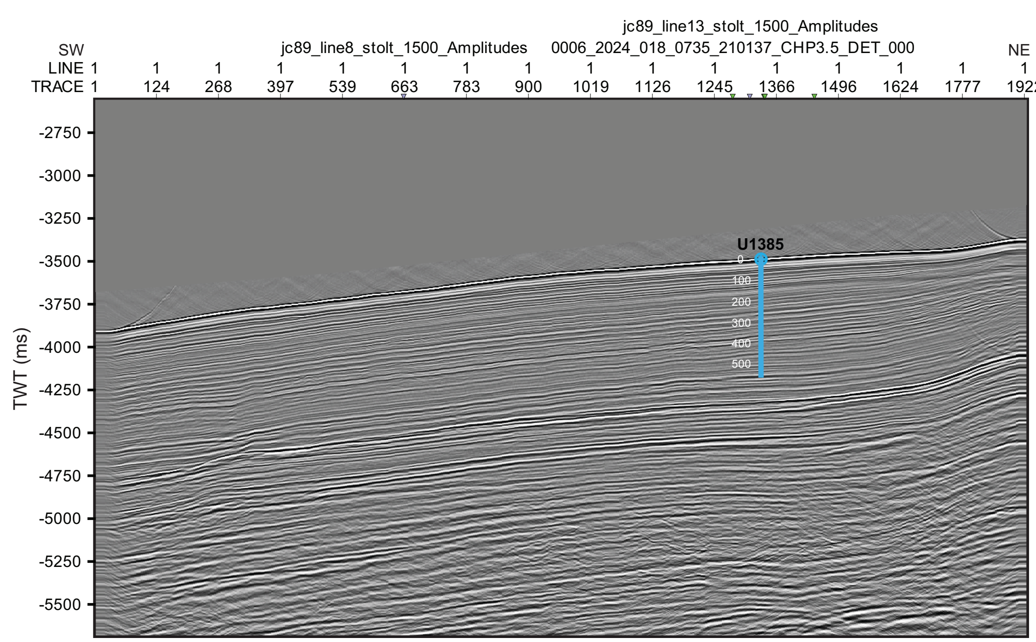

Figure F4. Seismic Line JC89-9 crossing Site U1385 penetration during Expeditions 339, 397, and 401 to ~4.2 s two-way traveltime (TWT). See figure 12 in Hodell et al. (2022) for cross-line and site map.

2. Operations

Holes U1385K and U1385L were cored after drilling down to start coring a little shallower than the 400 mbsf reached at this site during Expedition 397.

2.1. Hole U1385K

The 154 nmi voyage from Site U1610 to Site U1385 (37°34.0099′N, 10°7.6370′W) took 12.8 h at an average speed of 12.0 kt. We lowered the thrusters at 1622 h on 12 January 2024 and switched to dynamic positioning mode at 1652 h. Site U1385 was cored to 151 mbsf during Expedition 339 in 2011 and to 400 mbsf during Expedition 397 in 2022. The APC/XCB bottom-hole assembly (BHA) was assembled with a polycrystalline diamond compact (PDC) bit and lowered toward the seafloor, and a pipe-cleaning pig was pumped down to clean the inside of the drill pipe. The ship was positioned 20 m east of Hole U1385J, with the seafloor tagged at 2595.4 mbsl.

Hole U1385K was started at 0035 h on 13 January and was drilled ahead, reaching 385.0 mbsf at 1615 h. The center bit was retrieved, and we started coring. Cores 2X–6X returned nearly empty, so we ran the bit deplugger to ensure that the bottom of the BHA was free from loose sediment that may have entered during the preceding drill down. Recovery improved for subsequent cores, and we continued coring through Core 21X at 1035 h on 15 January, having reached the age target of 8 Ma. Cores 2X–21X penetrated from 385.0 to 552.5 mbsf and recovered 127.9 m (76.4%) (Table **T1**). We pulled up the pipe, clearing the seafloor at 1328 h on 15 January and ending Hole U1385K.

2.2. Hole U1385L

The ship was offset 20 m north, and we started Hole U1385L at 1455 h on 15 January 2024, drilling ahead without coring to 376 mbsf. Coring began at 0330 h on 16 January, and Cores 2X–8X penetrated from 376.0 to 443.9 mbsf, recovering 58.4 m (86.1%) (Table **T1**). We stopped coring at 1645 h because of the high wind and wave conditions forecast for the evening and next day. The bit cleared the seafloor at 1835 h and was pulled up to 332 mbsl while the ship began waiting on weather. After coring Hole U1385K, we had a choice between going directly to the next site or staying to core Hole U1385L; we prioritized collecting core from Hole U1385L, knowing that it would mean waiting on weather the following day.

Table T1. Core summary, Site U1385. DRF = drilling depth below rig floor, DSF = drilling depth below seafloor, CSF = core depth below seafloor. ROP = rate of penetration. APC = advanced piston corer, HLAPC = half-length APC, RCB = rotary core barrel. Core type: X = XCB, numeric core type = drilled interval. (Continued on next page.) **Download table in CSV format.**

Hole U1385K	Hole U1385L
Latitude: 37°34.0099′N	Latitude: 37°34.0197′N
Longitude: 10°7.6370′W	Longitude: 10°7.6367′W
Water depth (m): 2584.17	Water depth (m): 2584.17
Date started (UTC): 1645 h; 12 January 2024	Date started (UTC): 1330 h; 15 January 2024
Date finished (UTC): 1330 h; 15 January 2024	Date finished (UTC): 0030 h; 18 January 2024
Time on hole (days): 2.86	Time on hole (days): 2.75
Seafloor depth DRF (m): 2595.4	Seafloor depth DRF (m): 2595.4
Seafloor depth est. method: Tagged	Seafloor depth est. method: Offset
Rig floor to sea level (m): 11.23	Rig floor to sea level (m): 11.23
Penetration DSF (m): 552.5	Penetration DSF (m): 443.9
Cored interval (m): 167.5	Cored interval (m): 67.9
Recovered length (m): 127.89	Recovered length (m): 58.44
Recovery (%): 76.35	Recovery (%): 86.07
Drilled interval (m): 385	Drilled interval (m): 376
Drilled interval (*N*): 1	Drilled interval (*N*): 1
Total cores (*N*): 20	Total cores (*N*): 7
APC cores (*N*): 0	APC cores (*N*): 0
HLAPC cores (*N*): 0	HLAPC cores (*N*): 0
XCB cores (*N*): 20	XCB cores (*N*): 7
RCB cores (*N*): 0	RCB cores (*N*): 0
Other cores (*N*): 0	Other cores (*N*): 0

Table T1 (continued).

Core	Top depth drilled DSF (m)	Bottom depth drilled DSF (m)	Interval advanced (m)	Top depth cored CSF (m)	Bottom depth recovered (m)	Recovered length (m)	Curated length (m)	Recovery (%)	Sections (*N*)	Real ROP (m/h)	Core on deck date (2024)	Core on deck time UTC (h)
401-U1385K-												
Start hole											13 Jan	0035
11	0.0	385.0			*****Drilled from 0.0 to 385.0 mbsf*****					57.8	13 Jan	1655
2X	385.0	389.7	4.7	385.0	385.92	0.92	0.92	20	2	4.3	13 Jan	1850
3X	389.7	397.7	8.0	389.7	389.70	0.00		0	0	9.6	13 Jan	2050
4X	397.7	402.4	4.7	397.7	397.70	0.00		0	0	14.1	13 Jan	2225
5X	402.4	407.2	4.8	402.4	402.40	0.00		0	0	14.4	14 Jan	0010
6X	407.2	411.9	4.7	407.2	407.22	0.02	0.02	0	1	18.8	14 Jan	0145
7X	411.9	416.7	4.8	411.9	415.55	3.65	3.65	76	4	19.2	14 Jan	0435
8X	416.7	426.4	9.7	416.7	425.96	9.26	9.26	95	7	14.6	14 Jan	0630
9X	426.4	436.1	9.7	426.4	430.01	3.61	3.61	37	4	5.3	14 Jan	0850
10X	436.1	445.8	9.7	436.1	444.45	8.35	8.35	86	7	8.3	14 Jan	1140
11X	445.8	455.5	9.7	445.8	455.61	9.81	9.81	101	8	23.3	14 Jan	1325
12X	455.5	465.2	9.7	455.5	463.03	7.53	7.53	78	6	9.7	14 Jan	1545
13X	465.2	474.9	9.7	465.2	474.10	8.90	8.90	92	7	10.6	14 Jan	1800
14X	474.9	484.6	9.7	474.9	484.64	9.74	9.74	100	8	12.9	14 Jan	2005
15X	484.6	494.3	9.7	484.6	494.46	9.86	9.86	102	8	14.6	14 Jan	2200
16X	494.3	504.0	9.7	494.3	504.20	9.90	9.90	102	8	10.6	15 Jan	0030
17X	504.0	513.7	9.7	504.0	513.37	9.37	9.37	97	8	14.6	15 Jan	0240
18X	513.7	523.4	9.7	513.7	521.41	7.71	7.71	79	6	16.6	15 Jan	0435
19X	523.4	533.1	9.7	523.4	532.91	9.51	9.51	98	8	16.6	15 Jan	0645
20X	533.1	542.8	9.7	533.1	543.00	9.90	9.90	102	8	19.4	15 Jan	0835
21X	542.8	552.5	9.7	542.8	552.65	9.85	9.85	102	8	16.6	15 Jan	1035
		Hole U1385K total:	167.50			127.90	127.90	76				
401-U1385L-												
Start hole											15 Jan	1155
11	0.0	376.0			*****Drilled from 0.0 to 376.0 mbsf*****					68.4	16 Jan	0325
2X	376.0	385.7	9.7	376.0	381.61	5.61	5.61	58	5	11.6	16 Jan	0505
3X	385.7	395.4	9.7	385.7	393.74	8.04	8.04	83	7	14.6	16 Jan	0640
4X	395.4	405.1	9.7	395.4	404.04	8.64	8.64	89	7	9.7	16 Jan	0830
5X	405.1	414.8	9.7	405.1	414.23	9.13	9.13	94	7	23.3	16 Jan	1035
6X	414.8	424.5	9.7	414.8	424.66	9.86	9.86	102	8	23.3	16 Jan	1215
7X	424.5	434.2	9.7	424.5	433.40	8.90	8.90	92	7	16.6	16 Jan	1405
8X	434.2	443.9	9.7	434.2	442.46	8.26	8.26	85	7	10.6	16 Jan	1630
		Hole U1385L total:	67.90			58.40	58.04	86				

The ship began waiting on weather at 2315 h on 16 January. At midmorning on 17 January, the average wind speed reached 35 kt, gusting to 65 kt, and then it eased throughout the day. After waiting on weather for 28.25 h, we were able to resume operations at 0330 h on 18 January. The BHA was raised, disassembled, and stowed. The thrusters were raised at 0720 h, and at 0736 h we started the transit to Site U1611, ending operations at Site U1385.

3. Lithostratigraphy

Two lithologies were described for Site U1385: calcareous clay and clayey calcareous ooze (Figures **F5**, **F6**, **F7**; see HANDDRAWN in **Supplementary material**). Smear slide analysis, additional geochemistry data (e.g., coulometry and X-ray diffraction [XRD]), and physical properties data were integrated with visual core description to aid in lithologic identification and the definition of three lithostratigraphic units and their boundaries (Figures **F6**, **F7**). Unit I (385.0–458.5 m core depth below seafloor, Method A [CSF-A] in Hole U1385K and 376.0–442.5 m CSF-A in Hole U1385L) is composed of calcareous clay and clayey calcareous ooze. Subunit Ia (385.0–430.0 m CSF-A in Hole U1385K and 376.0–430.5 m CSF-A in Hole U1385L) is relatively homogeneous with gradational alternations between calcareous clay and clayey calcareous ooze (Figure **F8**). Subunit Ib (430.0–458.5 m CSF-A in Hole U1385K and 430.5–442.5 m CSF-A in Hole U1385L) is characterized by sharp contacts between calcareous clay and clayey calcareous ooze. Unit II (458.5–519.6 m CSF-A in Hole U1385K only) includes frequent cyclic alternations between calcareous clay (dark gray and olive-gray) and clayey calcareous ooze. Unit III (519.6–552.65 m CSF-A in Hole U1385K only) predominantly consists of calcareous clay (dark gray and olive-gray) with thinner beds of clayey calcareous ooze.

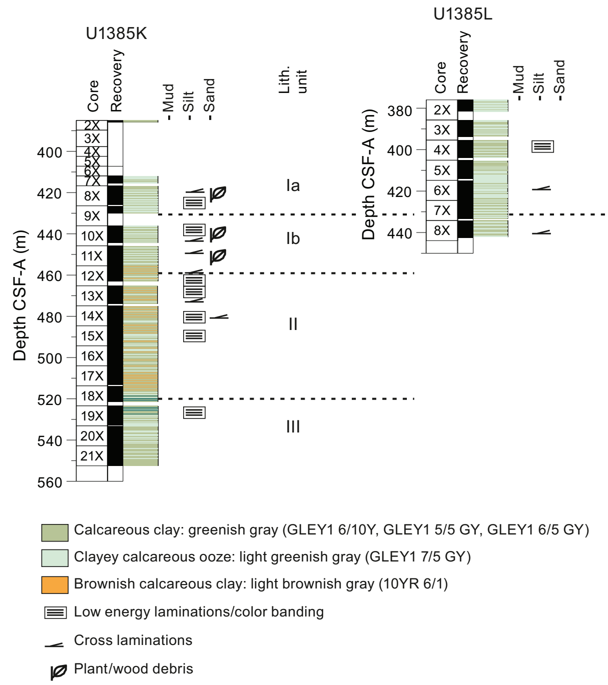

Figure F5. Lithologic synthesis, Holes U1385K and U1385L. See SYNTHLOGS in Supplementary material for editable version of this figure.

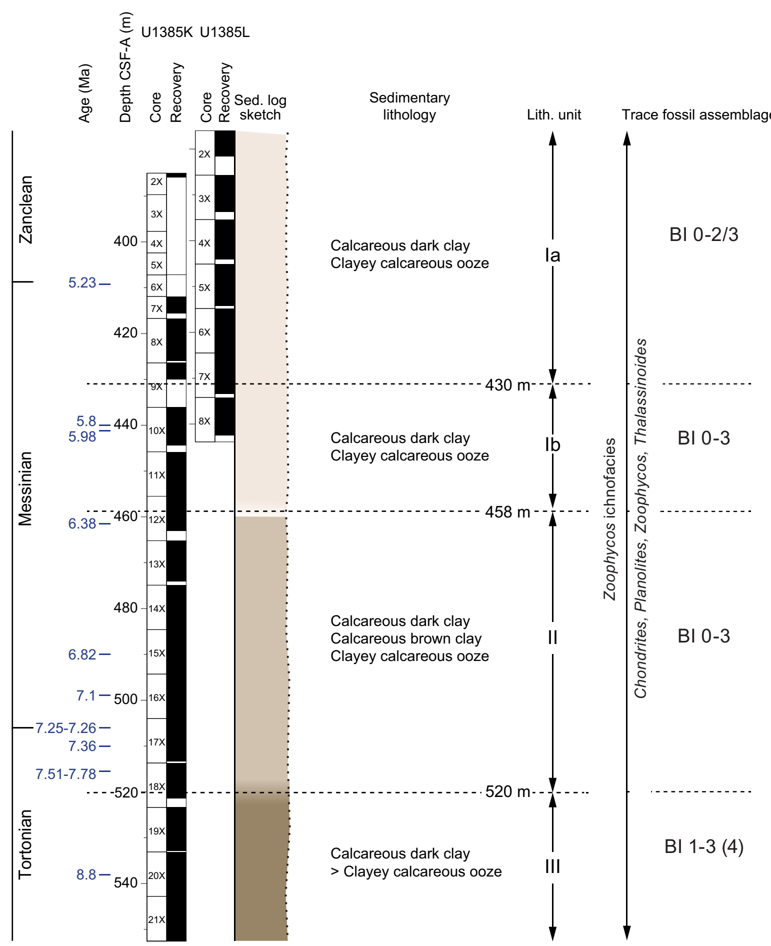

Figure F6. Lithologic summary, Holes U1385K and U1385L. Curve in sedimentary log indicates long-term relative variations of coarser versus finer grained sediments.

In general, the clayey calcareous ooze is lighter gray or greenish gray, whereas the calcareous clay is a darker shade of gray, olive-gray, or greenish gray. Minor lithologies include clay- and pyrite-rich intervals that exhibit shades of orange-brown and blue-green. In Units II and III, the calcareous clay is a darker shade of greenish gray and/or olive-gray.

Individual bed thickness for each primary lithology was calculated for both holes (Figure **F7**). The top and bottom of each core were excluded because they represent only a portion of the bed and would result in an underestimation of bed thickness. For cores composed entirely of a single lithology, the calculated thickness represents the minimum bed thickness. In many cases, the boundaries between lithologies are gradational and the lithologic contacts are placed within the transitional interval. In these instances, the calculated bed thickness may not strictly correspond to the true bed thickness. The lithologic boundaries can be more accurately determined by integrating visual core description information with physical properties data (e.g., magnetic susceptibility [MS] and natural gamma radiation [NGR]) and reflectance spectroscopy and colorimetry (e.g., red-green-blue [RGB] color; Figure **F9**).

The trace fossil assemblage at Site U1385 is largely similar throughout; however, intervals with abundant trace fossils (bioturbation index [BI] = 3–4) alternate with intervals associated with laminations where bioturbation is absent (BI = 0). Seven ichnotaxa were recognized at the ichnogenus level, including abundant *Chondrites, Planolites*, and *Zoophycos*; frequent *Thalassinoides*; rare *Palaeophycus*; and occasional *Asterosoma* and *Spirophyton* (Figure **F10**). Undifferentiated horizontal and vertical structures were also observed. Traces with darker and lighter infill can be related to calcareous clay and clayey calcareous ooze, respectively. Crosscutting relationships are frequent among the ichnotaxa.

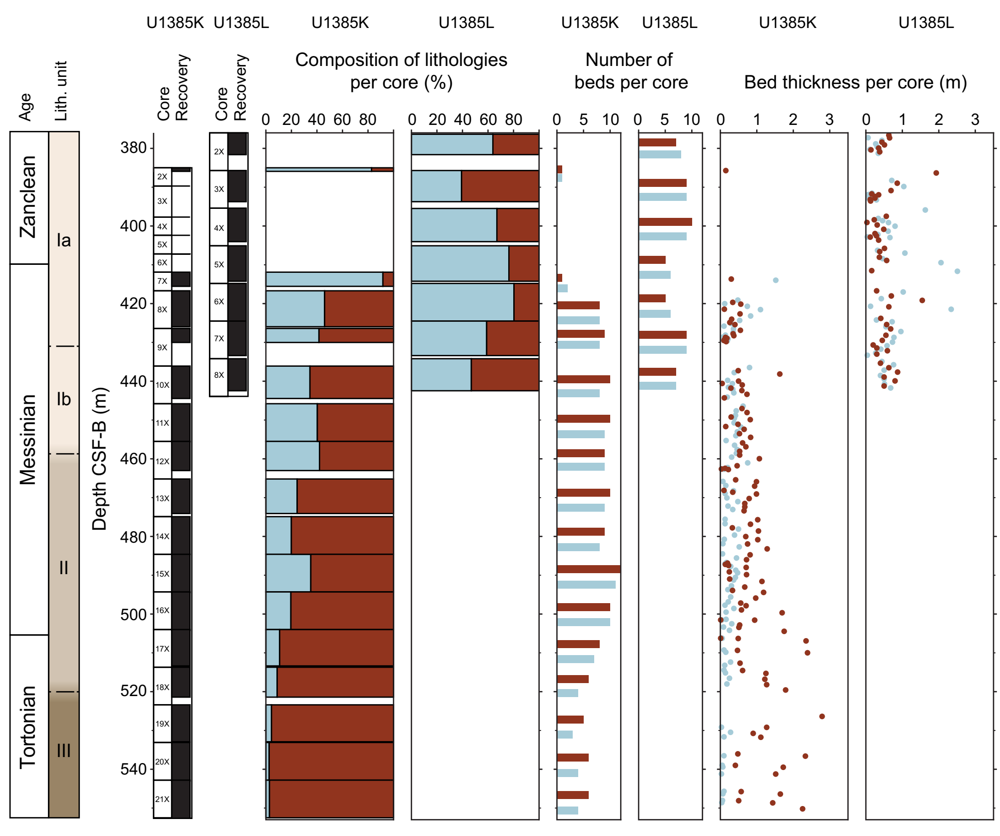

Figure F7. Core and bed thickness by lithology, Holes U1385K and U1385L. Visual bed thickness for calcareous clay in lower part of sequence is not inline with cycle thickness from physical properties data (see Stratigraphic correlation and age model).

Smear slides were taken regularly from Hole U1385K (n = 45) for petrographic analysis (Table **T2**). Smear slides prepared from Hole U1385L (n = 8) were analyzed to determine the lithology in poorly recovered intervals in Hole U1385K and confirm the presence of the same lithologies identified in Hole U1385K. Based on shipboard analyses for Holes U1385K and U1385L, the total carbonate content in these cores ranges 39%–69% (see **Geochemistry**). XRD analysis was conducted on 5 squeeze cake residues and 14 spot samples collected from the working halves of Holes U1385K and U1385L to gain a general understanding of the bulk mineralogy of different lithologies and identify any large-scale trends with depth. Representative diffraction patterns of the bulk mineralogy of the two primary lithologies in the three units are shown in Figure **F11**. Primary minerals identified are quartz; calcite; plagioclase; K-feldspar; and clay minerals including chlorite,

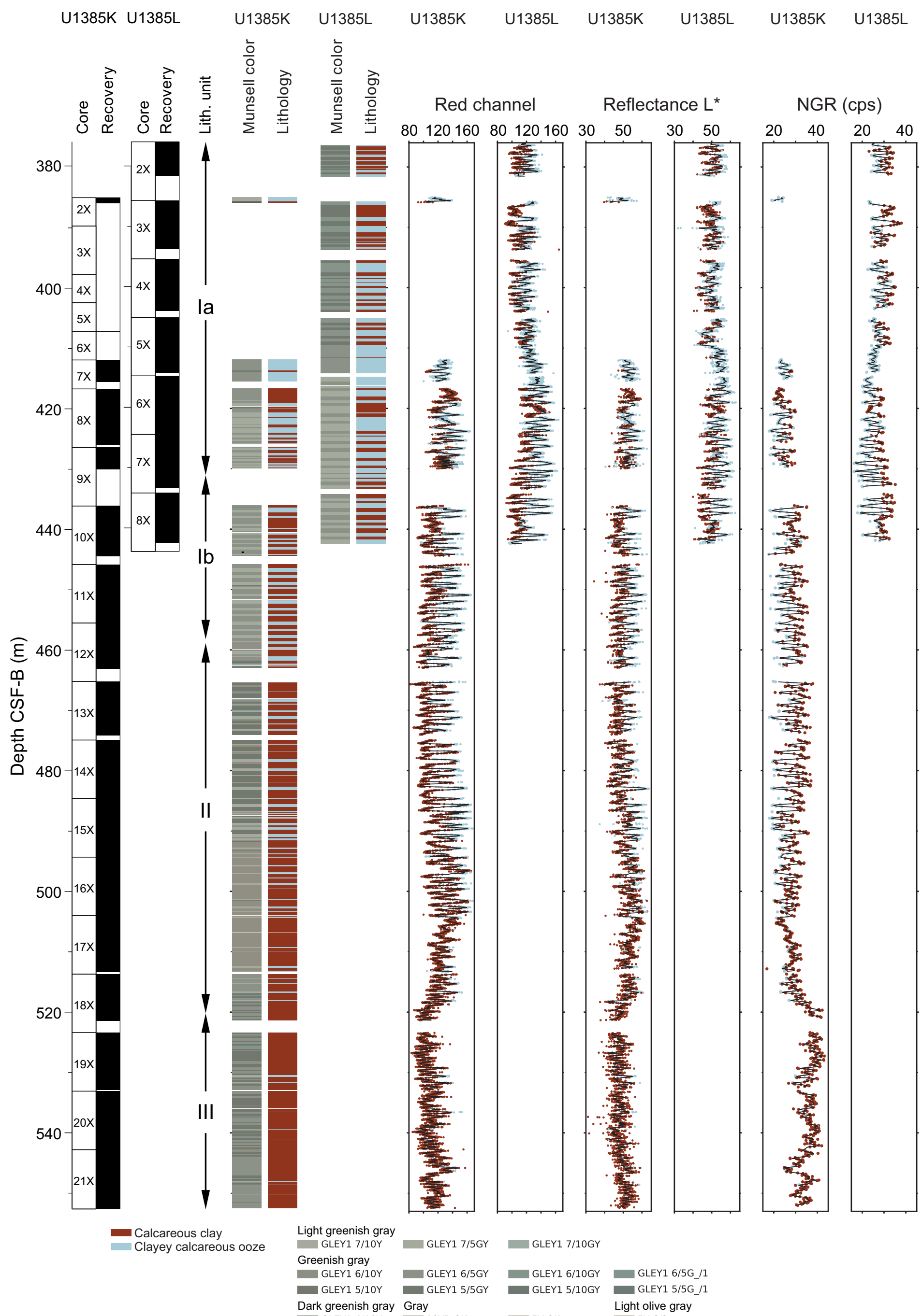

Figure F8. Cyclicity, Holes U1385K and U1385L. Red channel is from Section Half Imaging Logger. Reflectance L* is from Section Half Multisensor Logger. cps = counts per second.

illite (or mica), kaolinite, and mixed-layer illite/smectite (I/S) and minor dolomite and pyrite. Distinct peaks suggesting the presence of siderite were found in two samples (401-U1385K-8X-6, 94–95 cm [425.08 m CSF-A], and 12X-3, 127–128 cm [459.75 m CSF-A]). The bulk mineral assemblage is uniform downhole from Unit I to Unit III, with the most distinct changes in the relative peak intensities between calcite and other siliciclastic minerals (Figure **F11**). Overall, total carbonate content and its variation with depth as determined from XRD are consistent with total carbonate content determined by coulometry (Figure **F40**) based on samples analyzed from the same stratigraphic interval (Figure **F12**). Because of the relatively large sampling interval for interstitial water (IW) squeeze cakes and the lithology-driven sampling strategy for XRD analysis, the variations in total carbonate content (Figure **F12**) do not fully reflect the shorter term and subtler lithologic variations that dominate the NGR data (see **Physical properties**; Figure **F41**). The relative abundance of different minerals and mineral groups in all the XRD samples with depth in Holes U1385K and U1385L together with organic carbon content (from **Geochemistry**) is shown in Figure **F13**.

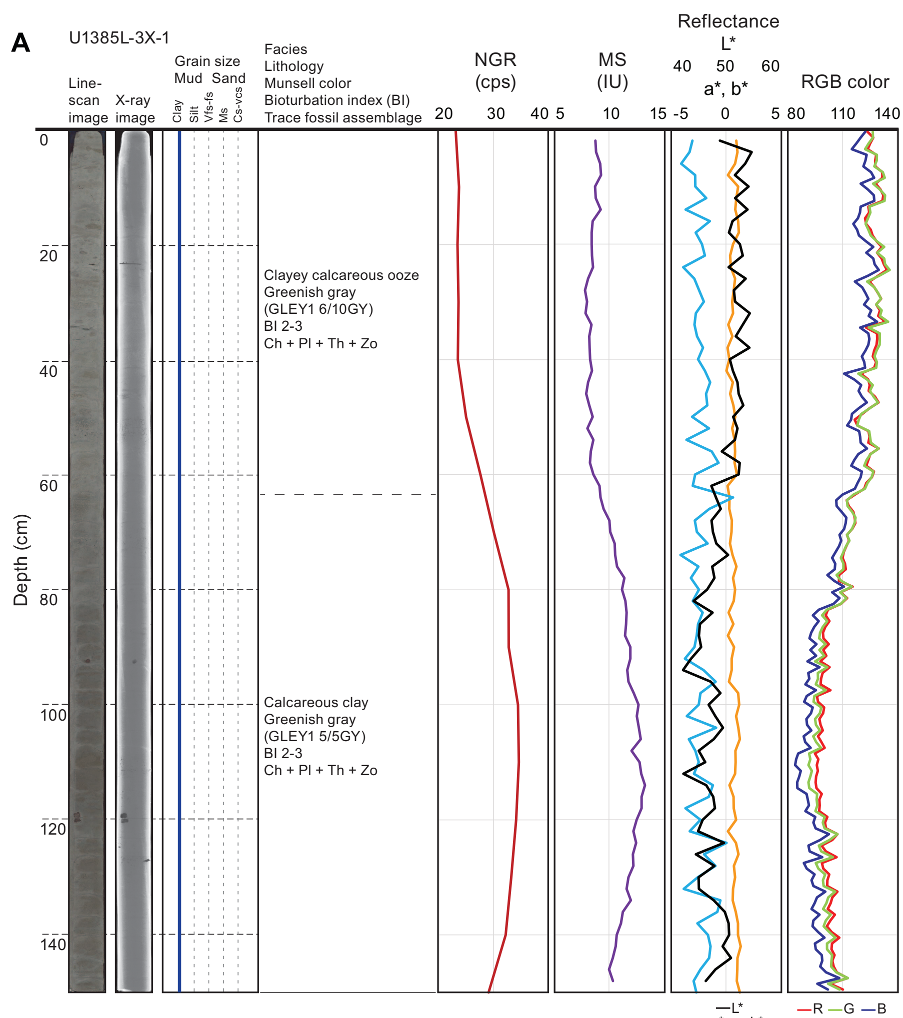

Figure F9. Example facies description for each unit, Holes U1385K and U1385L. Linescan image and RGB color are from Section Half Imaging Logger. X-ray image is from X-Ray Linescan Logger (XSCAN). Reflectance (L*a*b*) and MS are from Section Half Multisensor Logger. Vfs = very fine sand, fs = fine sand, Ms = medium sand, Cs = coarse sand, vcs = very coarse sand. Ch = *Chondrites*, Pl = *Planolites*, Th = *Thalassinoides*, Zo = *Zoophycos*. cps = counts per second, IU = instrument units. A. Greenish gray clayey calcareous ooze and greenish gray (slightly darker) calcareous clay, Subunit Ia. (Continued on next three pages.)

3.1. Unit I description

Intervals: 401-U1385K-2X-1 through 12X-2; 401-U1385L-2X-1 through 8X-CC
Depths: Hole U1385K = 385.0–458.5 m CSF-A; Hole U1385L = 376.0–442.5 m CSF-A
Age: Early Pliocene to late Messinian

3.1.1. Subunit Ia

Intervals: 401-U1385K-2X-1 through 9X-CC; 401-U1385L-2X-1 through 7X-4
Depths: Hole U1385K = 385.0–430.0 m CSF-A; Hole U1385L = 376.0–430.5 m CSF-A

3.1.1.1. Lithologies, bedding, and color

The dominant lithologies in Subunit Ia are calcareous clay and clayey calcareous ooze. These lithologies generally vary in color (Figure **F8**), with calcareous clay having a darker shade of greenish gray (GLEY1 5/5GY and GLEY1 6/5GY) and clayey calcareous ooze having light greenish gray (GLEY1 7/5GY) and greenish gray (GLEY1 6/10GY) colors. Lithologies are commonly distinguishable by color, and gradual color changes throughout Subunit Ia reflect lithologic transitions (Figure **F9A**). The upward transition from calcareous clay to clayey calcareous ooze is commonly gradational, but the upward transition from clayey calcareous ooze to calcareous clay tends to occur more abruptly.

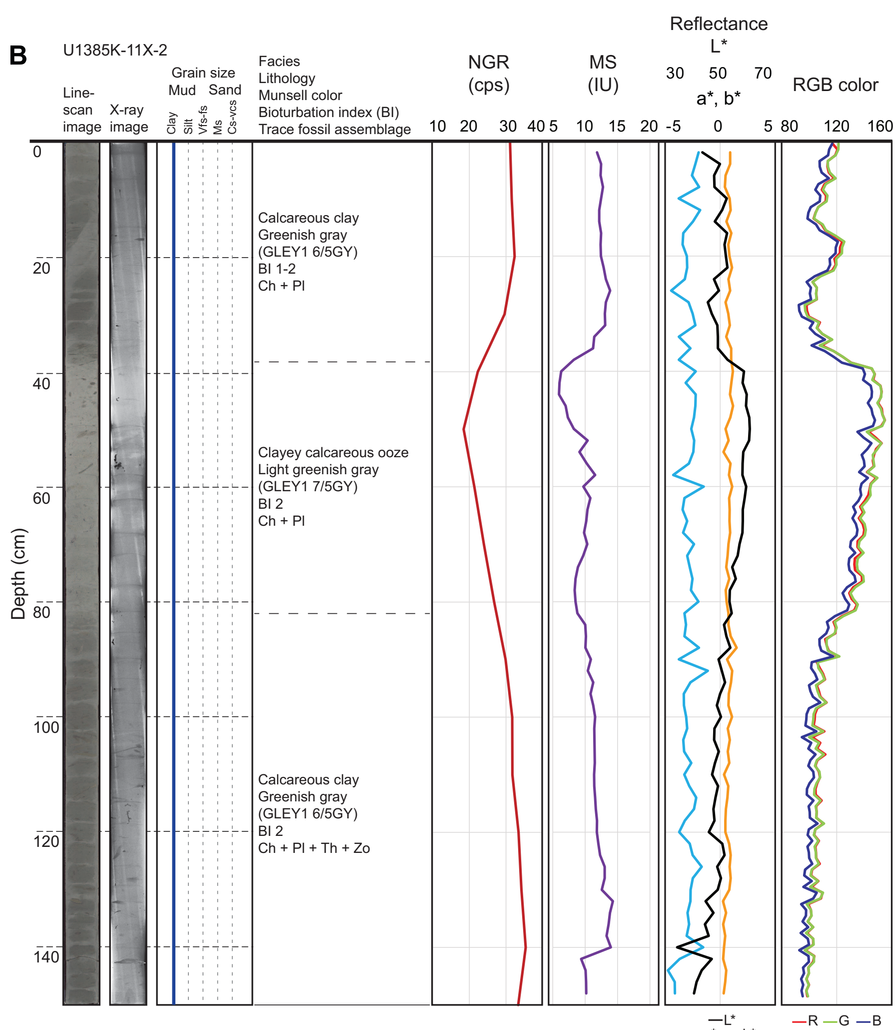

Figure F9 (continued). B. Greenish gray (darker) calcareous clay and light greenish gray clayey calcareous ooze, Subunit Ib. (Continued on next page.)

Because of the subtle and gradational changes observed between lithologies, occasionally physical properties data were used to define lithologic boundaries. For example, calcareous clays have higher NGR and MS values and relatively lower L* reflectance and RGB color values than clayey calcareous ooze (Figures **F8**, **F9A**).

This subunit is distinct because of the homogeneous appearance of each of the two lithologies and very gradational changes throughout. The bed thickness in Subunit Ia averages 29 cm (Hole U1385K) to 46 cm (Hole U1385L) for calcareous clay and 42 cm (Hole U1385K) to 62 cm (Hole U1385L) for clayey calcareous ooze. The thickest beds located in the upper part of Subunit Ia were not recovered in Hole U1385K, which may explain the difference in bed thickness between Holes U1385K and U1385L (Figure **F7**).

3.1.1.2. Structure and texture

Primary structures that are usually too subtle to be easily distinguished in these fine-grained sediments on the sample table can be recognized by careful analysis of the core photographs from the Section Half Imaging Logger (SHIL). Laminae characterized by subtle color variations are present in the calcareous clays in the lower part of Subunit Ia below ~415 m CSF-A (Figures **F5**, **F14C, F14E**). Specifically, Core 401-U1385L-6X has parallel and cross lamination, distinguishable by distinct color differences, and Core 401-U1385K-9X has parallel lamination. Overall, Subunit Ia calcareous clay shows color changes throughout and commonly exhibits intercalations between

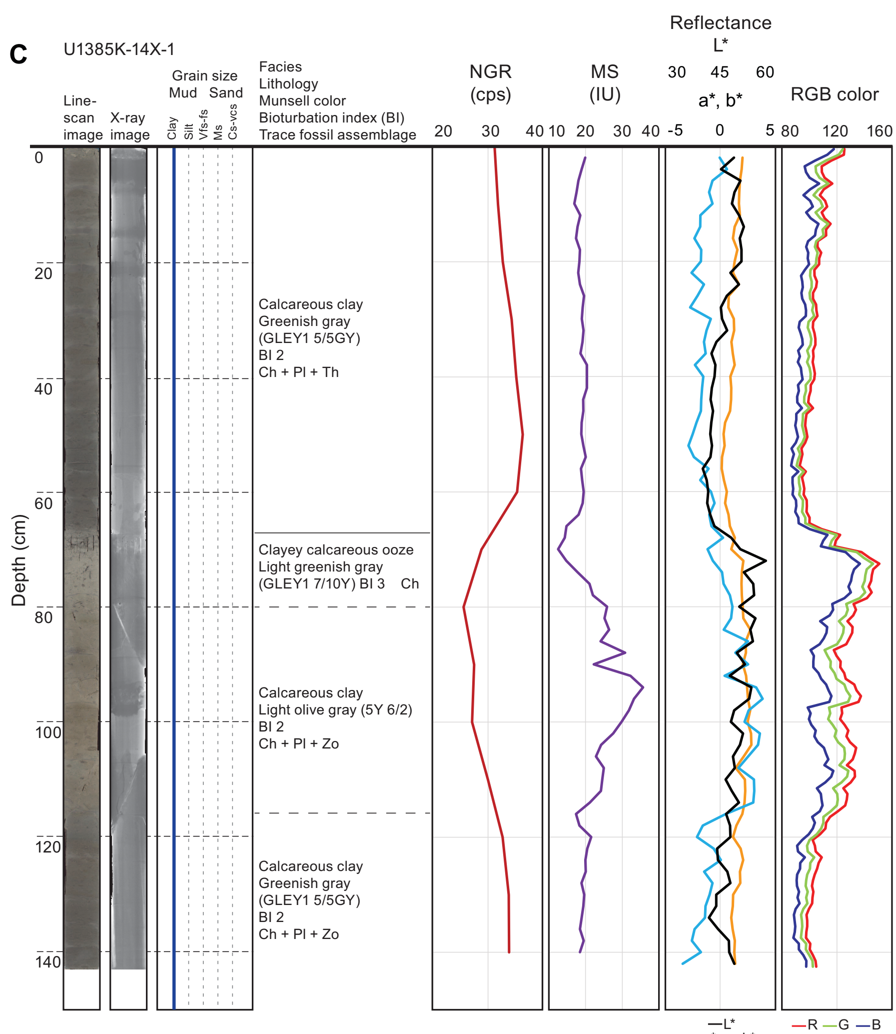

Figure F9 (continued). C. Greenish gray (darker) calcareous clay, light greenish gray clayey calcareous ooze, and light olive-gray calcareous mud, Unit II. (Continued on next page.)

several shades of greenish gray (GLEY1 5/10Y and GLEY1 5/5G_/1), the latter with a slightly greener tint. No distinct sedimentary structures were observed in the clayey calcareous ooze.

Smear slides show that the dominant texture in both calcareous clay and clayey calcareous ooze in Subunit Ia is clay (Figures **F15**, **F16**). The sand fraction is very minor (0%–5%), and the maximum grain size differs between lithologies. The clayey calcareous ooze tends to have fine sand-sized foraminifers, whereas these are generally less abundant and finer grained in the calcareous clay (maximum grain size is very fine sand). Bioturbation and trace fossils

Discrete trace fossils in Subunit Ia are sparse to moderate in abundance (mainly BI = 1 to 2 or 3) and occasionally absent (BI = 0) in the laminated intervals (Figure **F17**). The trace fossil assemblage consists of abundant *Chondrites, Planolites*, and *Zoophycos*; frequent *Thalassinoides*; and rare *Palaeophycus*. Gradual and subtle color changes throughout Subunit Ia complicate the distinction of lithologic boundaries and the differentiation between darker infilled and lighter infilled traces in the transition between calcareous clay and clayey calcareous ooze (Figure **F17**). Even so, occasionally dark *Zoophycos* penetrate around 20 cm from calcareous clay into the underlying clayey calcareous ooze (Figure **F18**).

3.1.1.3. Composition and bulk mineralogy

Smear slides show that Subunit Ia calcareous clay contains mainly siliciclastic grains, whereas the clayey calcareous ooze contains a smaller quantity of siliciclastic grains and a higher abundance of biogenic carbonates (Figure **F19**). Subunit Ia calcareous clay consists of 45%–70% siliciclastic grains, 0%–10% detrital and/or authigenic carbonate, and 25%–45% biogenic carbonate. Subunit Ia clayey calcareous ooze consists of 30%–65% siliciclastic grains, 0%–10% detrital and/or authigenic carbonate, and 30%–60% biogenic carbonate. The content of foraminifers varies throughout this subunit, ranging 2%–10%, and tends to be higher in the clayey calcareous ooze (Figure **F19**). Glauconite and fish bones are present in minor quantities. Pyrite is typically rare, except in areas in or close to pyrite nodules and in intervals with a slightly greener tint (GLEY1 5/5G_/1).

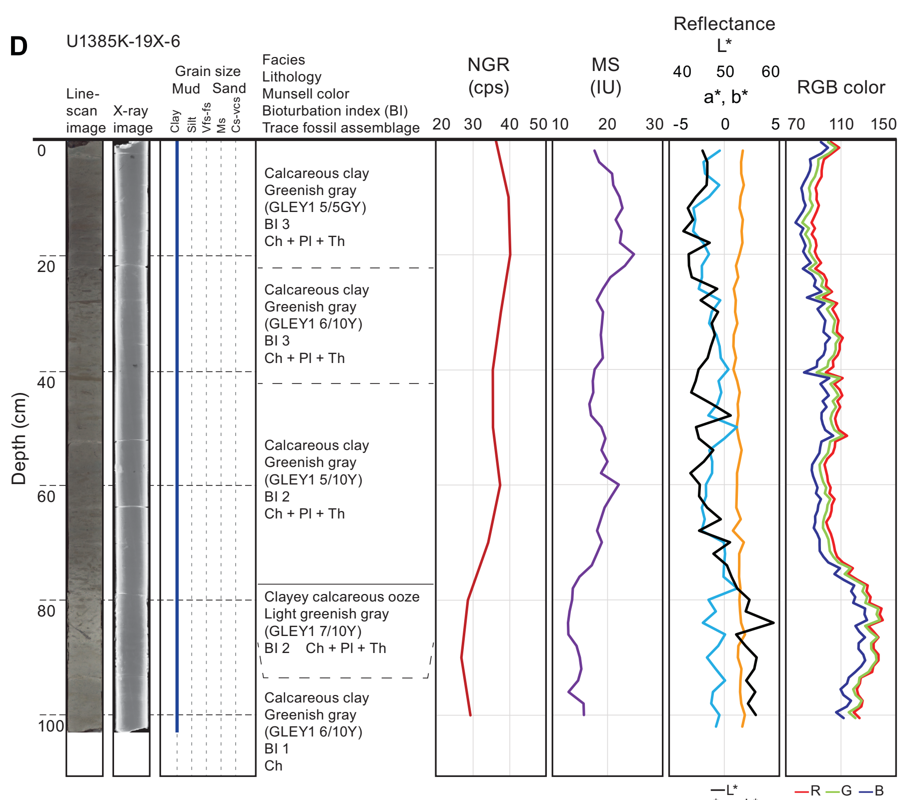

Figure F9 (continued). D. Greenish gray (darker) calcareous clay, greenish gray (intermediate shade) calcareous clay, and light greenish gray clayey calcareous ooze, Unit III.

The bulk mineral composition of five samples of clayey calcareous ooze and one sample of calcareous clay from Subunit Ia were analyzed by XRD. In clayey calcareous ooze, carbonate content ranges 53%–59% (averages = 57%) (Figures **F12**, **F13**). Quartz content is ~8%, feldspar (including plagioclase and K-feldspar) content is ~8%, and clay minerals make up 27% on average (Figure **F13**). The calcareous clay sample has lower carbonate content (42%) and higher quantities of quartz (11%), feldspars (10%), and clay minerals (35%). Both clayey calcareous ooze and calcareous clay have relatively low organic carbon content (average = 0.3%).

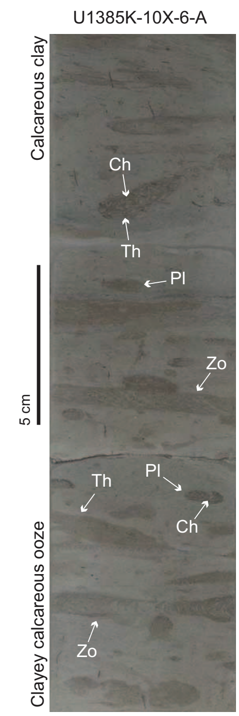

Figure F10. Typical trace fossil assemblage, Site U1385. Ch = *Chondrites*, Pl = *Planolites*, Zo = *Zoophycos*, Th = *Thalassinoides*. Note presence of trace fossils throughout interval and frequent crosscutting relationships among ichnotaxa.

Table T2. Smear slide data, Holes U1385K and U1385L. **Download table in CSV format.**

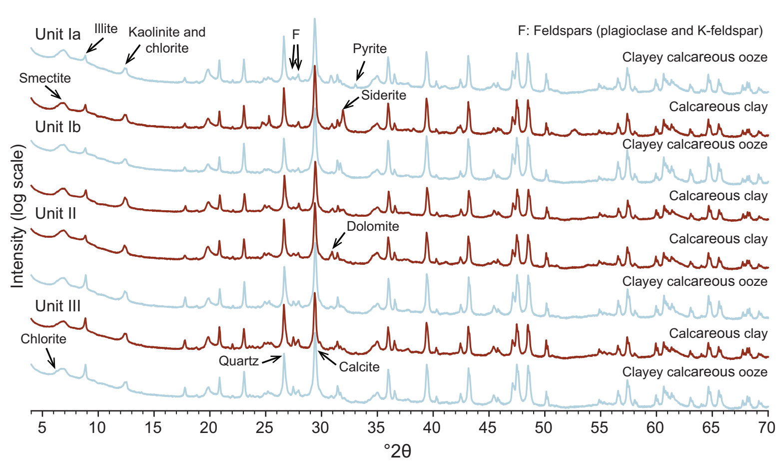

Figure F11. Powder XRD patterns of different lithologies in Units I–III, Site U1385. Samples are arranged from shallow (top) to deep (bottom). Patterns are plotted with intensity on logarithmic scale to highlight presence and nature of smaller peaks. Bulk mineral assemblage is nearly constant downhole.

3.1.2. Subunit Ib

Intervals: 401-U1385K-10X-1 through 12X-2; 401-U1385L-7X-5 through 8X-CC
Depths: Hole U1385K = 430.0–458.5 m CSF-A; Hole U1385L = 430.5–442.5 m CSF-A

3.1.2.1. Lithologies, bedding, and color

Subunit Ib comprises similarly alternating calcareous clay and clayey calcareous ooze with variable thicknesses as in Subunit Ia. Subunit Ib is distinguished from Subunit Ia because the lithologies in Subunit Ib commonly have sharp boundaries characterized by distinct color changes. The calcareous clay is greenish gray (GLEY1 5/10Y and GLEY1 6/5GY) and occasionally gray (10YR 6/1), whereas the clayey calcareous ooze is light greenish gray (GLEY1 7/5GY) and occasionally gray (10YR 6/1) (Figures **F8**, **F20**). The upward transition from the calcareous clay to the clayey calcareous ooze is gradational, but the upward transition from clayey calcareous ooze to calcareous clay is commonly sharp (Figure **F9B**).

Lithologic changes in Subunit Ib are reflected by color changes as well as physical properties and color variations. This is particularly well illustrated in Core 401-U1385K-11X (Figure **F20**), where calcareous clays have higher NGR values and lower L* reflectance and RGB color values than the clayey calcareous ooze (Figures **F8**, **F20**). Physical properties data were used to help define the position of lithologic boundaries where lithologic changes are gradational and subtle.

Bed thickness in Subunit Ib averages 57 cm (Hole U1385K) to 54 cm (Hole U1385L) for calcareous clay and 40 cm (Hole U1385K) to 45 cm (Hole U1385L) for clayey calcareous ooze. ,

3.1.2.2. Structure and texture

The clayey calcareous ooze lacks any distinct sedimentary structures. The darker calcareous clay has occasional color banding with a slightly greener tint (GLEY1 5/5G_/1) and subtle parallel and cross lamination (Figure **F14B**).

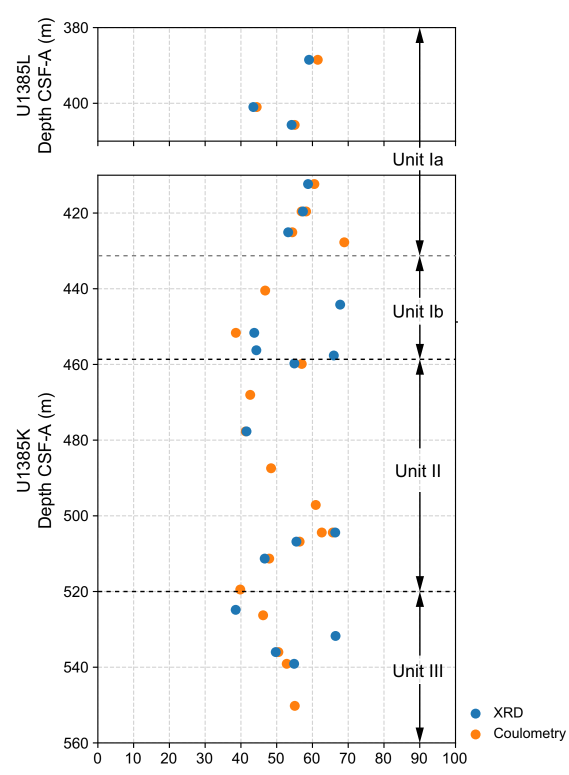

Figure F12. Variation in total carbonate content based on coulometry (see Geochemistry) and XRD data (calcite + dolomite + siderite), Holes U1385K and U1385L. Some XRD and coulometry analyses were made on same squeeze cake sample, and some were made on same stratigraphic interval but not on same sample. Total carbonate content determined on samples by two methods generally shows good agreement.

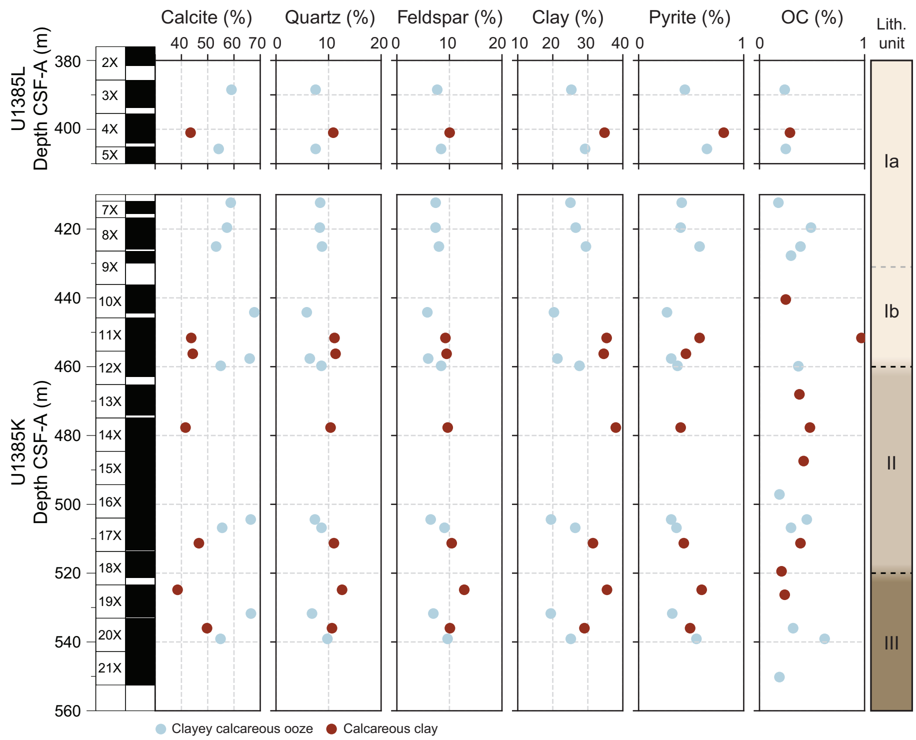

Figure F13. Variations in sediment composition, Holes U1385K and U1385L. Bulk mineralogy was determined from bulk XRD patterns using Rietveld refinements method (see Lithostratigraphy in the Expedition 401 methods chapter [Flecker et al., 2025a]). Feldspar = plagioclase + K-feldspar. Available organic carbon (OC) data are also included (see Geochemistry in the Expedition 401 methods chapter [Flecker et al., 2025a]).

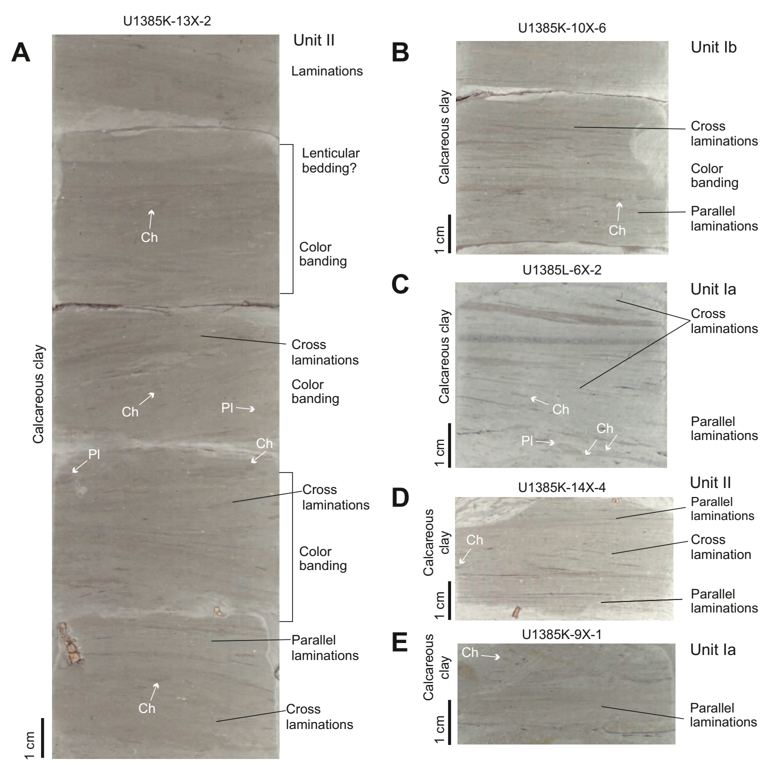

Figure F14. Examples of sedimentary structures (color banding, parallel lamination, cross lamination, and lenticular bedding) associated with calcareous clays, Holes U1385K and U1385L. A, D. Unit II. B. Subunit Ib. C, E. Subunit Ia. Ch = *Chondrites*, Pl = *Planolites*.

Smear slides show that the dominant texture in both calcareous clay and clayey calcareous ooze in Subunit Ib is clay (Figures **F15**, **F16**). Subunit Ib calcareous clay contains 0%–1% sand, 15%–20% silt, and 80%–85% clay, and the clayey calcareous ooze is a little finer grained with 0%–2% sand, 2%–10% silt, and 90%–98% clay. The maximum grain size differs between lithologies; the clayey calcareous ooze tends to contain fine sand-sized foraminifers, whereas foraminifers are typically less abundant and smaller in the calcareous clay where the maximum grain size is very fine sand.

3.1.2.3. Bioturbation and trace fossils

The relative abundance of discrete trace fossils is sparse to moderate (mainly BI = 1–3) and sometimes absent (BI = 0) where lamination is present. The trace fossil assemblage consists of abundant *Chondrites*, *Planolites*, and *Zoophycos*; frequent *Thalassinoides*; and rare *Palaeophycus*. Gradual and subtle color changes throughout Subunit Ib complicate the distinction of lithologic boundaries and the differentiation between darker and lighter infilled traces in the transition between the calcareous clay and the clayey calcareous ooze.

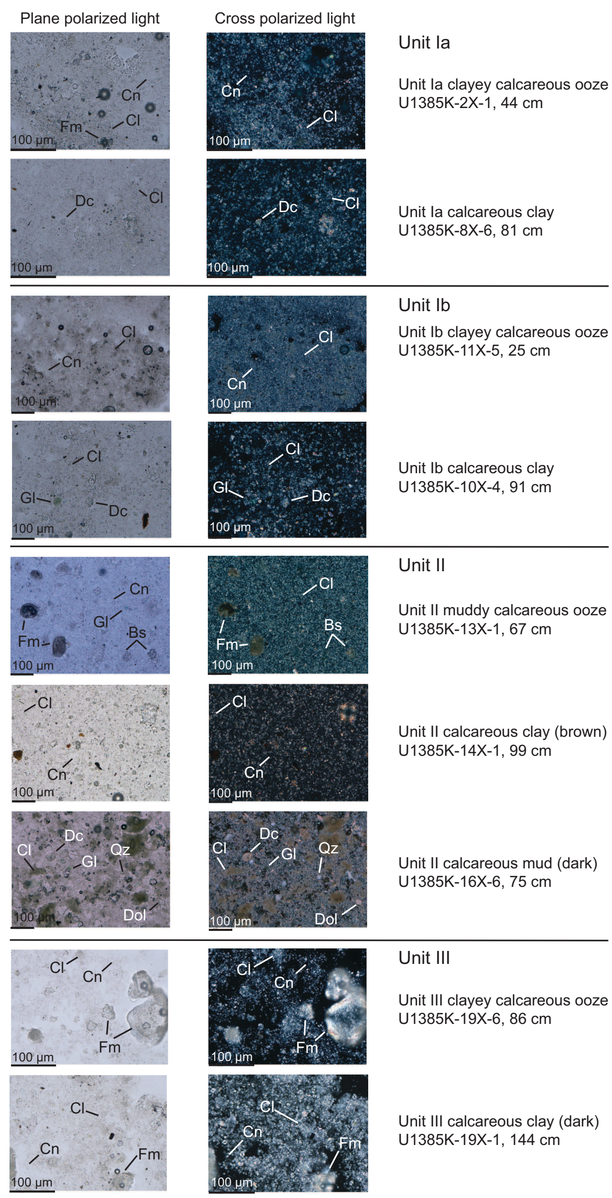

Figure F15. Major lithologies for Units I–III, Hole U1385K. Dominant siliciclastic and biogenic components are annotated. Bs = biosiliceous fragment, Cl = clay, Cn = calcareous nannofossils, Dc = silt-sized detrital carbonate, Dol = dolomite, Fm = foraminifer, Gl = glauconite, Qz = quartz.

3.1.2.4. Composition and bulk mineralogy

Smear slides show that the clayey calcareous ooze in Subunit Ib contains more siliciclastic grains than that in Subunit Ia (Figure **F19**). Some calcareous clay samples in Subunit Ib contain a greater proportion of very fine silt-sized authigenic carbonate than those in Subunit Ia, notably in Section 401-U1385K-11X-3 at 64 cm. Subunit Ib calcareous clay consists of 55%–65% siliciclastic grains, 5%–15% detrital and/or authigenic carbonate, and 30%–35% biogenic carbonate. Subunit Ib clayey calcareous ooze consists of 50%–70% siliciclastic grains, 0%–1% detrital and/or authigenic carbonate, and 30%–50% biogenic carbonate. Comparison with XRD and coulometry data suggests that smear slide analysis may have underestimated the amount of carbonate in the Subunit Ib clayey calcareous ooze, as shown by Figure **F12**. Glauconite, fish bones, and pyrite are commonly present in small quantities.

XRD analysis was conducted on two clayey calcareous ooze samples and two calcareous clay samples from Subunit Ib. The two clayey calcareous ooze samples contain ~67% carbonate, ~6% quartz, ~6% feldspar, and ~20% clay minerals (Figure **F13**). The composition of the two calcareous clay samples from Subunit Ib is similar to those from Subunit Ia.

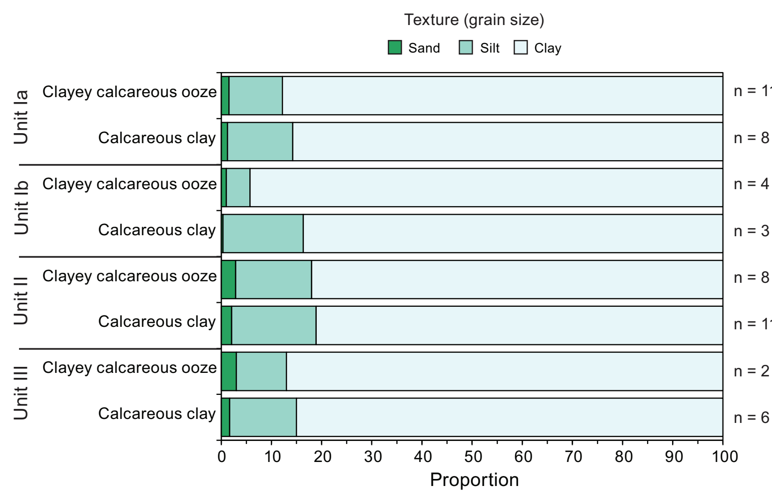

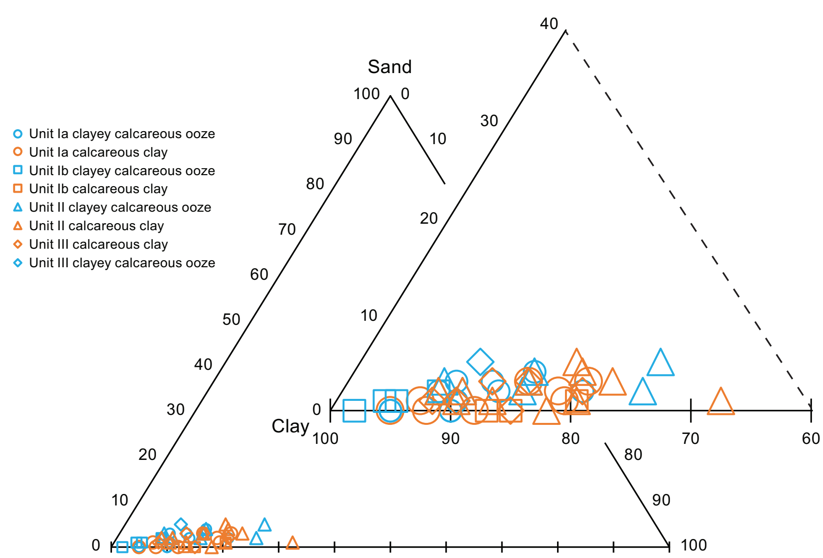

Figure F16. Texture (grain size) of main lithologies in Units I–III, Site U1385. Top: data averaged from smear slide analyses. Bottom: all data (*n* = 53) are plotted; diagram is expanded for visibility.

3.2. Unit II description

Interval: 401-U1385K-12X-3 through 18X-4
Depth: 458.5–519.6 m CSF-A
Age: early Messinian to late Tortonian

3.2.1. Lithologies, bedding, and color

Unit II, present in only Hole U1385K, consists of greenish gray calcareous clay, light olive-gray calcareous clay, and clayey calcareous ooze in varying shades of greenish gray (Figure **F8**). This unit is distinguished from Unit I by the presence of more brownish tones in the light-colored lithologies (Figure **F5**). Unit II is characterized by a distinct change in dominant colors, with an increased predominance of calcareous clay with a deeper tint of greenish gray (GLEY1 6/10Y, GLEY1 6/5GY, and GLEY1 5/5GY) and brownish tones of gray and light olive-gray (10YR 6/1, 5Y 6/1, and 5Y 6/2), whereas the clayey calcareous ooze is light greenish gray (GLEY1 7/10Y and

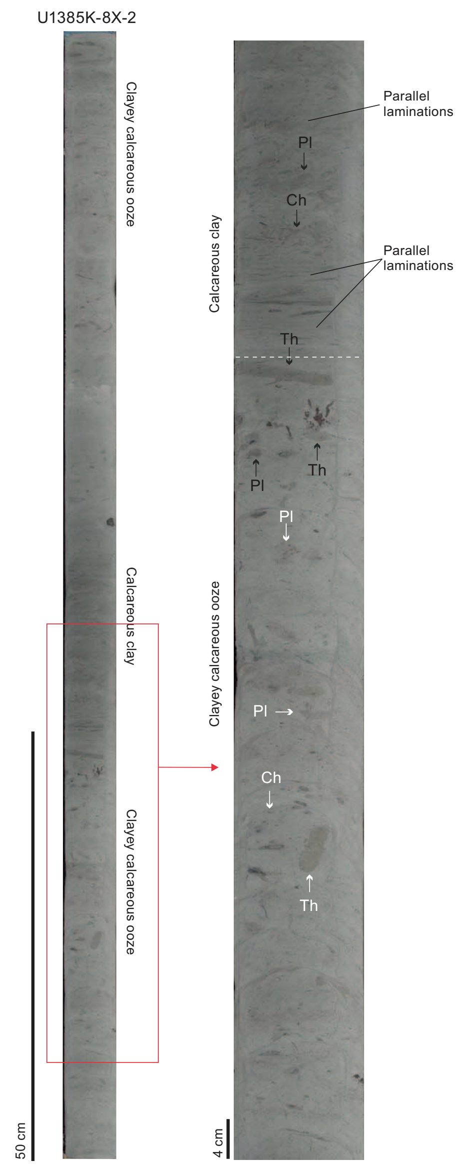

Figure F17. Cycles between clayey calcareous ooze (lighter facies) and calcareous clay (darker facies) in Subunit Ia annotated for trace fossils in contact between facies (dashed white line), Hole U1385K. Note differentiation between dark (black arrows) and light (white arrows) trace fossil assemblages and penetration of dark trace fossils into lighter sediments. Note moderate bioturbation in middle part of clayey calcareous ooze and parallel-lamination in lower part of calcareous clay. Ch = *Chondrites*, Pl = *Planolites*, Th = *Thalassinoides*.

GLEY1 7/5GY). Several distinctive thin greenish beds (GLEY1 5/5G) are intercalated with the calcareous clays. The clayey calcareous ooze typically has a gradational base and a sharper upper contact with the overlying calcareous clay (Figure **F9C**).

Where changes between lithologies were subtle and gradational, physical properties data were used to define lithologic boundaries. The greenish gray calcareous clay has higher NGR and MS and lower reflectance (L*a*b*) and RGB than the clayey calcareous ooze (Figure **F9C**). The gray (5Y 6/1) and light olive-gray (5Y 6/2) calcareous clays typically have intermediate physical properties values between the greenish gray calcareous clay and the clayey calcareous ooze end-members (Figure **F9C**).

Bed thickness in Unit II averages 75 cm for the calcareous clay and 24 cm for the clayey calcareous ooze (Figure **F7**). The thickness of the clayey calcareous ooze beds is relatively constant in Unit II, whereas in the upper part of Unit II (458 to ~490 m CSF-A), the calcareous clay beds are thinner than for the lower part of the unit where beds reach a thickness of 2.4 m. This thickness trend is reflected in the proportion of the different lithologies, and calcareous clay becomes less abundant upward (Figure **F7**).

3.2.2. Structure and texture

Overall, the clayey calcareous ooze and gray and light olive-gray calcareous clay do not have any distinct sedimentary structures. The greenish gray calcareous clay, however, does have subtle parallel lamination, low-angle cross lamination, possible lenticular bedding, and color banding in the upper part of Unit II, as in Cores 401-U1385K-13X and 14X (Figure **F14A, F14D**). These sedimentary structures were not identified in the rest of the unit and are mainly present in the lower portions of the calcareous clay beds directly above the clayey calcareous ooze.

Smear slides show that the dominant texture in both Unit II calcareous clay and the clayey calcareous ooze is clay (Figures **F15**, **F16**). Unit II calcareous clay contains 0%–5% sand, 10%–30% silt, and 70%–90% clay, and the clayey calcareous ooze is very similar, with 2%–5% sand, 10%–25% silt, and 70%–90% clay. The maximum grain size differs between lithologies; the clayey calcareous ooze tends to have fine sand-sized foraminifers, whereas the foraminifers are generally less abundant and finer grained in the calcareous clay (maximum grain size is very fine sand).

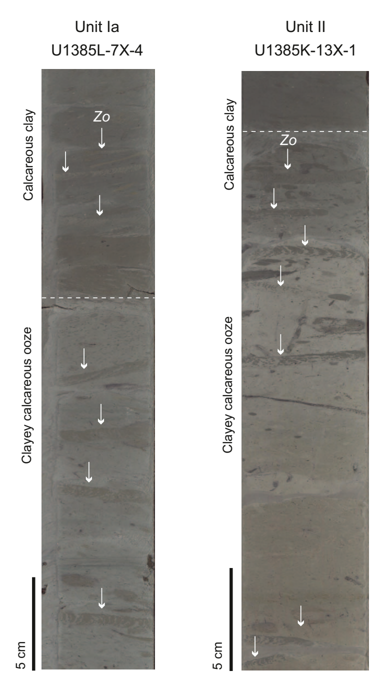

Figure F18. Dark infilled *Zoophycos* (Zo) penetrating from calcareous clay (darker facies) to clayey calcareous ooze (lighter facies), Subunit Ia in Hole U1385L and Unit II in Hole U1385K. Note penetration from contact between facies (dashed white lines) (i.e., darker clay is bioturbated down into lighter calcareous ooze).

3.2.3. Bioturbation and trace fossils

The bioturbation intensity is generally sparse to moderate (mainly BI = 2–3) and only occasionally absent (BI = 0) in the laminated intervals. The trace fossil assemblage consists of abundant *Chondrites, Planolites*, and *Zoophycos*; frequent *Thalassinoides*; and rare *Palaeophycus*. Other ichnotaxa, such as *Asterosoma* and *Spirophyton*, are occasionally visible. Dark *Zoophycos* burrows were observed penetrating ~25 cm into the clayey calcareous ooze from the overlying calcareous clay (Figure **F18**).

3.2.4. Composition and bulk mineralogy

Smear slides show that Unit II calcareous clay contains mainly siliciclastic grains, whereas the clayey calcareous ooze contains a slightly smaller quantity of siliciclastic grains and slightly more carbonates (Figure **F19**). Unit II calcareous clay consists of 35%–75% siliciclastic grains, 1%–10% detrital and/or authigenic carbonate, 15%–50% biogenic carbonate, and 0%–5% biogenic silica. Unit II clayey calcareous ooze consists of 25%–65% siliciclastic grains, 3%–10% detrital and/or authigenic carbonate, 30%–60% biogenic carbonate, and 0%–5% biogenic silica. The content of foraminifers varies from 2% to 8% and tends to be higher in the clayey calcareous ooze. Glauconite, calcareous sponge spicules, diatoms, and fish bones are commonly present in minor amounts.

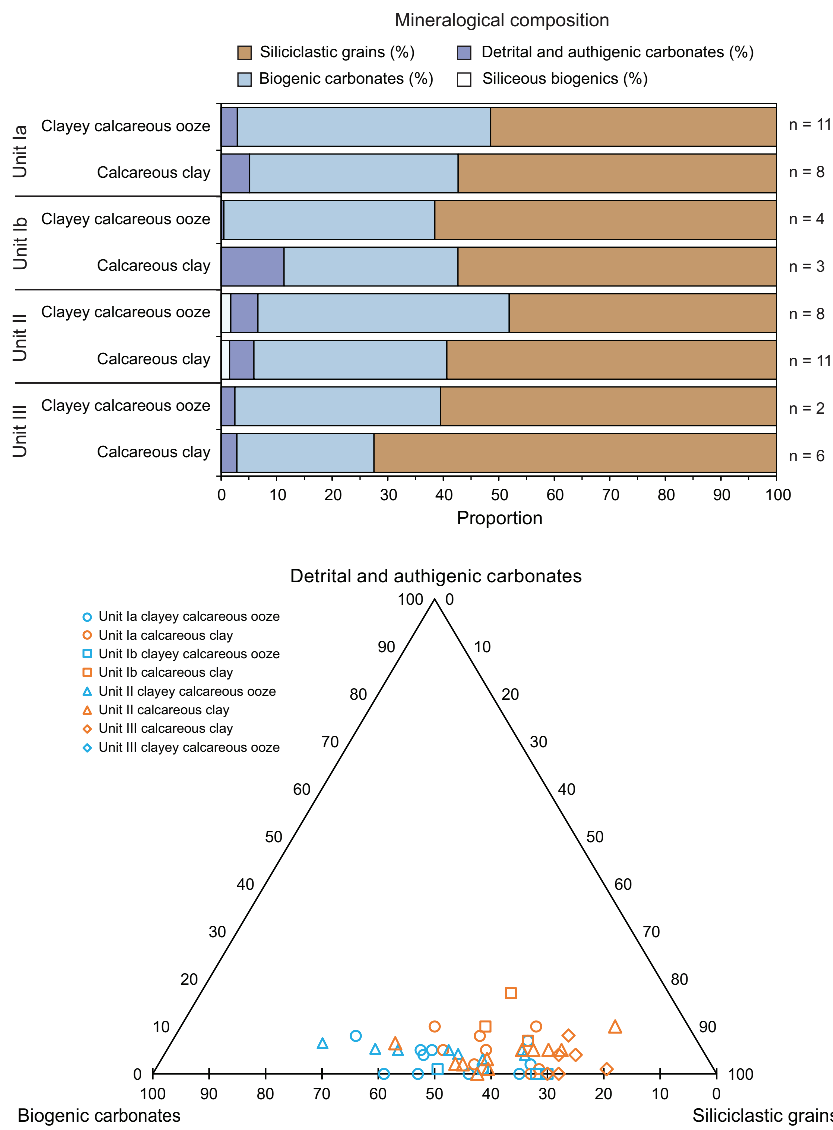

Figure F19. Mineralogical composition of main lithologies in Units I–III, Site U1385. Top: data averaged from smear slide analyses. Bottom: all data (n = 53) are plotted.

Pyrite is usually rare except where it is concentrated in pyrite nodules and exceptionally in Section 401-U1385K-12X-5 at 4 cm, where it makes up 7% of the smear slide.

XRD analysis was conducted on three clayey calcareous ooze and two calcareous clay samples from Unit II. The clayey calcareous ooze and calcareous clay in Unit II have a similar composition to those in Unit I (Figure **F13**) and are characterized by variation in the relative abundance of carbonate and siliciclastic minerals. Based on XRD and the coulometry methods applied to 11 samples from Unit II in Hole U1385K, the carbonate content generally increases from the base of Unit II (520 m CSF-A) upward to ~502 m CSF-A, then decreases upward to ~478 m CSF-A, and then increases again upward to the top of Unit II (458 m CSF-A; Figure **F12**). The general variations in the carbonate content in Unit II can be linked to overall changes in MS, NGR, and reflectance values, especially the L* parameter (Figure **F9C**). A higher carbonate content corresponds to lower MS and NGR values and higher reflectance values (see **Physical properties**). Despite the general correlation between the carbonate content and physical properties on a large scale, the higher frequency changes in physical properties were not captured by variations in total carbonate content because of the limited number of samples analyzed through the XRD and coulometry methods.

3.3. Unit III description

Interval: 401-U1385K-18X-5 through 21X-CC
Depth: 519.6–552.7 m CSF-A
Age: late to middle Tortonian

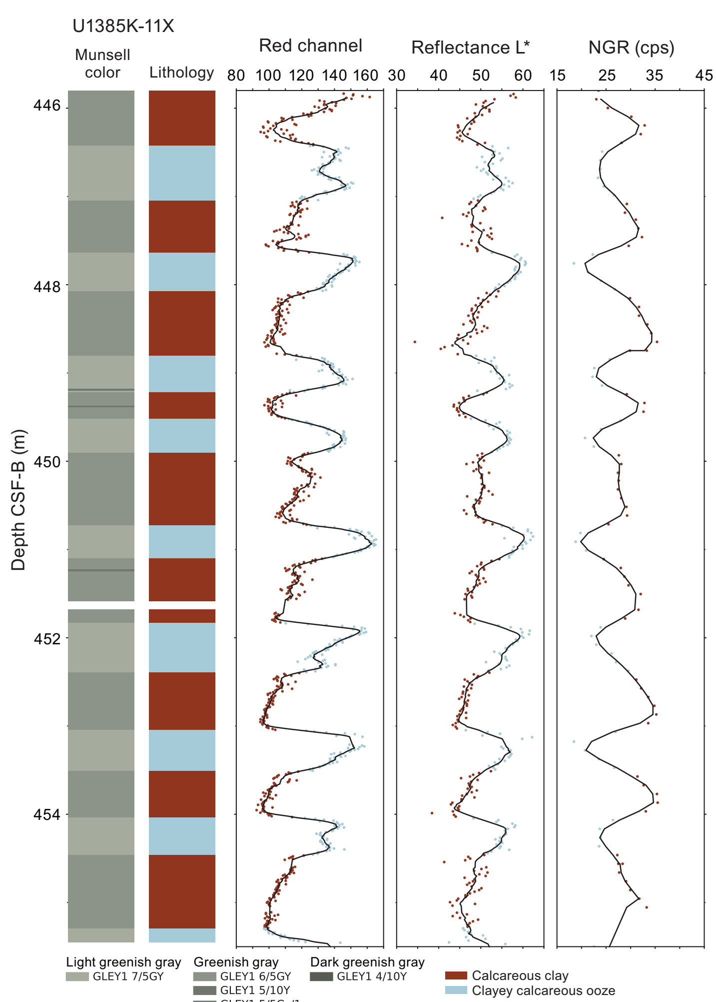

Figure F20. Cyclicity near base of Unit I, Hole U1385K. Red channel is from Section Half Imaging Logger. Reflectance L* is from Section Half Multisensor Logger. cps = counts per second.

3.3.1. Lithologies, bedding, and color

Unit III is mainly composed of calcareous clay alternating with thinner beds of clayey calcareous ooze (Figures **F7**, **F8**). The predominance of calcareous clay results in overall darker hues (greenish gray; GLEY1 5/10Y, GLEY1 6/5GY, GLEY1 6/10Y, and GLEY1 6/5GY) in Unit III compared with the overlying two units. Occasionally, the calcareous clay contains distinctively greenish layers (GLEY1 5/5G). The clayey calcareous ooze is predominantly light greenish gray in color (GLEY1 7/10Y and GLEY1 7/5GY) and typically has a gradational basal contact but a sharper contact at the top (Figure **F9D**).

Where transitions between lithologies are subtle and gradational, physical properties were used to help define lithologic boundaries. For example, calcareous clay has higher NGR and MS values and lower L* reflectance and RGB color values than clayey calcareous ooze (Figure **F9D**).

The bed thickness in Unit III has a large range of thicknesses compared to the overlying units, and the calcareous clay has significantly thicker beds than the clayey calcareous ooze (Figure **F7**). The bed thickness of the calcareous clay ranges 0.4–2.8 m (average = 1.4 m), and the bed thickness of the clayey calcareous ooze ranges 3–28 cm (average = 8 cm). The beds of calcareous clay are probably thicker than the thicknesses calculated here as they may be continuous across sections, but the presence of gaps does not allow the true bed thickness to be accurately determined.

3.3.2. Structure and texture

No distinct sedimentary structures were observed in the clayey calcareous ooze and the calcareous clay, but some beds of the darker calcareous clay do contain subtle parallel lamination and color banding in the upper part of Unit III (e.g., in Core 401-U1385K-19X).

Smear slides show that the dominant texture in both Unit III calcareous clay and clayey calcareous ooze is clay (Figures **F15**, **F16**). Unit III calcareous clay contains 0%–3% sand, 10%–20% silt, and 80%–90% clay, and the clayey calcareous ooze is very similar, with 1%–5% sand, 10% silt, and 85%–90% clay. The maximum grain size differs between lithologies; the clayey calcareous ooze tends to have fine sand-sized foraminifers, whereas the foraminifers are generally less abundant and finer grained in the calcareous clay, in which the maximum grain size is very fine sand.

3.3.3. Bioturbation and trace fossils

Unit III is characterized by generally more trace fossils than Unit II, with moderate bioturbation (mainly BI = 2–3) and occasionally abundant bioturbation (BI = 4). The trace fossil assemblage consists of abundant *Chondrites, Planolites*, and *Zoophycos*; frequent *Thalassinoides*; and rare *Palaeophycus*. The more conspicuous color change between calcareous clay and clayey calcareous ooze allows for better differentiation between darker and lighter colored infilled traces in the transition between two lithologies (Figure **F21**).

3.3.4. Composition and bulk mineralogy

Smear slides show that both calcareous clay and clayey calcareous ooze in Unit III contain mainly siliciclastic grains. However, the clayey calcareous ooze contains a greater proportion of carbonate (Figure **F19**). Calcareous clays comprise 70%–80% siliciclastic grains, 0%–10% detrital and/or authigenic carbonate, and 20%–30% biogenic carbonate, and the clayey calcareous ooze consists of 60% siliciclastic grains, 0%–5% detrital and/or authigenic carbonate, and 35%–40% biogenic carbonate. Comparison with XRD and coulometry data indicates that smear slide analysis underestimated the quantity of carbonate in Unit III clayey calcareous ooze (Figure **F12**). Minor glauconite and fish remains are common, along with very small quantities of pyrite.

XRD analysis was conducted on two clayey calcareous ooze and two calcareous clay samples from Unit III. The composition of clayey calcareous ooze and calcareous clay in Unit III is similar to those in the higher units. Based on the XRD and coulometry analyses of six samples from Unit III, the carbonate content generally decreases upward in Unit III (Figure **F12**), which corresponds well to the general increase in MS and NGR values in this unit on a large scale (see **Physical properties**; Figure **F8**). The organic carbon content is <1% in all four units and does not appear to vary consistently with lithology (Figure **F13**).

3.4. Discussion

3.4.1. Dominant sedimentary facies and depositional processes

At Site U1385, the dominant Pliocene lithologies recovered during Expeditions 339 and 397 were calcareous mud and calcareous clay, which were attributed to hemipelagic deposition (Expedition 339 Scientists, 2013; Hodell et al., 2024a) because of the combination of vertical (pelagic) settling and slow lateral advection of sediments across the continental margin. Expedition 401 coring of Holes U1385K and U1385L extended this record into the Messinian and late Tortonian. Clayey calcareous ooze and calcareous clay were identified in Units I–III. These deposits are interpreted to be deeper water sedimentary facies with a finer grain size relative to the Pliocene deposits, corresponding to sedimentation in a more pelagic setting (Hüneke and Henrich, 2011; Stow and Smillie, 2020; de Castro et al., 2021).

The dark calcareous clay of Unit I and the upper parts of Units II and III has subtle parallel lamination, low-angle cross lamination, and color banding (Figure **F14**). These characteristics are normally present in very fine grained contourites (Gonthier et al., 1984; Stow and Faugères, 2008;

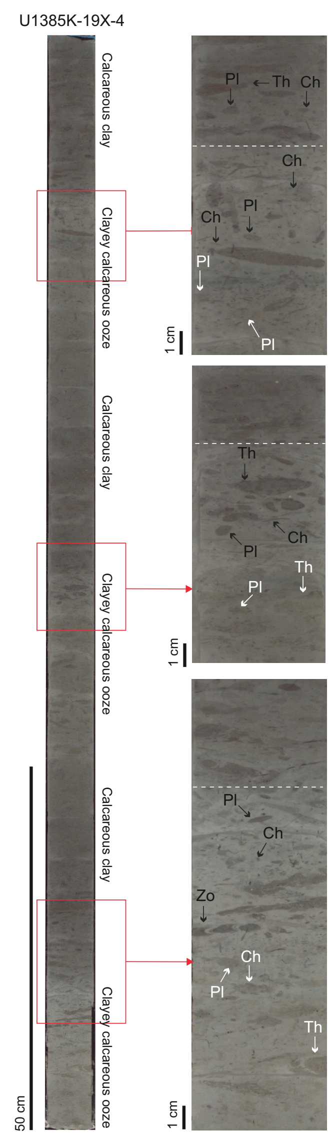

Figure F21. Alternating beds of clayey calcareous ooze (lighter facies) and calcareous clay (darker facies) in Unit III with details of trace fossils at contact between facies (dashed white lines), Hole U1385K. Note differentiation between dark (black arrows) and light (white arrows) trace fossil assemblages and penetration of dark traces into lighter sediments. Ch = *Chondrites*, Pl = *Planolites*, Th = *Thalassinoides*, Zo = *Zoophycos*.

Hüneke et al., 2021; Hernández-Molina et al., 2022; Rodríguez-Tovar, 2022), but the deposits in Holes U1385K and U1385L are finer grained than the contourites observed in previous studies. Nevertheless, the influence of bottom currents cannot be excluded because bedload transport and deposition of muds (made of clay- and silt-sized sediments) have been increasingly documented in flume experiments, modern muddy systems, and a growing number of detailed facies studies of ancient mudstone successions (Traykovski et al., 2000; Schieber et al., 2007; Yawar and Schieber, 2017; Li and Schieber, 2018). The observed parallel lamination and low-angle cross lamination in Units I and II (Figure **F14**) could be indicative of weak traction currents (weak bottom current processes?), which would explain the more common sharp contacts separating the clayey calcareous ooze from the overlying calcareous clay. Postcruise research will evaluate this hypothesis with detailed sedimentological analyses.

3.4.2. Trace fossils

The trace fossil assemblage (abundant *Chondrites, Planolites*, and *Zoophycos*; frequent *Thalassinoides*; rare *Palaeophycus*; and occasional *Asterosoma*, and *Spirophyton*) can be assigned to the *Zoophycos* ichnofacies. The *Zoophycos* ichnofacies is usually associated with fine-grained, low sedimentation rate, pelagic and hemipelagic, nonturbiditic sediments (MacEachern et al., 2007; Rodríguez-Tovar and Dorador, 2014; Dorador and Rodríguez-Tovar, 2015; Rodríguez-Tovar, 2022). This is consistent with low-energy settings. Variable bioturbation intensity (BI = 4–0) can result from changes in paleoenvironmental conditions. Typically, favorable conditions for macrobenthonic trace fossil maker communities are related to organic matter supply, sedimentation rate, and oxygen concentrations (i.e., in bottom water and at the sediment/water interface; Rodríguez-Tovar, 2022). The absence/scarcity of trace fossils in some intervals suggests some or all of these conditions were not present. The absence of bioturbation in laminated (parallel and cross lamination) intervals may be attributed to short periods of higher energy conditions, although other limiting factors of bioturbation (e.g., changes in sediment characteristics) cannot be fully discarded.

Similar trace fossil assemblages are observed in both the calcareous clay and clayey calcareous ooze, suggesting similar depositional and ecological conditions. The trace fossil assemblage appears to be unaffected by gradational to sharper contacts between lithologies. However, typically the trace fossil abundance is higher below the sharp contact between the clayey calcareous ooze and the overlying calcareous clay (Figure **F21**). This is particularly reflected by the lower bioturbation intensity in the calcareous clay directly overlying the clayey calcareous ooze, which can be associated with the higher energy conditions during the initial deposition of calcareous clay.

3.4.3. General sedimentary model

Site U1385 is located on a plateau, the Promontório dos Príncipes de Avis, on the lower continental slope of the southwestern Iberian margin (e.g., Terrinha et al., 2003; Maestro et al., 2015). This plateau represents an area without direct influence of submarine canyons or sedimentary input from slope deposition (see **Background and Objectives**; Figure **F1**), which is generally consistent with the dominant pelagic clayey calcareous ooze and calcareous clay deposits recovered. Precessional-scale climatic variability in the Quaternary sediments may have resulted in fluctuating carbonate and/or siliciclastic input, generating pelagic deposits with variations in carbonate content (Figures **F8**, **F20**) (Thomson et al., 1999; Lofi et al., 2016). The higher supply of detrital clays can be attributed to nepheloid layers containing significant amounts of suspended sediment, for example those associated with the Mediterranean Overflow Water (MOW) (Abrantes et al., 2000; Ambar et al., 2002; Magill et al., 2018).

Future research needs to evaluate the influence of regional water mass evolution in the dominant pelagic sedimentation at Site U1385, especially the interplay between the NEADW and the Antarctic Bottom Water (AABW) (van Aken, 2000; Hernández-Molina et al., 2011; Glazkova et al., 2022; Hodell et al., 2024a). This interplay would have been particularly important during the latest Miocene, a key period that marked the reorganization of intermediate and deepwater circulation into a pattern more similar to the one observed at present (Sykes et al., 1998; Billups, 2002; Nisancioglu et al., 2003; Uenzelmann-Neben et al., 2017; Hernández-Molina et al., 2017).

4. Biostratigraphy

Holes U1385K and U1385L were both washed down to start coring in Early Pliocene sediments. In Hole U1385K, an Early Pliocene assemblage was found in Sample 401-U1385K-2X-CC; however, the next four cores were empty, and no samples were obtained until Sample 7X-CC. An uninterrupted biostratigraphic record was recovered from Samples 7X-CC through 21X-CC, spanning from late Messinian to Tortonian (Figure **F22**; Tables **T3**, **T4**). Hole U1385L recovered the missing part of Hole U1385K, starting with Early Pliocene in Sample 401-U1385L-2X-CC (Table **T4**).

Samples from all Hole U1385K and U1385L core catchers were prepared and analyzed. Nannofossils and planktonic foraminifers were abundant and relatively well preserved in all samples (Tables **T5**, **T6**, **T7**, **T8**). Benthonic foraminifers were also analyzed in some of the samples (Table **T9**). The chronological framework for both Expedition 401 holes at Site U1385 was based on identifi-

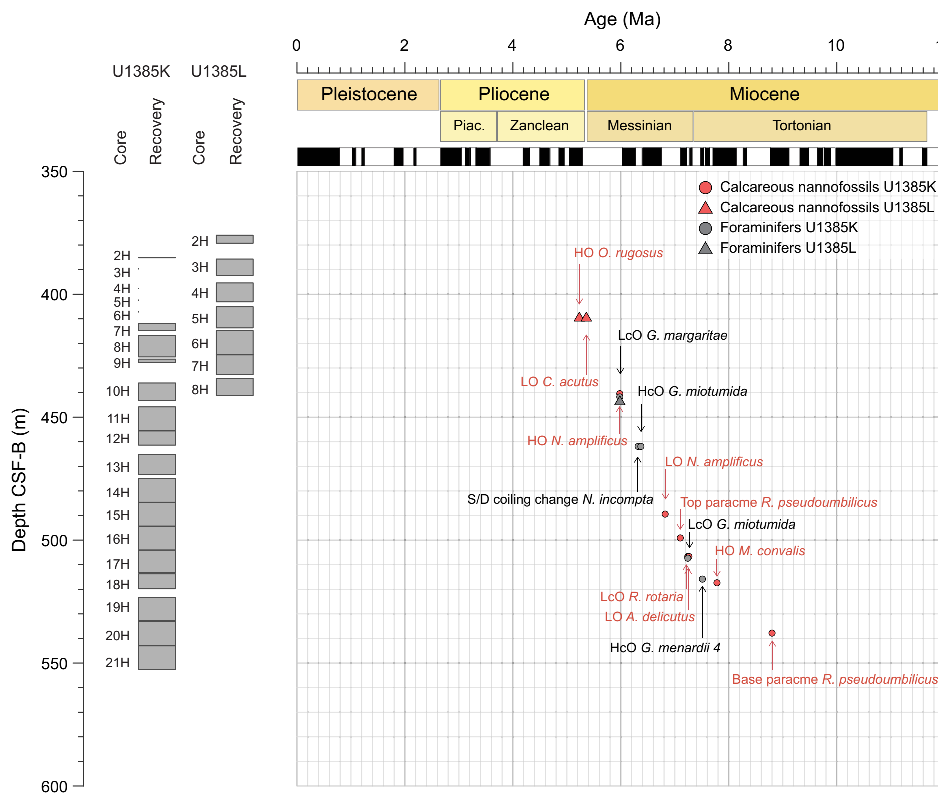

Figure F22. Biostratigraphic events, Site U1385. Events are plotted at their mean depth (Tables T3, T4). S/D = sinistral/dextral.

Table T3. Planktonic foraminifer biostratigraphic events, Holes U1385K and U1385L. LcO = lowest common occurrence, HcO = highest common occurrence, S/D = sinistral to dextral change in coiling. **Download table in CSV format.**

Events	Top core, section, interval (cm)	Bottom, core, section, interval (cm)	Top depth CSF-A (m)	Bottom depth CSF-A (m)	Mean depth CSF-A (m)	Top depth CSF-B (m)	Bottom depth CSF-B (m)	Mean depth CSF-B (m)	Age (Ma)
	401-U1385K-	401-U1385K-							
LcO *Globorotalia margaritae*	10X-3, 119–121	10X–5, 119-122	440.29	443.28	441.79	440.29	443.28	441.79	6.08
HcO *Globorotalia miotumida*	12X-4, 134–136	12X-5, 99–101	461.33	462.47	461.90	461.33	462.47	461.90	6.34
S/D coiling change of *Neogloboquadrina incompta*	12X-4, 134–136	12X-5, 99–101	461.33	462.47	461.90	461.33	462.47	461.90	6.37
LcO *Globorotalia miotumida*	17X-2, 114–116	17X-3, 117–119	506.62	508.11	507.37	506.62	508.11	507.37	7.24
LcO *Globorotalia menardii* 5	17X-4, 114–116	17X-5, 114–116	509.54	511.00	510.27	509.54	511.00	510.27	7.36
HcO *Globorotalia menardii* 4	18X-1, 119–121	18X-3, 19–21	514.91	516.83	515.87	514.91	516.83	515.87	7.51
	401-U1385L-	401-U1385L-							
LcO *Globorotalia margaritae*	8X-4, 99–101	8X-5, 121–123	439.71	441.43	440.57	439.71	441.43	440.57	6.08

cation of a series of calcareous nannofossil and planktonic foraminifer events (Tables **T3**, **T4**). The distribution of calcareous nannofossil and planktonic foraminifer events suggests that the Late Miocene–Pliocene stratigraphy recovered at Site U1385 is continuous (with no hiatuses).

4.1. Calcareous nannofossils

In addition to examining all core catchers from Holes U1385K and U1385L for calcareous nannofossil biostratigraphy, selected samples from Hole U1385K were analyzed to constrain bioevents, paying attention only to marker species. Calcareous nannofossil assemblages are abundant and

Table T4. Calcareous nannofossil biostratigraphic events, Holes U1385K and U1385L. HO = highest occurrence, LO = lowest occurrence, LcO = lowest common occurrence. **Download table in CSV format.**

Events	Top core, section, interval (cm)	Bottom core, section, interval (cm)	Top depth CSF-A (m)	Bottom depth CSF-A (m)	Mean depth CSF-A (m)	Top depth CSF-B (m)	Bottom depth CSF-B (m)	Mean depth CSF-B (m)	Age (Ma)
	401-U1385K-	401-U1385K-							
HO *Nicklithus amplificus*	10X-2, 142	10X-4, 134	441.92	439.01	440.47	441.92	439.01	439.01	5.98
LO *Nicklithus amplificus*	14X-CC	15X-CC	494.51	484.64	489.58	494.25	484.60	489.43	6.82
Top paracme *Reticulofenestra pseudoumbilicus*	16X-5, 88	16X-CC	504.15	501.04	502.60	503.95	500.90	502.43	7.10
LcO *Reticulofenestra rotaria*	17X-2, 62	17X-3, 34	507.26	506.08	506.67	507.26	506.08	506.67	7.24
LO *Amaurolithus delicatus*	17X-2, 62	17X-3, 34	507.26	506.08	506.67	507.26	506.08	506.67	7.26
HO *Minylitha convallis*	17X-CC	18X-CC	521.36	513.37	517.37	521.36	513.37	517.37	7.78
Base paracme *Reticulofenestra pseudoumbilicus*	19X-CC	20X-CC	542.95	532.91	537.93	542.75	532.91	537.83	8.80
	401-U1385L-	401-U1385L-							
HO *Orthorhabdus rugosus*	4X-CC	5X-CC	414.18	404.04	409.11	414.18	404.04	409.11	5.23
LO *Ceratolithus acutus*	4X-CC	5X-CC	414.18	404.04	409.11	414.18	404.04	409.11	5.36

Table T5. Nannofossil occurrences, Hole U1385K. **Download table in CSV format.**

Table T6. Nannofossil occurrences, Hole U1385L. **Download table in CSV format.**

Table T7. Planktonic foraminifer occurrences, Hole U1385K. **Download table in CSV format.**

Table T8. Planktonic foraminifer occurrences, Hole U1385L. **Download table in CSV format.**

Table T9. Percentage abundance of benthonic foraminifer assemblages in core catcher samples, Holes U1385K and U1385L. Percentage abundance is based on total count of between 85 and 120 benthonic foraminifers from each sample. *Cibicidoides* spp. and *Textularia* spp. make up the epibenthonic assemblage; Uvigerinids include *U. peregrina* and *U. hispida*. **Download table in CSV format.**

Core, section	Middle depth CSF-A (m)	Middle depth CSF-B (m)	Epibenthonic assemblage	Uvigerinids	*Globocassidulina subglobosa*	*Nuttalides umbonifera*
401-U1385K-						
2X-CC	385.90	385.90	21.95	10.37	1.83	1.22
6X-CC	407.21	407.21	20.00	13.85	3.85	0.77
8X-CC	425.94	425.94	24.07	12.04	5.56	1.85
10X-CC	444.43	444.43	28.21	5.13	5.13	1.28
12X-CC	463.01	463.01	31.76	8.24	1.18	2.35
14X-CC	484.62	484.58	9.35	5.61	17.76	0.93
16-X-CC	504.18	503.98	7.02	26.32	16.67	0.88
17X-CC	508.10	508.10	20.00	2.22	22.22	2.22
19X-CC	532.89	532.89	7.35	2.94	19.85	11.76
21X-CC	552.63	552.48	16.05	3.70	4.94	2.47
401-U1385L-						
3X-CC	393.72	393.72	18.75	9.82	1.79	17.86
4X-CC	404.02	404.02	29.41	7.84	5.88	1.96
5X-CC	414.21	414.21	27.66	24.47	0.00	10.64
6X-CC	424.64	424.48	23.66	7.53	13.98	0.54

diverse, and preservation is good. Small placolith species (<3 μm) dominate most of the assemblage. Inorganic input and reworked species are rare in a few of the samples analyzed (Tables **T5**, **T6**).

Two nannofossil events were defined in Hole U1385L, and six events were found in Hole U1385K (Raffi et al., 2006 and references therein; Hilgen et al., 2000a). In Hole U1385L, the highest occurrence (HO) of *Orthorhabdus rugosus* and lowest occurrence (LO) of *Ceratolithus acutus* were both recorded between Samples 401-U1385L-4X-CC and 5X-CC (mean depth = 409.11 m core depth below seafloor, Method B [CSF-B]). These two events are close in astronomical age (HO of *O. rugosus*, 5.23 Ma; LO of *C. acutus*, 5.36 Ma) (Raffi et al., 2006). Postexpedition high-resolution counts will better define their stratigraphic position.

In Hole U1385K, the first event recorded is the HO of *Nicklithus amplificus* between Samples 401-U1385K-10X-2, 142 cm, and 10X-4, 134 cm (mean depth = 440.47 m CSF-B) (Table **T4**). The LO of *N. amplificus* is recorded between Samples 14X-CC and 15X-CC (mean depth = 489.43 m CSF-B). The next recorded event is the top of the *Reticulofenestra pseudoumbilicus* paracme, a globally recognized event, between Samples 16X-5, 88 cm, and 16X-CC (mean depth = 502.43 m CSF-B).

To better constrain the nannofossil chronology for this site in the latest Tortonian, the LO of *Amaurolithus delicatus* and the lowest common occurrence (LcO) of *Reticulofenestra rotaria* were considered (see **Biostratigraphy** in the Expedition 401 methods chapter [Flecker et al., 2025a]). Comparison of different sections in the Mediterranean suggests that these events are reproducible and reliable in adjacent geographic areas (Morigi et al., 2007; Hilgen et al., 2000a). They have an astronomical age between 7.24 and 7.26 Ma (Hilgen et al., 2000a) and are therefore biostratigraphically helpful for the latest Tortonian interval (Morigi et al., 2007; Hilgen et al., 2000a). Both events are recorded in Hole U1385K, occurring between Samples 17X-2, 62 cm, and 17X 3, 34 cm (mean depth = 506.67 m CSF-B).

Two geologic timescale 2020 (GTS2020) events (Raffi et al., 2020) are also recorded in Hole U1385K: the HO of *Minylitha convallis* and the base of the paracme of *R. pseudoumbilicus* between Samples 17X-CC and 18X-CC (mean depth = 517.37 m CSF-B) and between Samples 19X-CC and 20X-CC (mean depth = 537.83 m CSF-B) (Table **T4**), respectively. These two events give a minimum age for the bottom of the hole of 7.78–8.8 Ma.

4.2. Planktonic foraminifers

Planktonic foraminifers are well preserved in the sedimentary succession recovered with evidence of some fragmentation. Bioevents were identified by analyzing every core catcher with additional samples taken from working halves between core catcher samples to better constrain their position. Because there are no planktonic foraminifer bioevents close to the Miocene/Pliocene boundary, the first event identified in this record is the LcO of *Globorotalia margaritae*. This event (dated at 5.98 Ma) is recorded between Samples 401-U1385K-10X-3, 119–121 cm, and 10X-5, 119–121 cm (mean depth = 441.79 m CSF-B), and between Samples 401-U1385L-8X-4, 99–101 cm, and 8X-5, 121–123 cm (mean depth = 440.57 m CSF-B) (Table **T3**). It becomes common in the foraminifer assemblage at 5.98 Ma as reported by Bulian et al. (2023). Although the age for the first occurrence of this species is dated at 6.08 Ma in the GTS2020, we used the age provided by Bulian et al. (2023) for a significant increase in abundance of this species.

In the latest Messinian, neogloboquadrinid coiling was dextral, but some sinistral specimens were found downcore that are related to the successive coiling changes in *Neogloboquadrina incompta* (Krijgsman et al., 2004; Bulian et al., 2023). The first sinistral to dextral coiling change in *N. incompta* during the Messinian was recorded between Samples 401-U1385K-12X-4, 134–136 cm, and 12X-5, 99–101 cm (mean depth = 461.90 m CSF-B). This event was not recorded in Hole U1385L because drilling did not reach this depth. Together with *N. incompta*, abundant specimens of other species such as *Neogloboquadrina atlantica* were found. Influxes of this species with sinistral and dextral coiling were found in some samples that could potentially be used in future biostratigraphic studies. The highest common occurrence (HcO) of *Globorotalia miotumida* was also recorded at the same position as the coiling change in *N. incompta*. This was expected because the events are almost contemporaneous. Indeed, the best way to identify the first coiling change of *N. incompta* is the identification of frequent specimens of *G. miotumida* in the same sample because after this point their abundance is drastically reduced. Abundant sinistral specimens of *N. incompta* were recorded in Sample 401-U1385L-8X-5, 121–123 cm (441.43 m CSF-B). This peak in abundance of sinistral *N. incompta* must be related to some of the fluctuations in coiling after the first coiling change because this sample does not contain *G. miotumida*.

The Tortonian/Messinian boundary, which is coincident with the LcO of *G. miotumida*, is recorded between Samples 401-U1385K-17X-2, 114–116 cm, and 17X-3, 117–119 cm (mean depth = 507.37 m CSF-B). The age for this event is 7.24 Ma. Immediately below the LcO of *G. miotumida*, *Globorotalia menardii* 5 drastically decreases in abundance, although the low-resolution sampling did not allow us to identify this event. This species usually coexists with *G. miotumida* in the northeast Atlantic during a short period of less than a single precession cycle. We did not use this bioevent here because it occurred only a few thousand years later than the LcO of *G. miotumida*. The LcO of *G. menardii* 5, typically with dextral coiling (dated at 7.36 Ma), is recorded between Samples 17X-4, 114–116 cm, and 17X-5, 114–116 cm (mean depth = 510.27 m CSF-B). The depth of this event may not be very precise; quantification at higher spatial resolution is needed to locate it better.

The HcO of *G. menardii* 4 (7.51 Ma) is located between Samples 401-U1385K-18X-1, 119–121 cm, and 18X-3, 19–21 cm (mean depth = 515.87 m CSF-B) (Table **T3**). Better quantification with a higher resolution biostratigraphic study is also needed to identify this event more precisely.

No other planktonic foraminifer bioevents are identified below 7.51 Ma. However, the low sedimentation rates and large number of (probably precessional) cycles visible in the physical properties data indicate that the bottom of Hole U1385K is likely to be Tortonian, probably around 8.8 Ma.

4.3. Benthonic foraminifers

A total of 10 core catchers from Hole U1385K and 4 core catchers from Hole U1385L were processed and studied for the abundance of more than 64 species of benthonic foraminifers. The level of preservation of the benthonic foraminifers was noted along with their abundance with respect to planktonic ones.

The >150 µm fraction of washed samples was analyzed for calcareous microfossil content. Although preservation of the foraminifers is good in all the samples analyzed, benthonic foraminifer specimens are rare. Benthonic foraminifers are <4% of the total foraminifer population in most samples, indicating that the site is deeper than 1200 m throughout the interval recovered, consistent with the water depth today of 2585 m. The benthonic foraminifer fauna mainly belong to the genera *Cibicidoides, Globocassidulina, Gyroidinoides, Lenticulina, Melonis, Nuttalides, Oridorsalis, Pullenia, Sigmoilopsis, Stilostomella*, and *Uvigerina* in varying proportions. The absence of shallow-water benthonic species in the samples indicates that the benthonic fauna is autochthonous and indicative of bottom water conditions.

The abundance of the elevated epibenthonic species like those of *Cibicidoides* spp. and *Textularia* spp. is between 7% and 25% in most samples with a high of 32% in Sample 401-U1385K-12X-CC (Figure **F23**; Table **T9**). Study of recent benthonic foraminifer assemblages from the Gulf of Cádiz region have shown that the abundance of elevated epibenthonic species is positively correlated with bottom water current velocities, and the elevated epibenthonic assemblages in the Gulf of Cádiz region have been used as an indicator for MOW (Schönfeld, 1997, 2002a, 2002b; Schönfeld and Zahn, 2000). The low abundance of the elevated epibenthonics at Site 401-U1385 suggests the site was not directly under the effect of MOW or any high-velocity current in the studied interval.

Globocassidulina subglobosa is a species that thrives in oligotrophic environments with episodic input of phytodetritus (Gooday, 1993; Szarek et al., 2007). It makes up to 17%–23% of the benthonic fauna between Samples 401-U1385K-14X-CC (mean depth = 484.58 m CSF-B) and 19X-CC (mean depth = 532.49 m CSF-B) (Figure **F23**; Table **T9**).

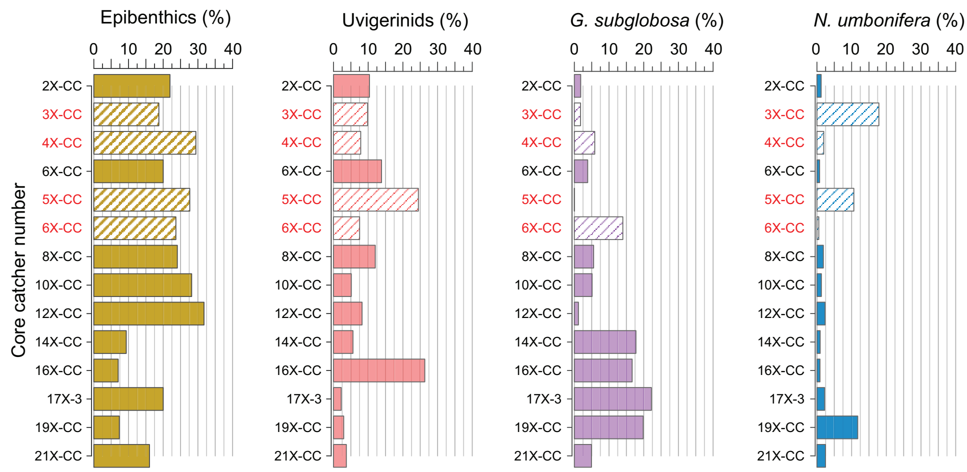

Figure F23. Abundance of benthonic foraminifer assemblages based on total counts between 85 and 120 benthonic foraminifers from each sample, Holes U1385K (black text; solid colors) and U1385L (red text; dashed lines). They are arranged in depth order as determined from splice between the two holes (see Stratigraphic correlation and age model). *Cibicidoides* spp. and *Textularia* spp. make up epibenthonic assemblage; Uvigerinids include *U. peregrina* and *U. hispida* (Table T9).

Uvigerinids have been associated with high surface water productivity and low bottom water oxygen content by previous workers (Zhu, 2001). *Uvigerina peregrina* and *Uvigerina hispida* are the common Uvigerinids at Site 401-U1385, and their abundances are low compared to the other Expedition 401 sites (ranging 2%–10% in most samples). However, they become more abundant (24%–26%) in Samples 401-U1385L-5X-CC (mean depth = 414.21 m CSF-B) and 401-U1385K-16X-CC (mean depth = 503.98 m CSF-B) (Figure **F23**; Table **T9**).

The presence of *Nuttalides umbonifera* is noted in all samples, although it is common (>17% abundance) only in Sample 401-U1385L-3X-CC (mean depth = 393.715 m CSF-B) (Figure **F23**). *N. umbonifera* has been associated with AABW in the modern ocean (Hodell et al., 1985).

The present study is quite low resolution, but preliminary results indicate that with higher resolution sampling it will be possible to identify periods of oxygen-rich/-poor bottom waters and eutrophic/oligotrophic environment and evaluate the likely impact of AABW/North Atlantic Deep Water at the site.

5. Paleomagnetism

Paleomagnetic investigation of 16 cores from Hole U1385K and 7 cores from Hole U1385L focused on demagnetization of the natural remanent magnetization (NRM) of archive-half split core sections and discrete samples of the working-half split core sections. Pass-through paleomagnetic measurements were performed using the superconducting rock magnetometer (SRM) to investigate the NRM on a total of 132 archive halves (91 archive halves from Hole U1385K and 41 archive halves from Hole U1385L). No pass-through measurements were made on core catcher sections. Alternating field (AF) demagnetization was performed on the SRM by applying stepwise peak fields of 5, 10, 15, and 20 mT, with measurement of the remaining magnetization taken at 2 cm resolution. SRM measurements were sporadically disturbed by the occurrence of artificial flux-jumps; these results were removed from the database. Next, the SRM data were processed to remove all measurements collected from anomalous peak intensity intervals and all measurements that were made within 5 cm of the section ends, which are biased by measurement edge effects. A moving window of 1 m was used for smoothing the inclination values to suppress the influence of data points that deviate significantly from the expected geocentric axial dipole (GAD) inclination (57°) at the site latitude (37.3°N). The processed NRM, inclination, and intensity data after 20 mT peak field AF demagnetization are shown in Figures **F24** and **F25** and listed in PMAG in **Supplementary material** and Tables **T10** and **T11**.

A total of 117 discrete oriented cube samples were collected from the working-half sections using an extruder. For each core, 3–7 discrete samples were taken, avoiding visually disturbed intervals. First, the anisotropy of magnetic susceptibility (AMS) and bulk MS were measured on all samples using the MFK2 KappaBridge unit. Next, the NRM of 61 cube samples (47 samples from Hole U1385K and 14 samples from Hole U1385L) was measured on the AGICO JR-6A spinner magnetometer. Stepwise AF demagnetization was performed at successive peak fields of 0, 5, 10, 15, 20, 30, 40, 50, 60, and 70 mT up to a maximum of 80 mT for the Hole U1385K samples and up to a maximum of 40 mT for the Hole U1385L samples where the magnetic signal was weaker (similar to the equivalent upper part of Hole U1385K). When magnetization became erratic, demagnetization was stopped. The inclination data after 20 mT peak field AF demagnetization of the discrete samples are displayed in Figures **F24** and **F25** and listed in Tables **T12** and **T13**.

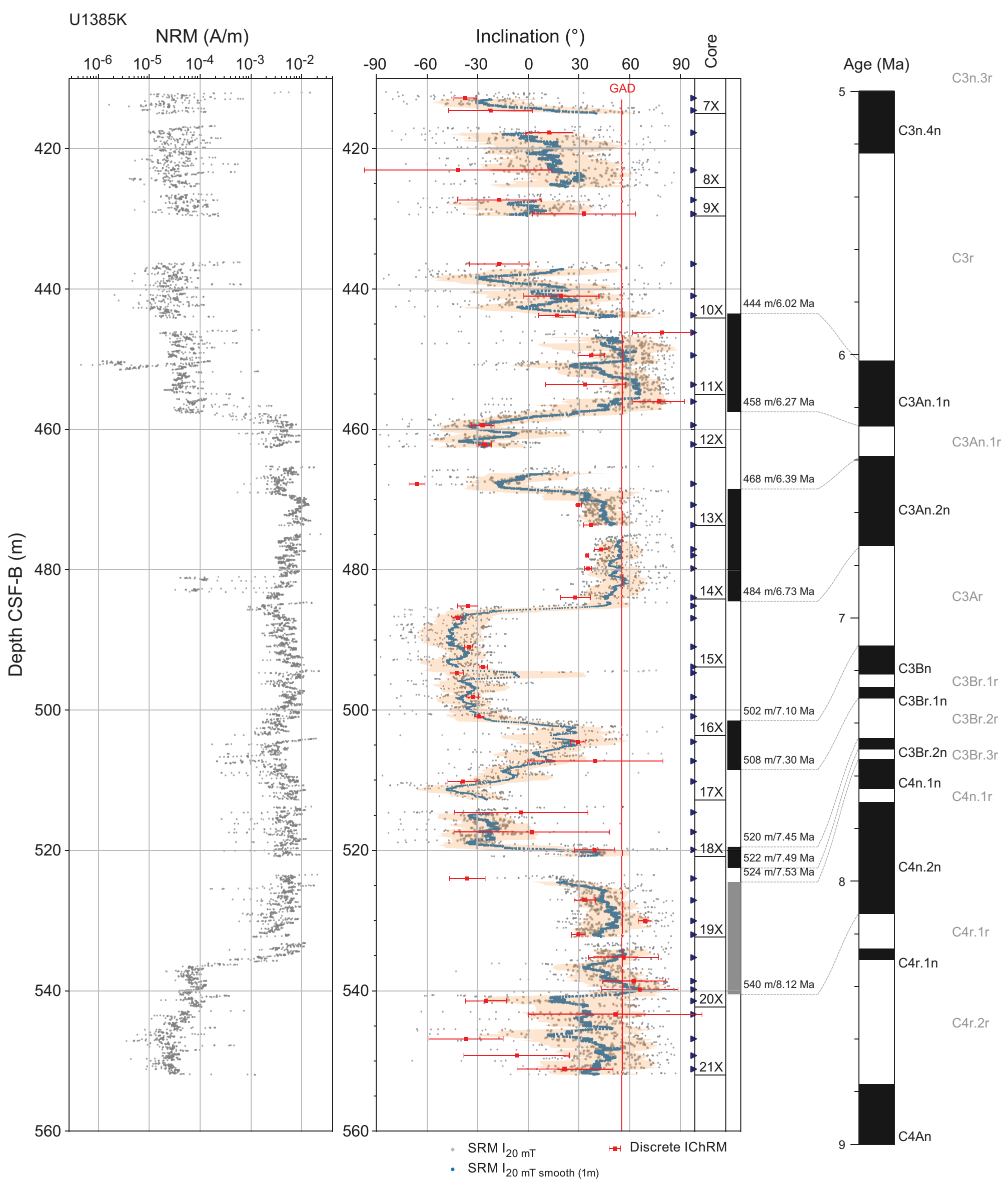

Figure F24. Paleomagnetic results, Hole U1385K. Red vertical line = GAD inclination at site latitude in normal polarity. Smoothed inclination used 1 m moving window. Orange band = standard deviation of smoothing results. ChRM inclination of discrete samples have α_{95} uncertainties. Blue triangles = discrete sample positions. Chron columns: black = normal polarity, white = reversed polarity, gray = zones of uncertain normal polarity. Lines and numbers along interpreted chron column = tie points between hole and GPTS. Dashed lines between hole and GPTS = best-fit correlation of uncertain polarity boundaries.

5.1. Paleomagnetic signals

AMS results for both Holes U1385K and U1385L show an overall vertical direction of the K_{min} axis in agreement with a sedimentary fabric of horizontal strata and a vertical drill hole (Figure **F26**).

The NRM intensity measured on the SRM in Hole U1385K ranges from about 1.0 × 10^{-4} to 1.0 × 10^{-1} A/m and exhibits values between 455 and 535 m CSF-B, that are two orders of magnitude higher than the overlying and underlying cores (Figure **F24**). The high-intensity signal is most likely related to the presence of magnetite in the sediment and different paleoenvironmental conditions on the seafloor. Based on the SRM inclination records after 20 mT demagnetization, Hole U1385K shows several polarity reversals. At least four normal polarity intervals and five reversed

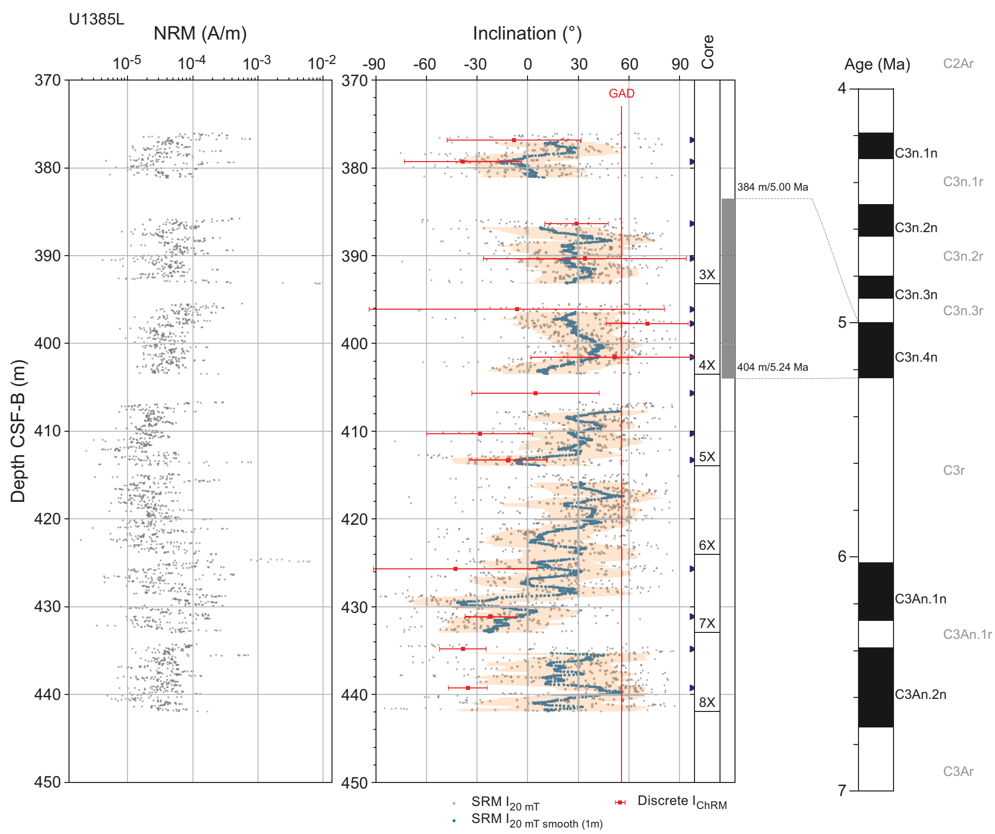

Figure F25. Paleomagnetism after 20 mT AF demagnetization, Hole U1385L. Red vertical line = GAD inclination at site latitude in normal polarity. Smoothed inclination used 1 m moving window. Orange band = standard deviation of smoothing results. ChRM inclination of discrete samples have α_{95} uncertainties. Blue triangles = discrete sample positions. Chron columns: black = normal polarity, white = reversed polarity, gray = zones of uncertain normal polarity. Lines and numbers along interpreted chron column = tie points between Hole U1385K and GPTS. Dashed lines between hole and GPTS = best-fit correlation of uncertain polarity boundaries.

Table T10. Paleomagnetic results of SRM measurements after 20 mT peak field AF demagnetization, Section 401-U1385K-7X-1. **Download table in CSV format.**

Table T11. Paleomagnetic results of SRM measurements after 20 mT peak field AF demagnetization, Section 401-U1385L-3X-1. **Download table in CSV format.**

Table T12. Paleomagnetic results of JR-6A spinner measurements of discrete samples after AF demagnetization at 20 mT, Hole U1385K. **Download table in CSV format.**

Table T13. Paleomagnetic results of JR-6A spinner measurements of discrete samples after AF demagnetization at 20 mT, Hole U1385L. **Download table in CSV format.**

polarity intervals are easy to identify (Figure **F24**). NRM intensities of the discrete samples from Hole U1385K range 1.3 × 10^{-5} to 5.1 × 10^{-2} A/m, and demagnetization diagrams (Z-plots) are mostly straightforward to interpret (Figure **F27**). Detailed analyses showed that a normal polarity overprint component was generally removed between 0 and 10 mT, which is probably related to an overprint caused by the core drilling (Acton et al., 2002). After demagnetization at 20 mT, a second component remained with inclinations clustering approximately around normal and reversed polarities. We interpret this to be the characteristic remanent magnetization (ChRM) component. The ChRM component of most samples was successively demagnetized at higher applied magnetic fields up to 80 mT and generally shows a linear decay in magnetization, suggesting magnetite is the main magnetic mineral (Figure **F27**). The inclinations of the discrete samples at 20–40 mT are generally coherent and confirm the polarities suggested by the SRM inclination values (Figure **F24**).

SRM measurements for Hole U1385L show NRM intensity ranging 1 × 10^{-4} to 5 × 10^{-3} A/m, similar to the upper part of Hole U1385K. The inclination record at 20 mT shows only shallow (between −30° and +30°) values, indicating that the primary magnetic components are not properly resolved (Figure **F25**). NRM intensities of the discrete samples from Hole U1385L are also relatively weak and range 7.1 × 10^{-5} to 1.6 × 10^{-4} A/m. Demagnetization of these samples shows less stable components in the Z-plots and was discontinued after 40 mT (Figure **F27**). The inclinations of the discrete samples at 20 mT indicate a normal polarity interval at 384–404 m CSF-B enclosed between reversed polarity intervals (Figure **F25**).

5.2. Magnetostratigraphy

Inclination values of both SRM measurements after 20 mT and JR-6A reveal the magnetostratigraphic pattern in Holes U1385K (Figure **F24**) and U1385L (Figure **F25**), which were then combined and correlated to the most recent geomagnetic polarity timescale (GPTS 2020; Raffi et al., 2020) to obtain magnetostratigraphic age constraints for the observed polarity reversals and the core sections and to calculate sediment accumulation rates (Table **T14**).

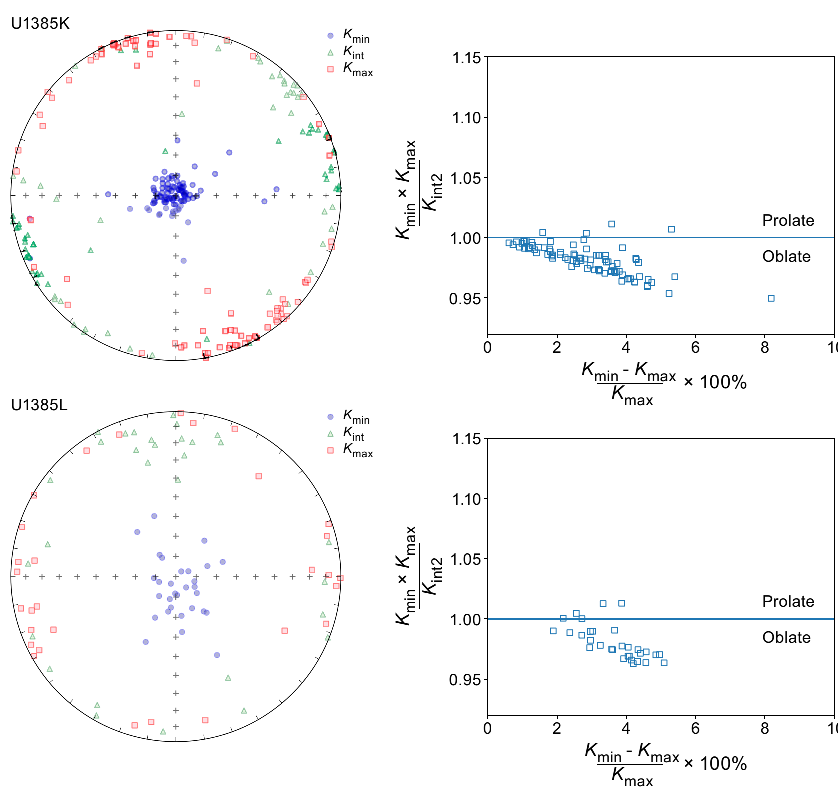

Figure F26. AMS determinations, Holes U1385K and U1385L. Left: orientation of principal AMS axes K_{max}, K_{int}, and K_{min}. Right: shape factor of AMS ellipsoid versus AMS degree.

The JR-6A discrete sample data for the upper part of Hole U1385L show negative inclinations in Core 401-U1385L-2X and positive inclinations in Cores 3X and 4X (384–404 m CSF-B). In the following interval (404–444 m CSF-B), negative inclinations are dominant in both the Hole U1385L and U1385K records, even though inclination values of the SRM records do not approach the expected antipodal GAD inclination at the coring site (−57°), and the results of the discrete samples are also somewhat scattered (Figures **F24**, **F25**). This interval is also poorly resolved in the partly overlapping SRM data of Holes U1385F–U1385H and U1385J (Expedition 397; Hodell et al.,

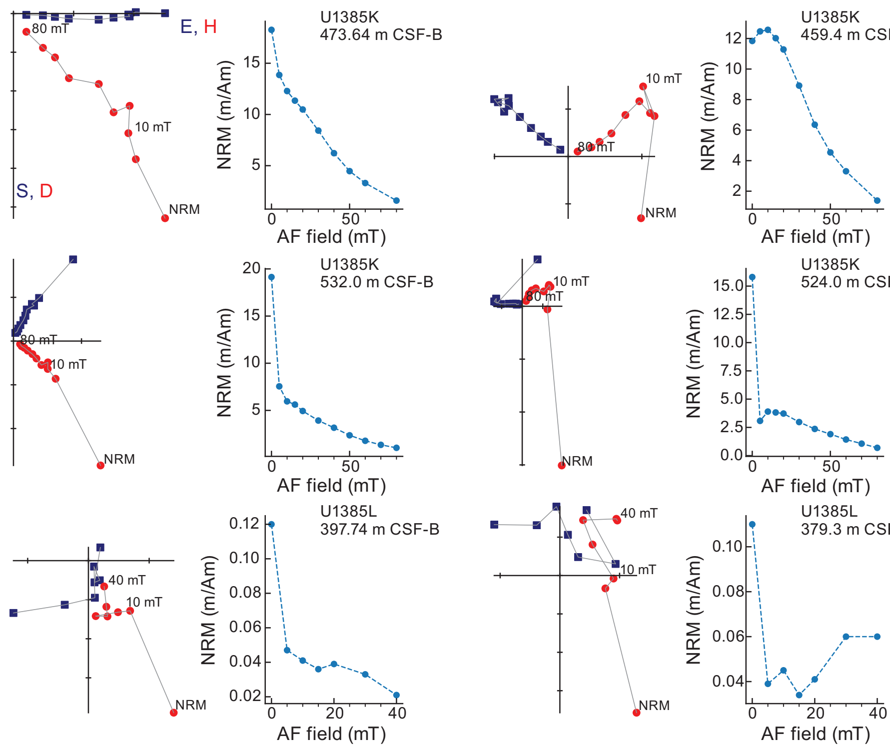

Figure F27. AF demagnetization results, Holes U1385K and U1385L. Left: vector endpoints of paleomagnetic directions measured after each demagnetization treatment on an orthogonal projection (Zijderveld) plot. Examples of normal (positive inclinations) and reversed (negative inclinations) polarity are shown in left and right panels, respectively. Squares = horizontal projections, circles = vertical projections. Right: intensity variation with progressive demagnetization.

Table T14. Magnetostratigraphic results showing depth estimates for correlative GPTS reversals, Holes U1385K and U1385L. * = greater degree of uncertainty. x = not detected. **Download table in CSV format.**

Chron	GPTS 2020 Age (Ma)	Hole U1385K JR-6A depth (m)	Hole U1385L SRM depth (m)
C3n.3r	5	381–386	x
C3n.1n (Thvera)	5.23	402–406	x
C3r	6.02	440–445	440–445
C3An.1n	6.27	456–459	457–458
C3An.1r	6.39	468–471	468–469
C3An.2n	6.73	484–485	484–485
C3Ar	7.1	501–504	501–502
C3Bn	7.21	x	x
C3Br.1r	7.26	x	x
C3Br.1n	7.31	507–510*	507–510*
C3Br.2r	7.46	518–520*	519–520*
C3Br.2n	7.5	521–524*	x
C3Br.3r	7.54	524–525*	x
C4n.1n	7.65	x	x
C4n.1r	7.7	x	x
C4n.2n	8.13	540–541*	x
C4r.1r	8.26	x	x
C4r.1n	8.3	x	x

2023). Knowing from the previous results of Expedition 397 that we started coring in the lowermost Pliocene, the reversed–normal–reversed polarity sequence most likely corresponds to Chrons C3n.3r, C3n.4n (Thvera), and C3r, respectively. Below this, four intervals with normal polarity and three intervals of reversed polarity are well established in Hole U1385K and demagnetization results from discrete samples are straightforward. The upper two normal polarity intervals at 444–458 and 468–484 m CSF-B correlate to Chrons C3An.1n and C3An.2n, respectively. The next normal polarity interval at 502–508 m CSF-B most likely correlates to the Chron C3Bn–C3Br.1n interval in which the Tortonian/Messinian boundary is defined (Hilgen et al., 2000b; see **Paleomagnetism** in the Expedition 401 methods chapter [Flecker et al., 2025a]). This is in good agreement with the determination of the LcO of the *G. miotumida* group between 506.6 and 508.1 m CSF-B in Hole U1385K (Table **T3**), the planktonic foraminifer bioevent that closely coincides with this stage boundary. The lowermost normal polarity intervals (520–522 and 524–540 m CSF-B) correlate best with the Chron C3Br.2n–C3n.2n interval, indicating that the multiple short (20–30 ky) polarity intervals in the latest Tortonian part of the GPTS are not well resolved, probably because the resolution of discrete samples is too low and as a result of poor determination of magnetic components in the SRM records. The reversed polarities of the discrete samples of the lowermost Core 401-U1385K-21X imply that the base of Hole U1385K is older than 8.2 Ma. The interval with high-intensity NRM signals is dated between 7.8 and 6.3 Ma.

The magnetostratigraphic correlation of the observed polarity pattern to GPTS 2020 was used to calculate sediment accumulation rates for the combined record of Holes U1385K and U1385L (Figure **F28**). This curve indicates an average accumulation rate of ~5 cm/ky for the Messinian part of the record.

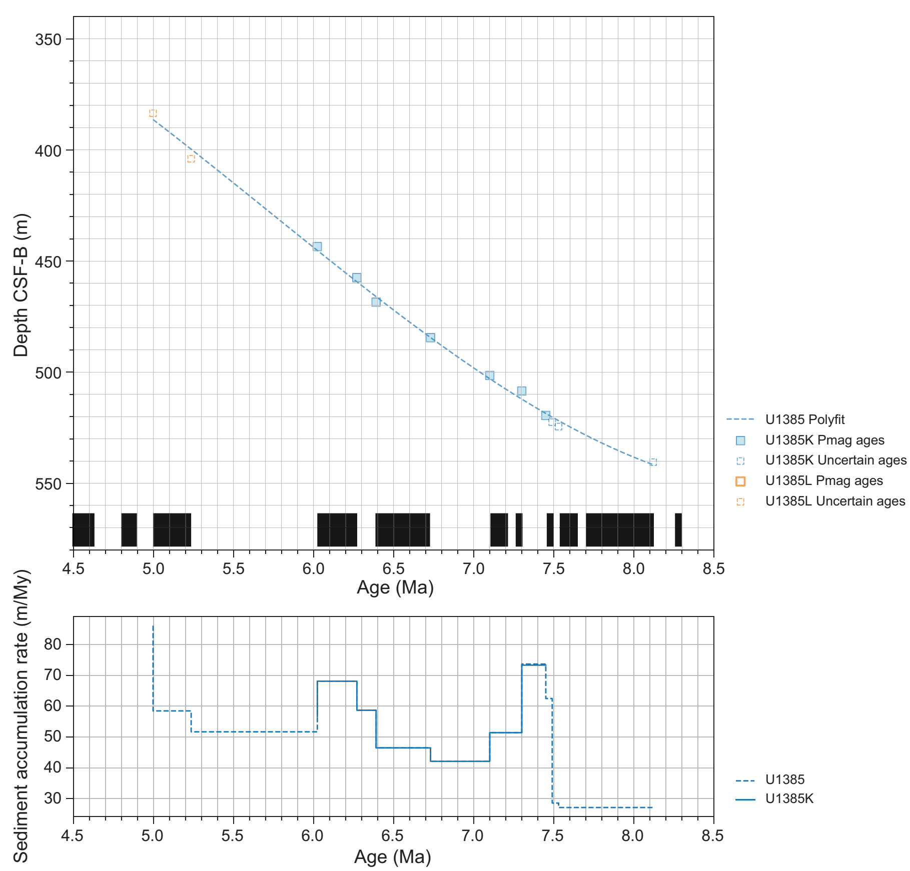

Figure F28. Sediment accumulation curve resulting from magnetostratigraphic correlations to GPTS 2020 (Raffi et al., 2020), Holes U1385K and U1385L. Squares with solid lines = well-established reversals, squares with dashed lines = uncertain ages. Ages are fitted to polynomial of 3° using least squares method.

6. Geochemistry

6.1. Volatile hydrocarbons

Headspace gas analysis was performed as part of the standard protocol required for shipboard safety and pollution prevention monitoring. A total of 16 headspace samples were analyzed from Hole U1385K, 1 sample per recovered core (Figure **F29**; Table **T15**). Methane (C_1) at 23,688 parts per million by volume (ppmv) and ethane (C_2) at <1 ppmv were detected in the shallowest Sample 401-U1385K-2X-1, 0 cm; thereafter, only lower levels of methane were detected. These concentrations of volatile hydrocarbons do not present a drilling concern. Headspace analyses were not repeated in Hole U1385L, which targeted a depth range that overlapped Hole U1385K. Comparison with earlier drilling of shallower stratigraphy in Expedition 397 Hole U1385G (Hodell et al., 2024a) shows the overlying zone of methanogenesis by microbial degradation of organic matter (Figure **F29**).

6.2. Interstitial water chemistry

IW was extracted from a total of 13 whole-round samples from Hole U1385K at a sampling resolution of 1 sample per XCB core (Tables **T16**, **T17**). Samples for IW analyses were not collected in Hole U1385L, which overlapped the depth range of Hole U1385K. Data from Hole U1385K are presented in comparison to those from Expedition 397 Hole U1385G (Hodell et al., 2024a), which recovered IW samples from 0 to 395 m CSF-A. Some IW analyses were also performed during Expedition 339 in Holes U1385A and U1385B over the uppermost 150 m (Expedition 339 Scientists, 2013), but these data overlap with the records from Hole U1385G and are therefore not presented here. No mudline water or bottom water samples were available, so geochemical properties are compared to the International Association for the Physical Sciences of the Oceans (IAPSO) seawater standard where relevant. Figure **F30** shows comparisons between several of the IW analyses.

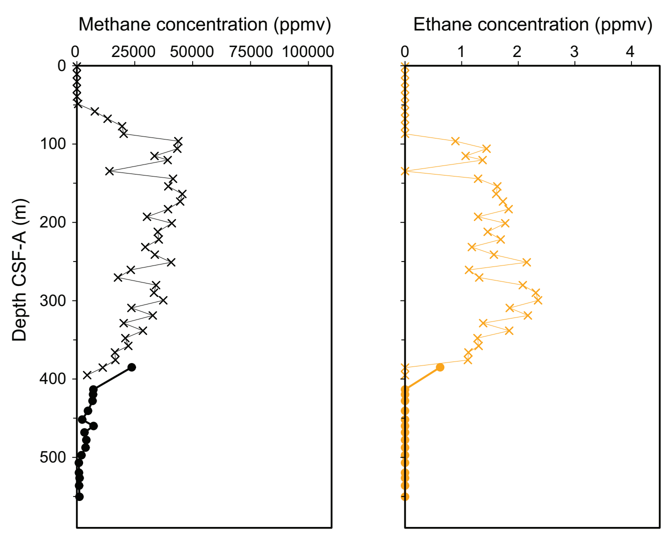

Figure F29. Headspace gas methane and ethane, Hole U1385K. Results from overlying Pliocene–Pleistocene sequence from Expedition 397 Hole U1385G are shown for comparison (Hodell et al., 2024a).

Table T15. Gas concentrations, Hole U1385K. **Download table in CSV format.**

Table T16. Geochemical properties measured for liquid phase, Hole U1385K. **Download table in CSV format.**

Table T17. Geochemical properties measured by ICP-AES for liquid phase, Hole U1385K. **Download table in CSV format.**

6.2.1. Alkalinity, pH, and salinity

Alkalinity decreases from a maximum of 4.8 mM at 419.6 m CSF-A (Section 401-U1385K-8X-2) to a minimum of 1.8 mM at 519.5 m CSF-A (Section 18X-4) (Figure **F31**; Table **T16**). Comparison with data from shallower stratigraphy in Hole U1385G (Hodell et al., 2024a) shows that the initial trend of decreasing alkalinity in Hole U1385K is the tail of the decline in alkalinity below approximately 250 m CSF-A before values stabilize around 2.4 mM. We interpret the decrease in alkalinity to be predominantly caused by formation of authigenic silicates, which consume sodium, magnesium, and potassium, despite net carbonate dissolution as indicated by the increase in calcium during this interval (Figure **F30**).

Values for pH for Hole U1385K range from a minimum of 7.5 to a maximum of 7.7 (mean = 7.6) (Figure **F31**). The pH data are also best understood in context with the overlying trend reported from Hole U1385G (Hodell et al., 2024a), with a continuous decline in pH below approximately 50 m CSF-A, where the sulfate–methane transition zone (SMTZ) is located (Figure **F30**). Salinity is 32 throughout Hole U1385K (Figure **F32**; Table **T16**).

6.2.2. Major ions

Major ion concentrations (Na^+, Cl^-, Ca^{2+}, Mg^{2+}, K^+, $SO_4{}^{2-}$, and Br^-) of IW were analyzed by ion chromatography (IC) (Table **T16**). Sodium and chloride are constant; the mean values are 494.7 and 583.6 mM, respectively (Figure **F32**). The Na/Cl ratio range is 0.84–0.85. Comparison to shallower IW samples in Hole U1385G (Hodell et al., 2024a) shows consistent Na/Cl ratios but an unexplained offset of approximately 5% in both sodium and chloride concentrations between the data sets from the two different expeditions. It is likely that these offsets, which are also visible in other conservative elements (e.g., Br; Figure **F33**), are an artifact of analytical methods (e.g., poor pipette calibrations or evaporation during preparation of solutions) during sample or standard preparation. The artifact is probably present for nonconservative elements as well, although the

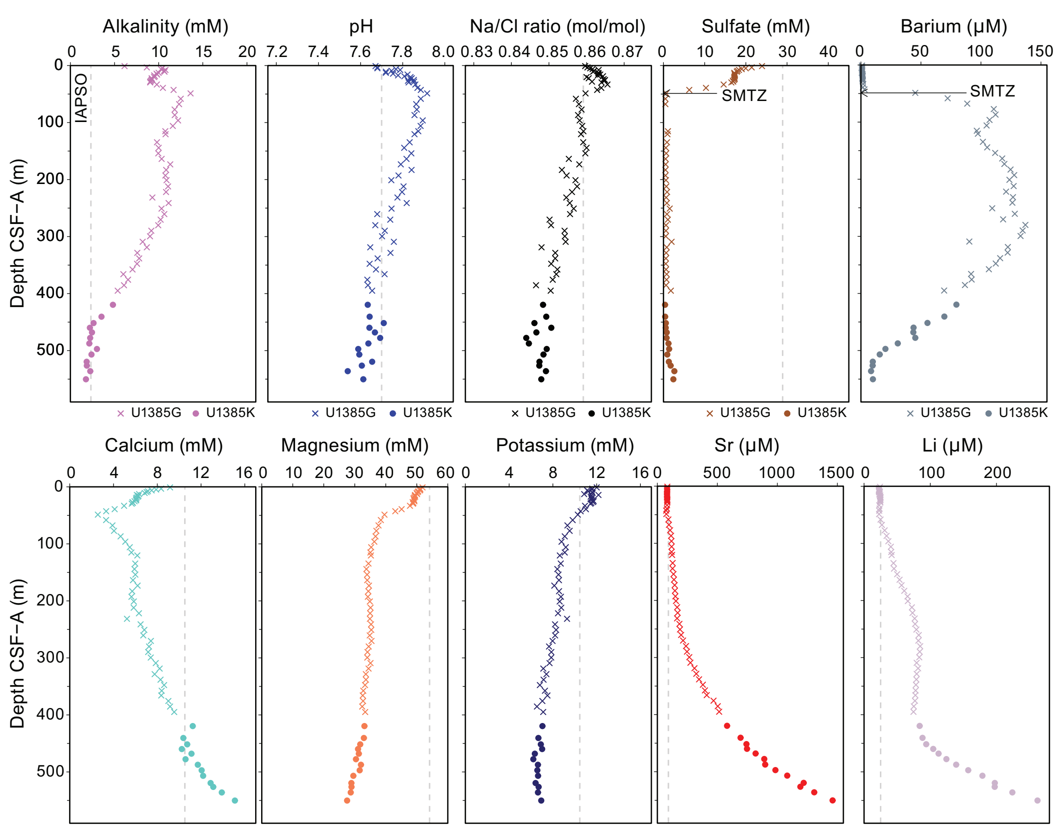

Figure F30. Comparison of several key chemical profiles from IW, Hole U1385K. Expedition 397 Hole U1385G data are also shown (Hodell et al., 2024a). Dashed line = IAPSO standard seawater.

much greater relative changes for reactive elements largely obscure the small (~5%) effect that is most easily observed in the stable concentration profiles of the most conservative elements. For comparisons of IW concentration data between Holes U1385G and U1385K, normalization to chloride concentrations would effectively remove this discrepancy; the data presented below are not normalized in this manner. The decreasing trend in Na/Cl downcore likely reflects a sodium sink in clays or zeolites.

Calcium, magnesium, and potassium concentrations continue trends seen in the overlying IW samples collected from Hole U1385G (Figure **F34**; Hodell et al., 2024a). Calcium increases with depth in Hole U1385K from a minimum of 9.0 mM at 419.6 m CSF-A (Section 401-U1385K-8X-2) to 13.6 mM at 550.2 m CSF-A (Section 22X-5). This calcium increase with depth in Hole U1385K coincides with a slight decrease in pH and likely reflects net carbonate dissolution (Figure **F30**). Magnesium shows a slight decrease from 33.1 mM at 419.6 m CSF-A to 27.5 mM at 550.2 m CSF-A. Potassium concentrations in Hole U1385K are relatively constant, ranging 6.2–7.0 mM. The

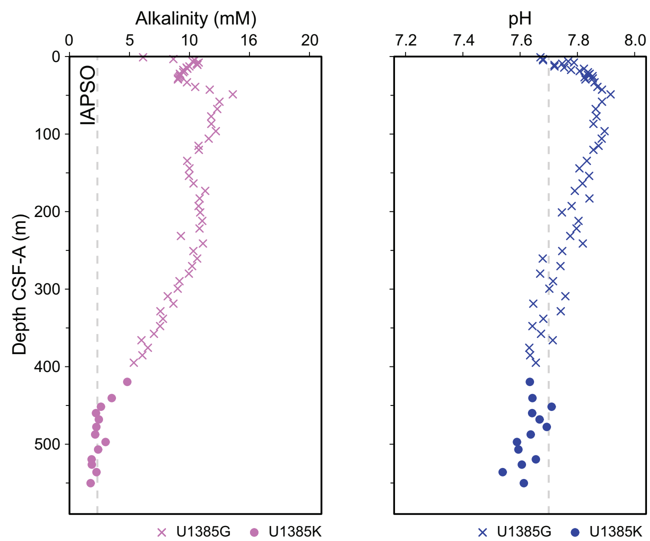

Figure F31. IW alkalinity and pH, Hole U1385K. Dashed line = IAPSO standard seawater. Results from Expedition 397 Hole U1385G are shown for comparison (Hodell et al., 2024a).

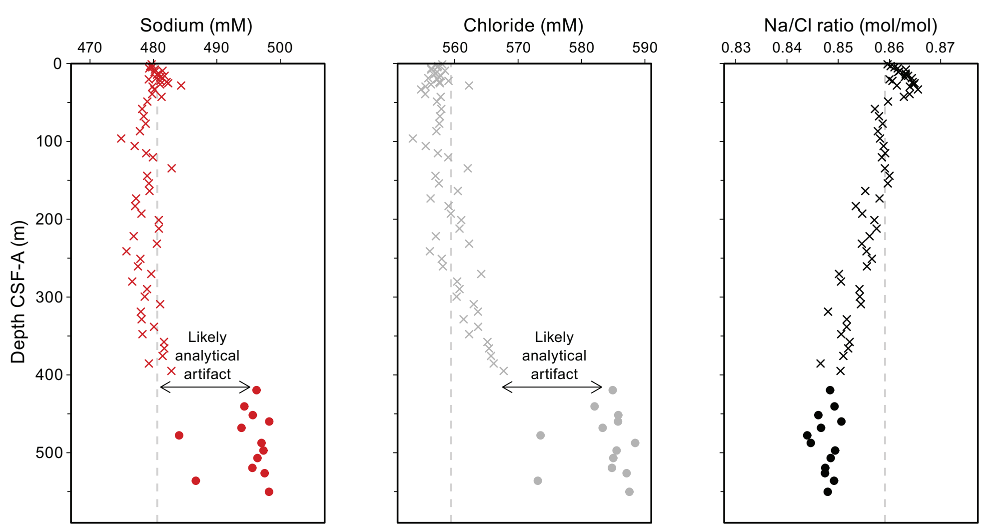

Figure F32. IW sodium and chloride concentrations, and Na/Cl ratios, Hole U1385K. Dashed line = IAPSO standard seawater. Results from Expedition 397 Hole U1385G are shown for comparison (Hodell et al., 2024a). Note apparent offsets between expedition data sets for sodium and chloride concentrations that are likely analytical artifacts.

variations in magnesium and potassium are likely caused by minor amounts of authigenic clay and dolomite formation.

Sulfate is consistently less than 1.0 mM from the uppermost sample to 477.7 m CSF-A (Section 401-U1385K-14X-2) and then increases slightly to 2.6 mM at 536.0 m CSF-A (Section 20X-2) (Figure **F33**). Low sulfate concentrations indicate that the cored interval is deeper than the SMTZ at ~50 m CSF-A (Expedition 339 Scientists, 2013; Hodell et al., 2024a). Bromide shows a constant value of 1.0 mM in Hole U1385K, approximately 0.04 mM higher value than at the bottom of Hole U1385G (Hodell et al., 2024a). The offset between Br concentrations in Holes U1385G and U1385K likely stems from the same procedural or analytical errors reflected in Na and Cl concentrations. The increase in Br concentrations in the shallow part of the profile stems from the degradation of organic matter; otherwise this ion behaves conservatively.

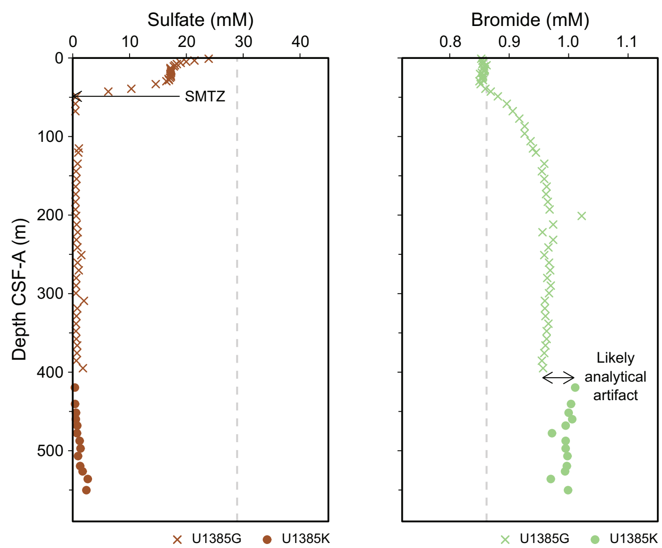

Figure F33. IW major anion concentrations (sulfate and bromide), Hole U1385K. Dashed line = IAPSO standard seawater. Results from Expedition 397 Hole U1385G are shown for comparison (Hodell et al., 2024a). Note apparent offset between expedition data sets for bromide concentrations that is likely an analytical artifact.

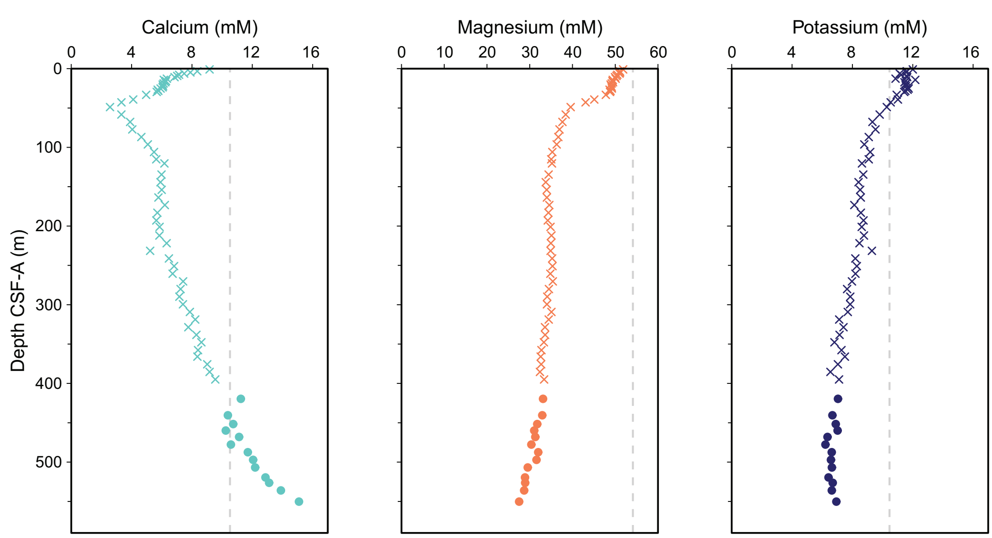

Figure F34. IW major cation concentrations (calcium, magnesium, and potassium), Hole U1385K. Dashed line = IAPSO standard seawater. Results from Expedition 397 Hole U1385G are shown for comparison (Hodell et al., 2024a).

6.2.3. Ammonium and phosphate

Ammonium and phosphate concentrations in IW were analyzed by spectrophotometry (Figure **F35**; Table **T16**). Ammonium concentrations decrease downcore from a maximum of 2527 μM at 419.6 m CSF-A (Section 401-U1385K-8X-2) to a minimum of 1808 μM at 550.2 m CSF-A (Section 21X-5). Phosphate concentrations show minor variation between 3.60 and 4.12 μM in Hole U1385K. Ammonium shows good continuity with the data from Hole U1385G (Hodell et al., 2024a), with the continuous decrease in ammonium with depth likely reflecting downward diffusion below the zone of methanogenesis. Phosphate concentrations show an apparent discontinuity between 8.2 μM at 394 m CSF-A (Section 397-U1385G-42X-5; Hodell et al., 2024a) and approximately 4.0 μM below 419.6 m CSF-A (Section 401-U1385K-8X-2). This discontinuity between the analyses conducted during different expeditions is likely an artifact of data standardization and analytical methods, although the greater magnitude of the difference in phosphate concentrations (Hole U1385K concentrations are <50% of the values at the bottom of Hole U1385G) indicates a different source of the offset than for the much smaller effect observed in Na, Cl, and Br concentrations. Internal data consistency was confirmed for both data sets, and data for Hole U1385K were rerun and verified to be robust. It is possible that the conditions or timing of IW sampling resulted in differential mobilization of P-bearing phases during the two expeditions, as the good agreement between the amount of organic C in the two holes suggests that sudden changes in the availability or degradation of organic matter that could affect IW phosphate concentrations are unlikely.

6.2.4. Trace elements (Li, Si, Ba, B, Sr, Fe, and Mn)

Trace element concentrations in IW were analyzed by inductively coupled plasma–atomic emission spectroscopy (ICP-AES) (Table **T17**). All trace elements exhibit continuous trends from the overlying samples collected from Hole U1385G (Figures **F36**, **F37**, **F38**; Hodell et al., 2024a). Small (~5%) offsets may be present given the behavior of the conservative elements, but the scale of changes of these chemically reactive elements, as well as the general scatter in many of the profiles, obscures these smaller analytical artifacts. Lithium increases from 84 μM at 419.6 m CSF-A (Section 401-U1385K-8X-2) to 262 μM at 550.2 m CSF-A (Section 21X-5) (Figure **F36**), likely reflecting clay mineral diagenesis. Silicon decreases from 211 μM at 419.6 m CSF-A to <150 μM below 450 m CSF-A, and the similarity to the depth profile for alkalinity (Figure **F36**) suggests that authigenic silicate formation is occurring at depth at this location.

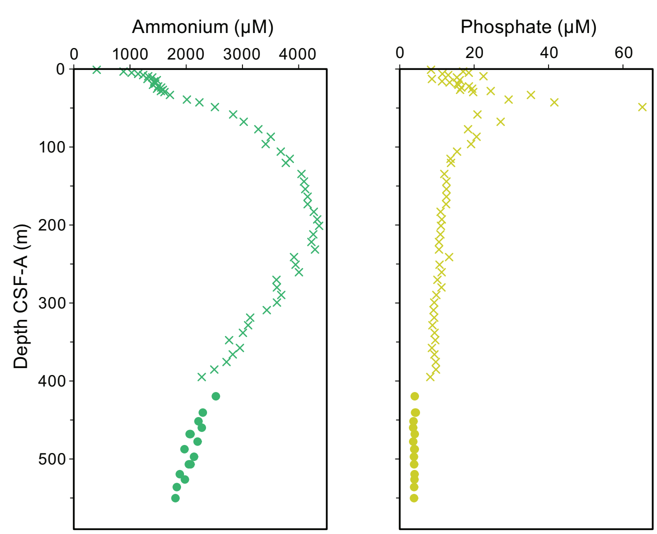

Figure F35. IW major nutrient concentrations (ammonium and phosphate), Hole U1385K. Results from Expedition 397 Hole U1385G are shown for comparison (Hodell et al., 2024a). Note offset between expedition data sets for phosphate concentrations that may be an artifact of sample preparation; Expedition 401 results were replicated to confirm calibration and data reported from Hole U1385K.

Barium concentrations decrease from a maximum of 80 µM at 419.6 m CSF-A to a minimum of 8 µM at 535.9 m CSF-A in Hole U1385K (Figure **F37**). Combined with barium data from Hole U1385G (Hodell et al., 2024a), barium shows a clear response at the SMTZ and continues to respond to sulfate concentrations through the mechanism of barite ($BaSO_4$) solubility. Boron shows a gradual decrease from 492 µM at 419.6 m CSF-A to 322 µM at 550.2 m CSF-A with some fluctuations, matching the trend of silicon and likely reflecting a decrease in clay dissolution. Strontium shows an increase from 581 µM at 419.6 m CSF-A to 1460 µM at 550.2 m CSF-A, which accompanies the increase in calcium and indicates calcium carbonate dissolution and/or recrystallization.

Iron concentrations in Hole U1385K were below the detection limit of the ICP-AES methods, whereas manganese ranges 0.8–1.6 µM. Higher concentrations of Fe were recorded in Hole U1385G (10.9 µM at 394.9 m CSF-A; Hodell et al., 2024a), but the apparent difference in Fe concentrations may be related to the same analytical artifact tentatively identified in phosphorus con-

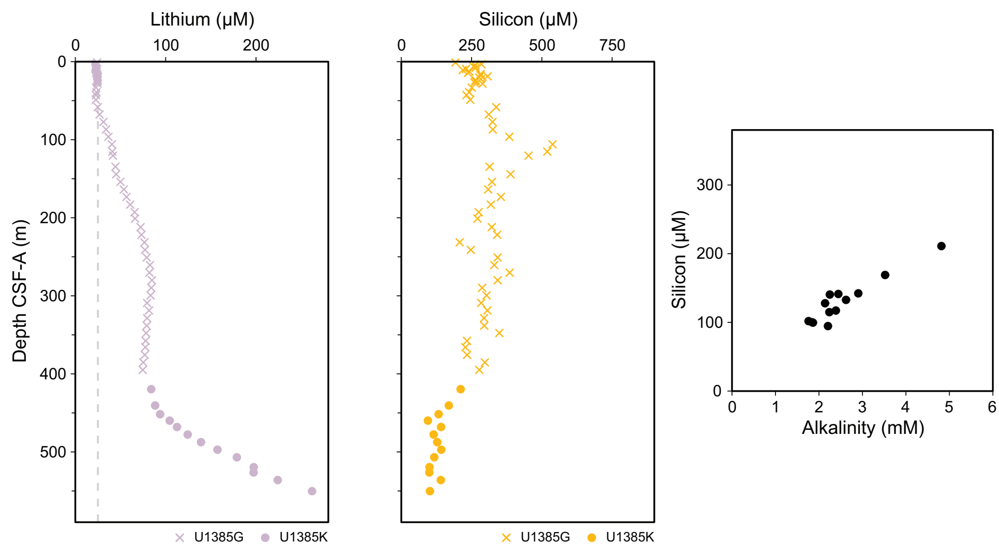

Figure F36. IW minor element concentrations (Li and Si) and crossplot of alkalinity versus silicon concentration, Hole U1385K. Dashed line = IAPSO standard seawater. Results from Expedition 397 Hole U1385G are shown for comparison (Hodell et al., 2024a).

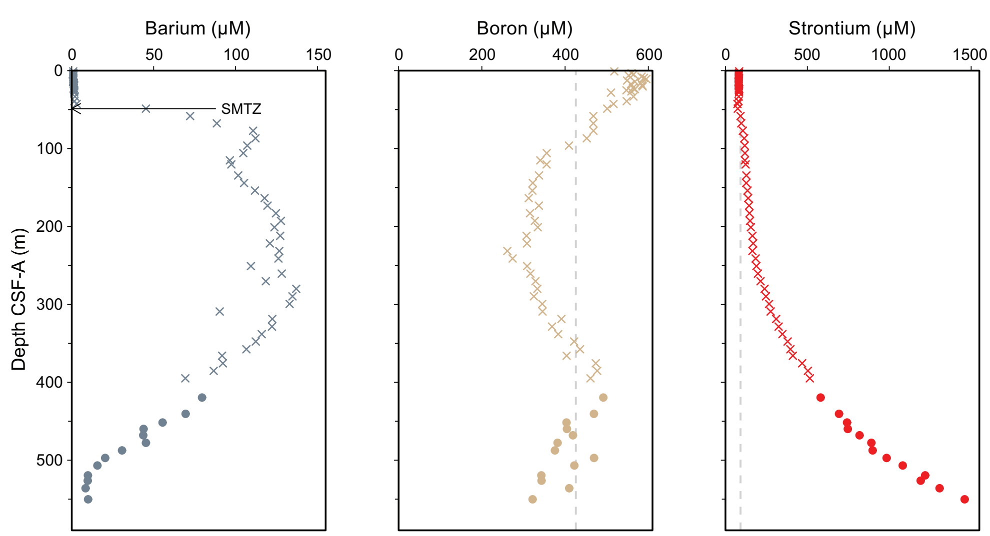

Figure F37. IW minor and trace element concentrations (Ba, B, and Sr), Hole U1385K. Dashed line = IAPSO standard seawater. Results from Expedition 397 Hole U1385G are shown for comparison (Hodell et al., 2024a).

centrations. A precipitous change in redox conditions is highly unlikely, but it is possible that Fe-phosphorus phases were mobilized in different ways during sampling for the two expeditions.

6.3. Sedimentary geochemistry

Sediment samples were collected for analysis of solid-phase geochemistry at a resolution of one sample per recovered core in Hole U1385K (Table **T18**). These samples came from a fraction of the IW squeeze cake residue (n = 13 samples). Some additional samples were taken from both Holes U1385K (n = 6 samples) and U1385L (n = 3 samples) to identify the geochemical variation across lithologic color cycles identified by the shipboard sedimentologists.

6.3.1. Calcium carbonate

Weight percent $CaCO_3$ varies from 38.6 to 68.9 wt% (Figure **F39**; Table **T18**) with a mean of 52.4 wt% and a standard deviation of 8.5 wt%. $CaCO_3$ continues the same amplitude of variability seen in shallower sediments collected in Hole U1385G during Expedition 397 (Hodell et al., 2024a), suggesting that the same range of production and mixing may be occurring and that the variability is likely cyclic in nature. The highest carbonate concentrations presumably reflect higher carbonate productivity and/or lower dilution or dissolution. The range in the $CaCO_3$ measurements represents random sampling of the higher frequency lithologic cycles, detected visually in color variations (see **Lithostratigraphy**) and in measurements of physical properties of the cores (see **Physical properties**).

The determination of carbonate by coulometry and XRD analysis agrees very well (Figure **F40**). A negative correlation (R^2 = 0.58) between the $CaCO_3$ weight percent and adjacent NGR measurements shows that the cycles in NGR are controlled by the balance of carbonate and clay deposition at this site (NGR itself is controlled principally by the concentration of clay minerals) (Figure **F41**). A weaker negative correlation (R^2 = 0.33) between the $CaCO_3$ weight percent and adjacent MS measurements suggests that the carbonate sedimentary fraction also dilutes the magnetic mineral fraction in the sediments, though, being a minor sediment component, the relationship is not as clear as for that with NGR (Figure **F41**; **Physical properties**). The $CaCO_3$ range and cyclicity is aliased by the low resolution and random shipboard sampling across the lithologic cyclicity (similar to previous sites; e.g., Figure **F41**) and could be refined with higher resolution analyses. In XCB cores, whole-round IW sampling was selected from core sections with more intact lithology,

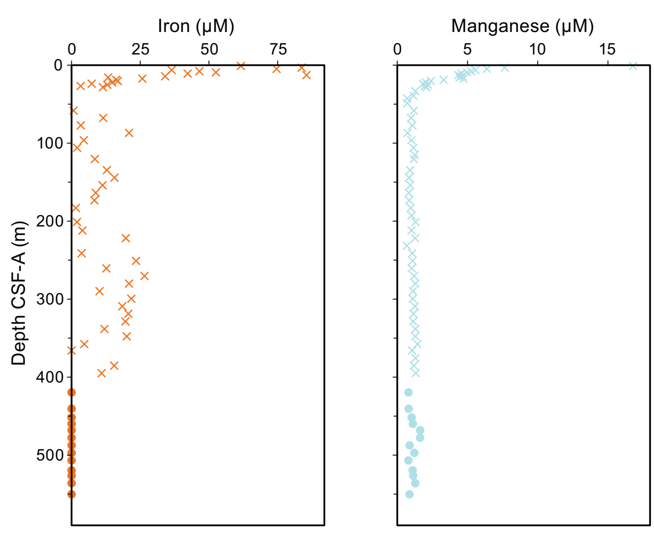

Figure F38. IW trace element concentrations (Fe and Mn), Hole U1385K. Fe and Mn concentrations below detection limit are plotted as 0 μM. Results from Expedition 397 Hole U1385G are shown for comparison (Hodell et al., 2024a). Note apparent offset between expeditions that may be an artifact of sample preparation.

Table T18. $CaCO_3$, organic carbon, and nitrogen in sediments, Hole U1385K. **Download table in CSV format.**

avoiding sediments visibly disturbed by drilling rather than sampling specific lithologies to evaluate their carbonate content. Consequently, some bias may be incorporated into the reported $CaCO_3$ weight percent because part of the natural range may be unsampled.

6.3.2. Carbon and nitrogen

Total organic carbon (TOC) is calculated to be 0.18–0.97 wt% (Figure **F39**; Table **T18**) based on the difference between total carbon (TC) and total inorganic carbon (TIC) (TOC = TC − TIC). Weight percent nitrogen (Figure **F39**; Table **T18**) was measured downhole and ranges 0.008–0.048 wt%. The C/N mass ratio (using TOC and total nitrogen [TN]) is used to distinguish the origin of organic matter (marine versus terrestrial) in sediment (Emerson and Hedges, 1988; Meyers, 1997) and may also be influenced (decreased) by the degradation of organic matter (Ruttenberg and Goñi, 1997). The C/N data set ranges 4.8–62.6, with a mean C/N ratio of 13.7 and a standard deviation of 12.6, indicating that the organic carbon is dominantly of marine origin with sporadic input

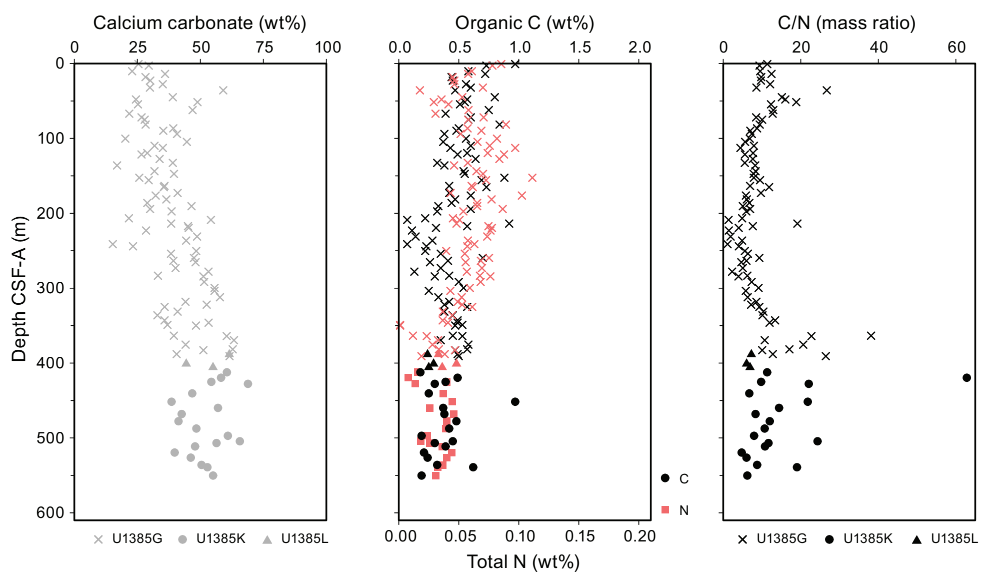

Figure F39. $CaCO_3$, organic carbon, nitrogen, and C/N in sediments, Holes U1385K and U1385L. Results from Expedition 397 Hole U1385G are shown for comparison (Hodell et al., 2024a).

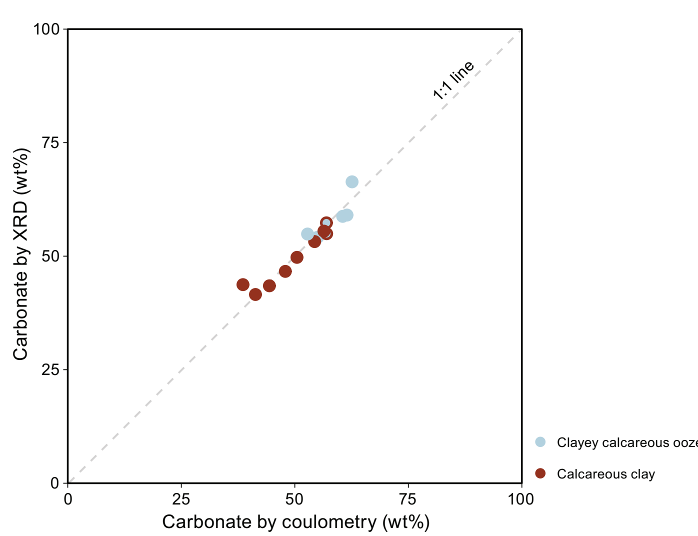

Figure F40. Relationship between carbonate weight percent determined by analysis of XRD spectra and coulometry, Holes U1385K and U1385L. Symbol color indicates lithologies found immediately above and below each IW whole-round sample; where they differ, interior color shows lithology above and exterior color shows lithology below.

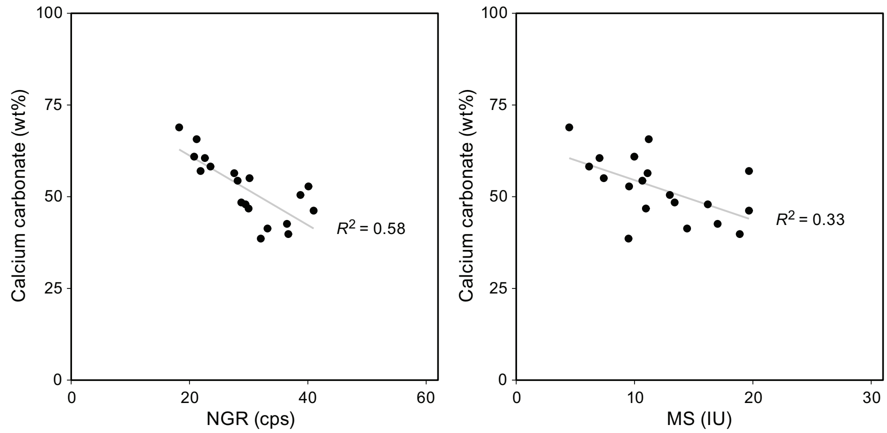

Figure F41. Relationship between carbonate weight percent, NGR, and MS, Hole U1385K. NGR and MS measurements represent closest analysis to carbonate sample (usually within 15 cm). cps = counts per second, IU = instrument units.

of terrestrial organic matter (Figure **F39**; Table **T18**). There is no significant downhole trend in the data, suggesting that marine production and terrestrial inputs as well as organic degradation are broadly consistent across the drilled interval, with variability likely cyclic at frequencies higher than that sampled here. Variability in the C/N ratio may be related to terrestrial inputs or marine productivity changes in discrete samples. However, some component of the variability is likely analytical scatter due to the analytical challenge of obtaining TOC from TC minus TIC, and one outlier with high C/N ratio is associated with a very low measured TN concentration of 0.008 wt%.

7. Physical properties

Physical properties at Site U1385 were determined in Holes U1385K and U1385L at 2.5 cm spacing on the Whole-Round Multisensor Logger (WRMSL) and the Section Half Multisensor Logger (SHMSL) and at 10 cm spacing on the Natural Gamma Radiation Logger (NGRL) (see **Physical properties** in the Expedition 401 methods chapter [Flecker et al., 2025a]). Additionally, all cores from Hole U1385L were scanned on the Special Task Multisensor Logger (STMSL) to stratigraphically correlate them to the physical properties data from Expedition 397 and to Hole U1385K. *P*-wave velocity measurements of the split core section (working half) were determined at two locations in each core section. One or two discrete cylindrical samples were taken from each core for moisture and density (MAD) measurements.

The physical properties data show pervasive cyclicity throughout Holes U1385K and U1385L (Figure **F42**). Regularly spaced high-amplitude cycles characterize the central zone (from ~330 to ~500 m CSF-A) of the recovered interval, with more variable amplitude in the cycles above and below that zone. A prominent rise in MS and a decline in lightness (L*) (Figure **F43**) at 458 m CSF-B, corresponds to the Lithostratigraphic Unit II/III boundary (see **Lithostratigraphy**). This boundary is also conspicuous as a two orders of magnitude downhole increase in magnetic intensity (see **Paleomagnetism**; Figure **F24**).

7.1. Magnetic susceptibility

Three large-scale trends define the MS data set (Figure **F42**). The interval from 380 to 458 m CSF-B exhibits ~1 m wavelength cycles with no variation in baseline level with depth. The amplitude abruptly increases at around 417 m CSF-B. From 458 to 520 m CSF-B, Lithostratigraphic Unit II is characterized by a shift to higher MS values that subsequently decline downcore. MS values increase abruptly at ~520 m CSF-B and decline downcore to 535 m CSF-B, where they return to lower values with lower amplitude variability.

The high MS values correspond to calcareous clays, and low values correspond to clayey calcareous oozes (Figure **F9A, F9B, F9D**).

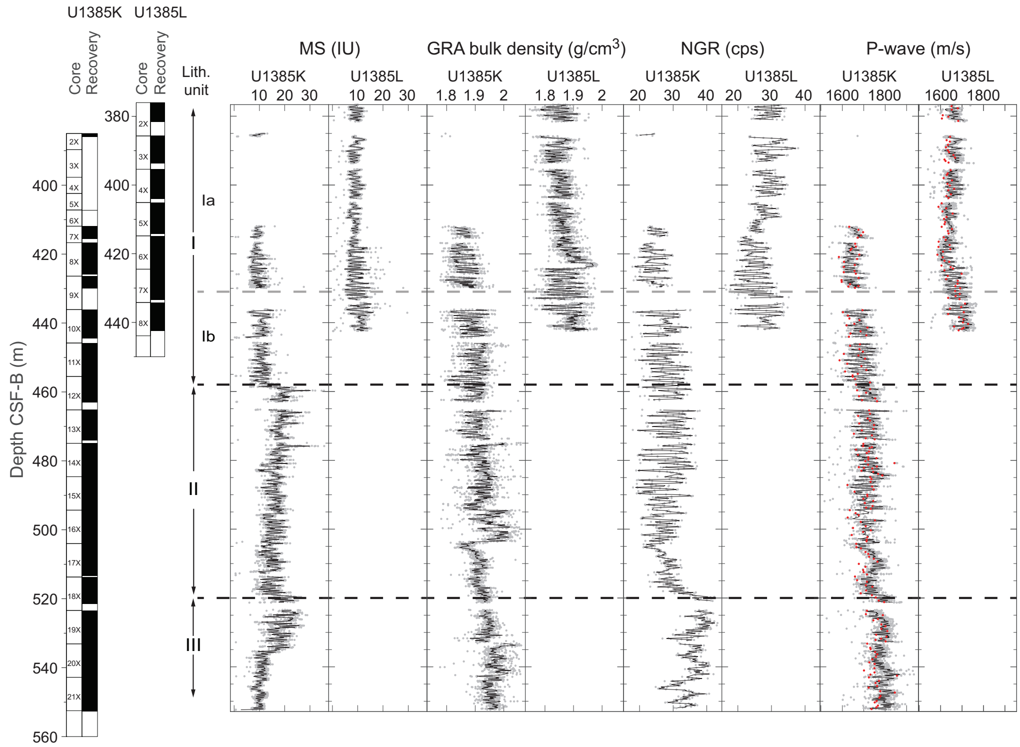

Figure F42. Section Half Multisensor Logger MS and WRMSL GRA density, NGR, and *P*-wave velocity, Holes U1385K and U1385L. Gray dots = original data sets (with anomalous values removed from GRA density and PWL), overlying black lines = 15 point locally weighted nonparametric regression (LOWESS) smooth run on MS, GRA density, and PWL to highlight variations and secular trends and 5 point LOWESS smooth run on NGR because data set was smaller. Red dots = PWC measurements. IU = instrument units, cps = counts per second.

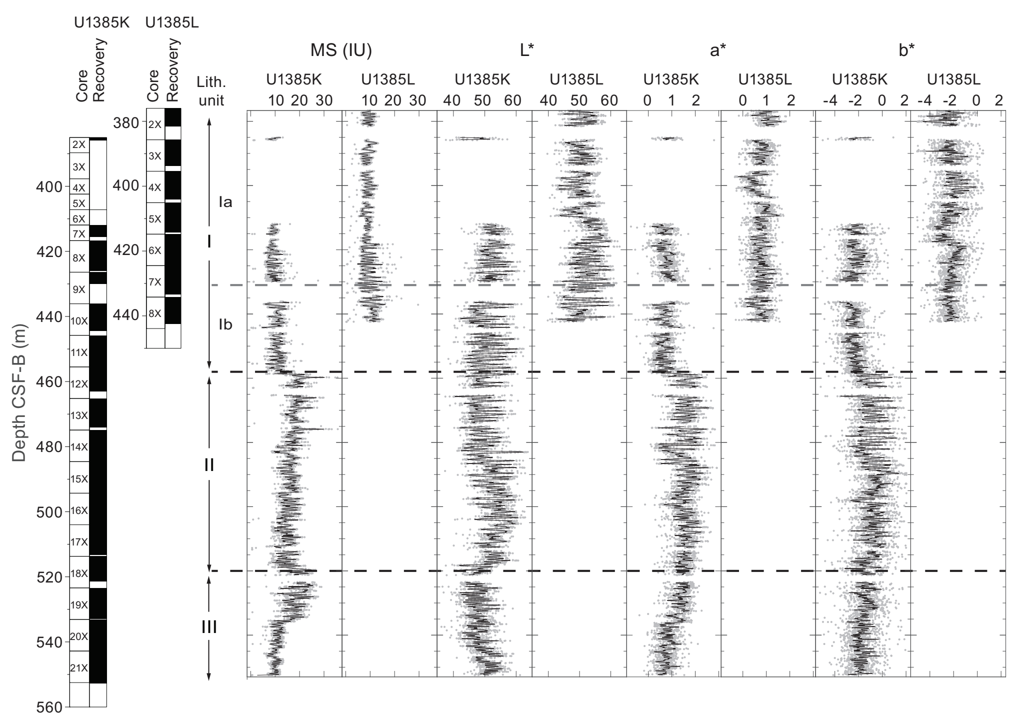

Figure F43. MS and L*, a*, and b* color variation, Holes U1385K and U1385L. Gray dots = original data sets (with anomalous values removed from L*, a*, and b*), overlying black lines = 15 point locally weighted nonparametric regression (LOWESS) smooth run on all data sets to highlight variations and secular trends. Gray dashed line = lithostratigraphic subunit boundary, black dashed lines = lithostratigraphic unit boundaries. IU = instrument units.

The Unit I/II boundary (458 m CSF-B) coincides with both a sharp rise in MS values and the onset of a brief interval (458–482 m CSF-B) of inverse phase relationship between the MS and NGR cycles, where high MS values correspond to low NGR values and vice versa (Figure **F44**). Below and above this interval, the MS NGR values appear to be in phase, with high and low MS values associated with calcareous clays and clayey calcareous oozes, respectively (Figure **F9D**). The out-of-phase interval of higher MS values is in the upper part of Unit II, which includes brown calcareous clays (Figure **F6**), and the peaks in MS, L*, a*, and b* (Figure **F43**) correlate with thin light brownish (10YR 6/1) layers.

The higher MS values between 458 and 530 m CSF-B coincide with a prominent interval of high magnetic intensity (Figure **F24**) that extends below the Unit II/III boundary. Postexpedition sampling and analysis is required to determine the precise change in magnetic mineralogy.

7.2. Gamma ray attenuation bulk density

Gamma ray attenuation (GRA) density values vary from ~1.77 to 2.01 g/cm³ for Holes U1385K and U1385L. As at the other sites of the expedition, GRA density is affected by core diameter: cores with smaller diameter give low bulk density estimates compared with cores that fill the core liner. MAD bulk density values are more reliable (Figure **F45**). Cores 401-U1385K-16X and 20X have higher GRA density values than cores immediately above and below, suggesting that core quality is also a factor affecting GRA density values.

The GRA density record consists of thin cyclic variation (~0.5–2 m cycles) superimposed on longer changes and trends in amplitude (Figure **F42**). Unit I (376–431 m CSF-B), consists of low-amplitude ~1 m thick cycles, with a subtle increase in density values with depth. Unit II is differentiated from Unit I by a downhole reduction in cycle amplitude and a higher baseline value. GRA values generally increase with depth in this unit, probably reflecting a typical sediment compaction trend.

The prominent MS peak at the Unit II/III boundary is absent in the GRA density record (Figure **F42**). The compaction trend of increasing bulk density continues in Unit III.

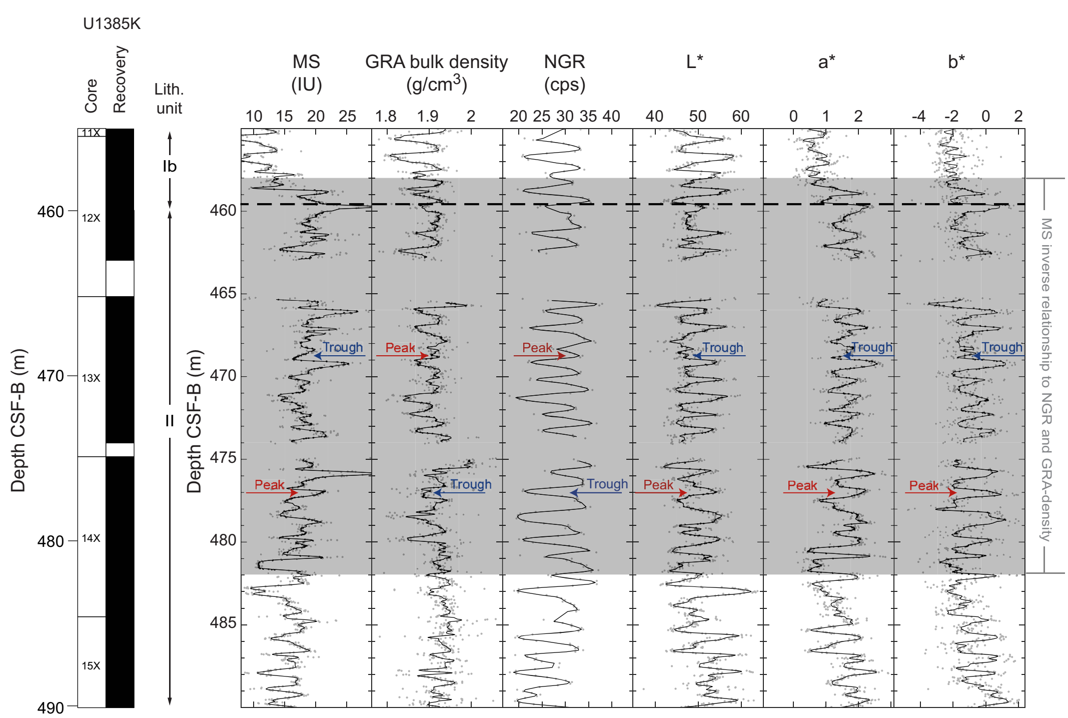

Figure F44. MS; GRA density; NGR; and L*, a*, and b* color variation from ~455 to ~490 m CSF-B, Hole U1385K. Note how MS peak (red arrows) corresponds to NGR trough (blue arrows), and vice versa (466.5 and ~476 m CSF-B). Dashed line = Lithostratigraphic Unit I/II boundary. IU = instrument units, cps = counts per second.

7.3. Natural gamma radiation

NGR fluctuates between 15 and 45 counts/s in Holes U1385K and U1385L (Figure **F46**). The record can be divided into three intervals (Figure **F42**): an upper interval (380–417 m CSF-B) characterized by cycles of varying amplitude and thickness centered around 30 counts/s; a central interval (417–504 m CSF-B) dominated by regular high-amplitude cycles; and a lowermost interval (504 m CSF-B to the bottom of Hole U1385K), where thinner (~1 m or <1 m at the bottom part of the NGR record) low-amplitude cycles are superimposed on lower frequency (~10 m) variations.

The three components of NGR, potassium, uranium, and thorium, were derived from the total NGR counts using the MATLAB code developed by De Vleeschouwer et al. (2017). The spectral NGR signal shows similar long-term variations to total NGR counts (Figure **F46**).

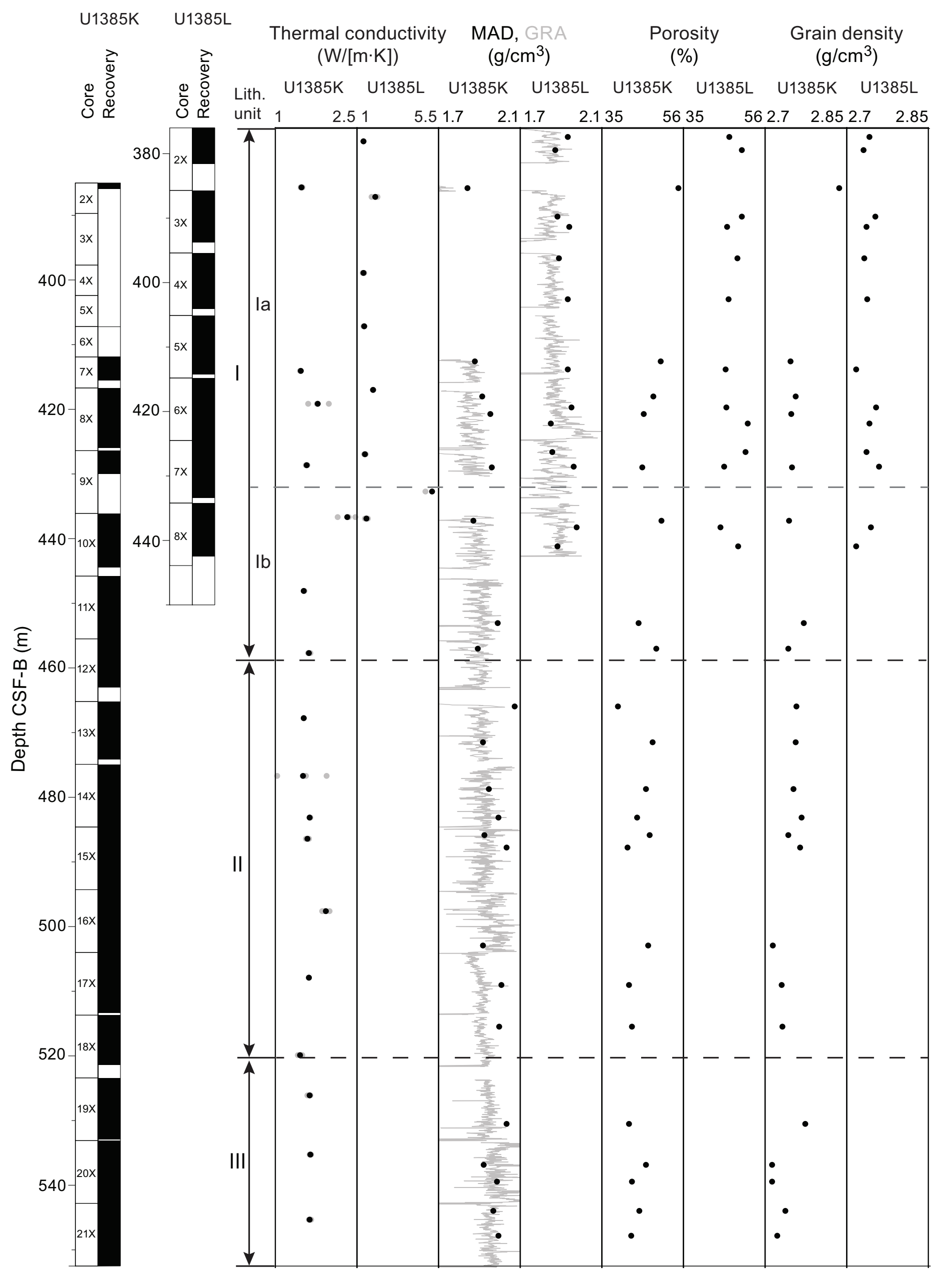

Figure F45. Thermal conductivity, MAD, GRA bulk density, porosity, and grain density, Holes U1385K and U1385L. Porosity and grain density were obtained from MAD measurements.

7.4. Spectrophotometry

Lightness (L*), green–red (a*), and blue–yellow (b*) color is highly cyclic, consisting of regular cycles with thicknesses ranging ~0.5–1.5 m. The L* record shows the same high-amplitude cyclic pattern as the NGR (Figures **F42**, **F43**), whereas a* and b* data show a similar abrupt rise in values at 458 m CSF-B, coinciding with the lithologic color change at the Unit I/II boundary. Only in the upper part of Unit II (458–490 m CSF-B) do the a* and b* records show regular high-amplitude cyclicity. This corresponds to an interval of very well developed color-specific lithologic alternations with relatively sharply defined boundaries (see **Lithostratigraphy**). Elsewhere, the variability is smaller scale and more irregular, possibly reflecting the gradational nature of many of the lithologic contacts.

7.5. Thermal conductivity

At Site U1385, thermal conductivity was measured in triplicate at one position per core, typically on Section 2 of each core, using a half-space probe (H51033). When Section 2 was cracked or deformed, the measurement was made on another section. The average value for thermal conductivity is slightly higher in Hole U1385L (1.93 W/[m·K]) compared to Hole U1385K (1.61 W/[m·K]) (Figure **F45**), with minimum and maximum values ranging 1.03–2.48 and 1.36–2.19 W/(m·K) for Holes U1385K and U1385L, respectively, except for one anomalous value that yielded a thermal conductivity of 5.53 W/(m·K) at ~435 m CSF-B. Holes U1385K and U1385L show a slowly increasing trend of thermal conductivity values with depth. This trend matches with and continues the thermal conductivity measurements of previously drilled splices at this site during Expedition 339 (Hole U1385A) and Expedition 397 (Holes U1385F and U1385G) (Expedition 339 Scientists, 2013; Hodell et al., 2024a). Thus, when comparing these holes, it is evident that deeper and older sedi-

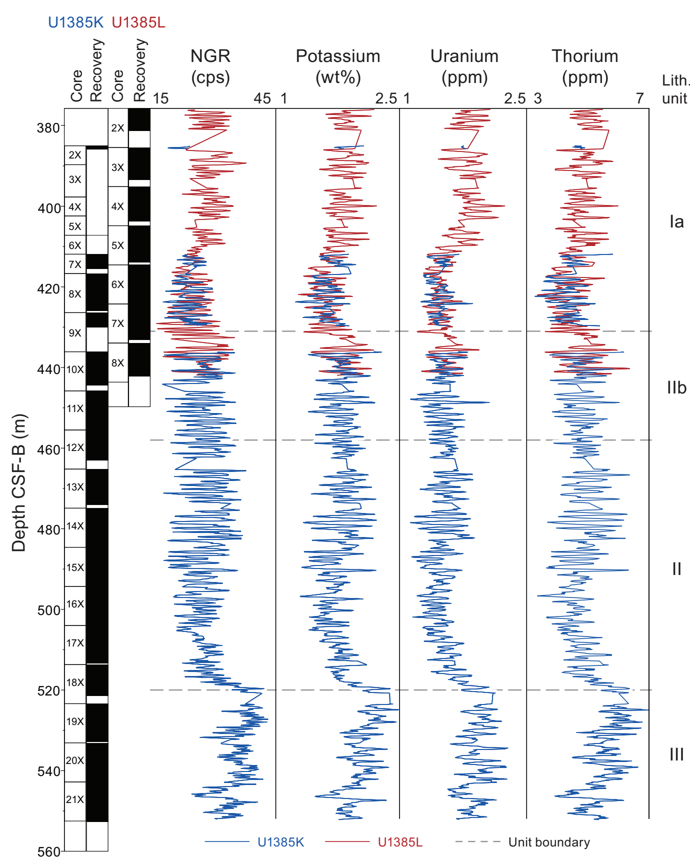

Figure F46. NGR measurements, Holes U1385K and U1385L. Corresponding spectral NGR components (potassium, uranium, and thorium) extracted from total NGR counts using shipboard codes based on method described by De Vleeschouwer et al. (2017). cps = counts per second.

ments have higher thermal conductivity values. Thermal conductivity slowly increases downhole in Holes U1385K and U1385L, except for two outliers present in Subunit IIb: 2.49 W/(m·K) at 436 m CSF-B in Hole U1385K and 5.53 W/(m·K) at ~433 m CSF-B in Hole U1385L (Figure **F45**), which are anomalous based on thermal conductivity of similar sediments. Unit III shows a top-down increasing trend with some value dispersion in Core 401-U1385K-14X at ~480 m CSF-B.

MAD bulk density slowly increases through Units I–III in Hole U1385K. The general trend for Site U1385 is that thermal conductivity smoothly increases downhole, followed by a similar increase in GRA and MAD bulk densities. Porosity decreases downhole because of compaction, which also explains the depth-increasing density trend. Grain density shows a scattered pattern within a narrow range, with no obvious trend.

7.6. *P*-wave velocity

P-wave velocities were measured with the WRMSL (*P*-wave logger [PWL]) for Holes U1385K and U1385L (Figures **F42**, **F47**). Unlike the highly scattered values from Sites U1609 and U1610, the PWL of the WRMSL at Site U1385 yielded apparently reliable *P*-wave velocity values, probably because of minimal gaps between the sediments and the core liners.

Excluding a few outliers, PWL values range 1550–1900 m/s for Holes U1385K and U1385L. Values generally increase with depth and show notable and very similar cyclicity to the MS, NGR, and

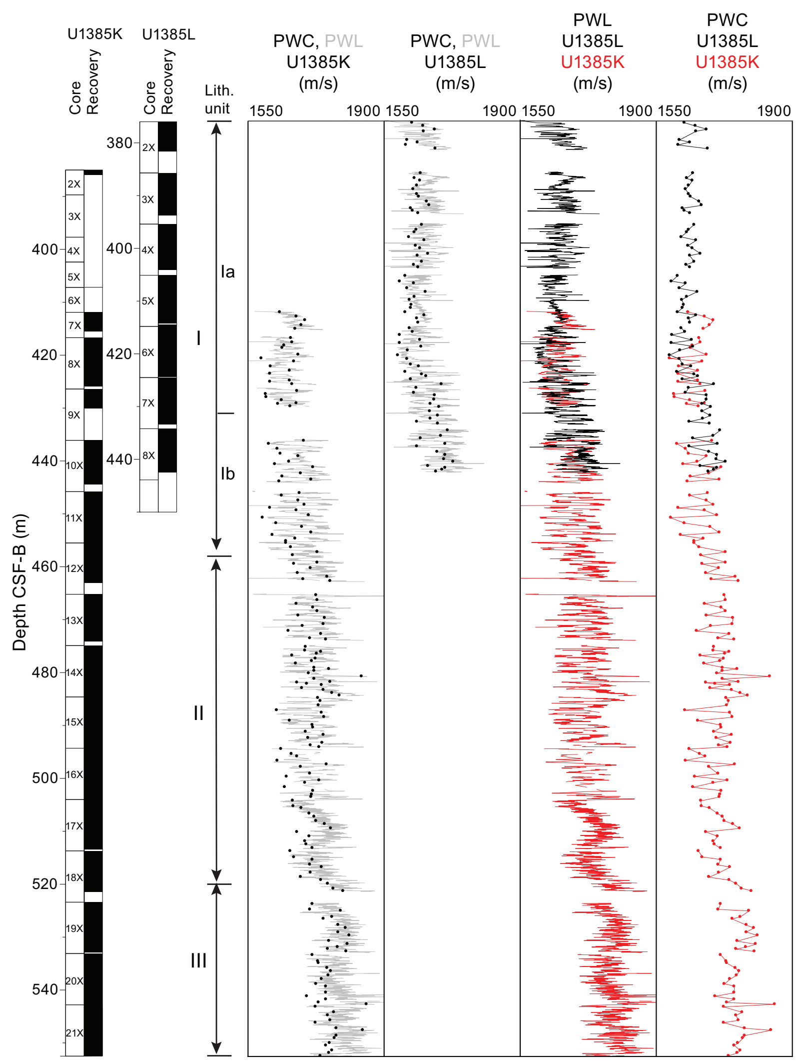

Figure F47. PWL (WRMSL) and PWC, Holes U1385K and U1385L. Comparisons of PWL and PWC results between holes are also shown.

GRA density data sets. Similar to NGR and MS, the amplitude of PWL cycles is lower in Subunit Ia compared to Subunit Ib. The cycles in Unit II are 1.1–1.5 m thick, and they shift toward thinner cycles in Unit III (0.5–1.1 m thick).

A separate set of discrete *P*-wave velocities (*P*-wave caliper [PWC]) were measured on working halves. As shown in Figure **F47**, PWC and PWL velocities increase with depth. For Hole U1385K, the lowest value (~1584 m/s) is at ~420.9 m CSF-B and the highest value (1855 m/s) is at 542.6 m CSF-B. For Hole U1385L, the lowest value (~1585 m/s) is at ~420.26 m CSF-B and the highest value (1728 m/s) is at 440.36 m CSF-B. Generally, PWC velocities show similar absolute values to PWL velocities. Both sets of velocity measurements likely underestimate the in situ V_P velocities, but because there was no downhole logging at this site (Rider, 1985), the extent of this underestimation is not determined.

7.7. Moisture and density measurements

A total of 35 discrete cylindrical samples were taken from the working halves of each core for Holes U1385K and U1385L for bulk density measurements. As shown in Figure **F45**, MAD bulk density values are generally higher than GRA values in intervals where the XCB system was employed for coring. However, because discrete samples are free from the negative influence of sediment-liner gaps, MAD bulk density measurements are considered more reliable than GRA densities.

8. Bulk density, grain density, and porosity

Bulk density calculated from MAD measurements typically varies between 1.84 and 2.08 g/cm³ for Hole U1385K and between 1.85 and 1.98 g/cm³ for the short upper interval recovered in Hole U1385L (Figure **F45**). Grain density typically ranges 2.71–2.83 g/cm³ for Hole U1385K and 2.72–2.76 g/cm³ for Hole U1385L (Figure **F45**). Generally, both grain density and porosity decrease with depth (Figures **F45**, **F48**, **F49**).

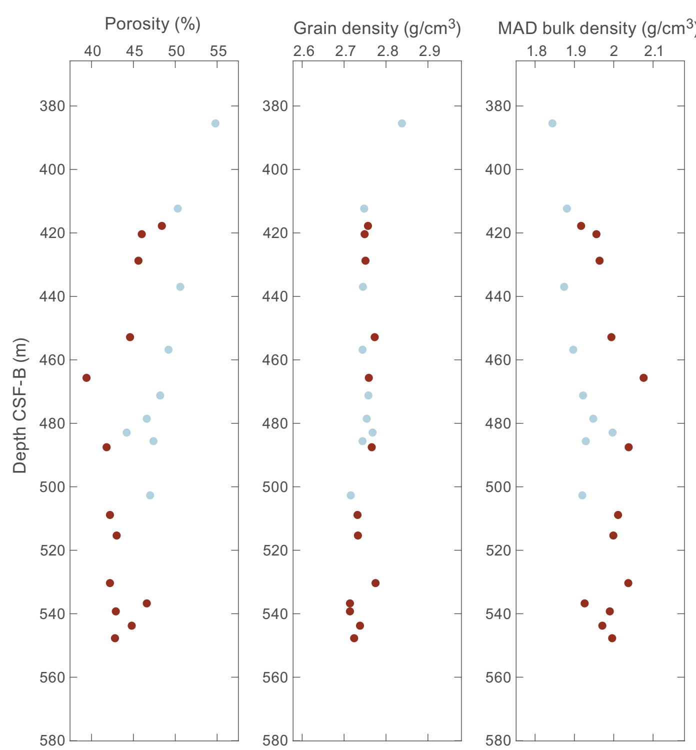

Figure F48. Porosity, grain density, and bulk density with lithologies based on MAD, Hole U1385K. Note that recovered lithologies are clayey calcareous ooze and calcareous clay.

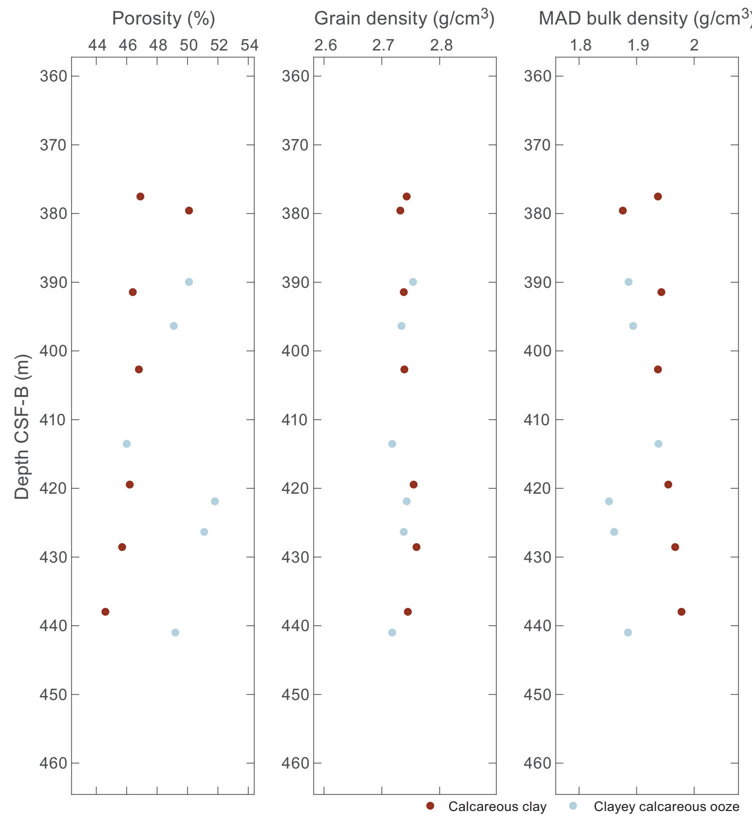

Figure F49. Porosity, grain density, and bulk density with lithologies based on MAD, Hole U1385L. Note that recovered lithologies are clayey calcareous ooze and calcareous clay.

Discrete porosity values range 39.4%–54.8% in Hole U1385K and 44.6%–51.8% in Hole U1385L (Figure **F45**). The lowest porosity (39.4%) and highest bulk density value (2.08 g/cm³) measured at ~385 m CSF-B in Hole U1385K correspond to a calcareous mud sample, potentially indicating that in the lithologic cycles, calcareous mud layers have higher bulk density than the calcareous ooze layers (see **Lithostratigraphy**).

9. Stratigraphic correlation and age model

Expedition 401 Holes U1385K and U1385L include cyclic variations in physical properties data that can clearly be correlated from hole to hole (Figure **F50**) within sediments that date from the Tortonian to the Early Pliocene (see **Biostratigraphy**). Stratigraphic correlation was first made from Hole U1385L to the short overlapping depth interval cored during Expedition 397 (Holes U1385F–U1385H and U1385J) to make a consistent composite depth scale for these holes. Holes U1385K and U1385L overlap by approximately 30 m (Cores 401-U1385K-7X through 10X correspond to Cores 401-U1385L-5X through 8X), allowing for stratigraphic correlation (Table **T19**) and the construction of a splice record for Site U1385 (Table **T20**; Figure **F50**). However, because most of the Miocene stratigraphy at Site U1385 is recovered in a single hole (either Hole U1385K or U1385L but not both), there are inevitable gaps in stratigraphy that complicate the alignment of the two holes. To gauge how much stratigraphy is missing in each of the core gaps, after the expedition we made a visual correlation between Expedition 401 Site U1385 and Expedition 397 Site U1587 (not shown; Hodell et al., 2024b), which has a complete stratigraphic record and similar stratigraphic patterns despite being at a deeper water depth. Based on this correlation, we adjusted the thickness of the core gaps in Holes U1385K and U1385L in the composite depth scale to reflect the thickness of missing stratigraphy. The affine and splice tables presented here were finalized in May 2024 (Tables **T19**, **T20**) and will be revised further to adjust the spacing between cores based on cyclostratigraphic interpretation.

The age model is composed of nannofossil (n = 9), foraminifer (n = 7), and paleomagnetic (n = 12) age control datums between 5.0 and 8.8 Ma (Tables **T14**, **T3**, **T4**). Gaps in age tie points are less of a concern at this site as cyclicity provides evidence for consistency of sedimentation rates, albeit complicated by gaps in recovery. There is a good correspondence between the bioevents and magnetostratigraphic chron boundaries at Site U1385 (Figure **F51**). These indicate that the sedimentation rate is fairly constant (~50 m/Ma) from just above the Miocene/Pliocene boundary (409 m CSF-B) to 510–520 m CSF-B. Below this there are some biostratigraphic indications that the sedimentation rate declines slightly to the bottom of the hole. This is supported by the cycle thickness measurements made on both the NGR and MS data, which show a shift to thinner beds at this level (Figure **F51**; Table **T21**). These lower sedimentation rates are consistent with a low sedimentation rate at Site U1609 in the Tortonian relative to the overlying sediments.

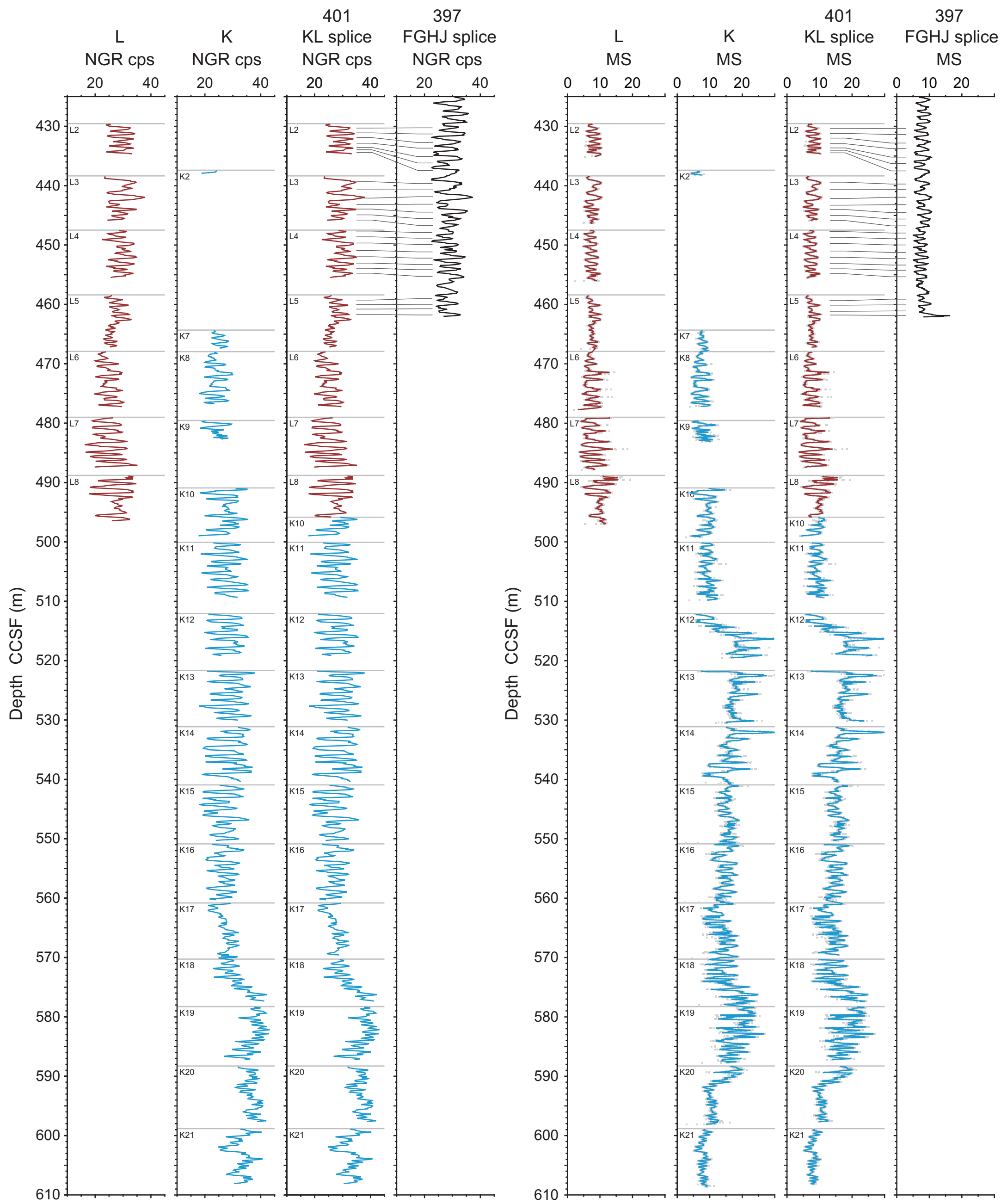

Figure F50. Stratigraphic correlation in NGR and MS, Holes U1385K and U1385L. Correlation to overlapping depth interval generated during Expedition 397 (Holes U1385F–U1385H and U1385J) is also shown. CCSF = core composite depth below seafloor.

Table T19. Affine table, Holes U1385K and U1385L. CCSF- A = core composite depth below seafloor. **Download table in CSV format.**

Core	Top depth CSF-A (m)	Top depth CCSF (m)	Cumulative offset (m)	Differential offset (m)	Growth rate	Shift type	Data used	Reference core	Reference tie point CSF-A (m)	Shift tie point CSF-A (m)
401-U1385K-										
2X	385	437.400	52.4	0	1.136	SET	Natural gamma			
7X	411.9	464.336	52.436	0	1.127	TIE	Susceptibility	L5	413.062	413.937
8X	416.7	467.962	51.262	0	1.123	TIE	Natural gamma	L6	419.626	421.475
9X	426.4	479.565	53.165	0	1.125	TIE	Natural gamma	L7	425.855	427.201
10X	436.1	490.921	54.821	0	1.126	TIE	Natural gamma	L8	441.029	440.819
11X	445.8	500.077	54.277	0	1.122	SET	Natural gamma			
12X	455.5	512.077	56.577	0	1.124	SET	Natural gamma			
13X	465.2	521.677	56.477	0	1.121	SET	Natural gamma			
14X	474.9	531.127	56.227	0	1.118	SET	Natural gamma			
15X	484.6	540.927	56.327	0	1.116	SET	Natural gamma			
16X	494.3	550.877	56.577	0	1.114	SET	Natural gamma			
17X	504	560.827	56.827	0	1.113	SET	Natural gamma			
18X	513.7	570.277	56.577	0	1.11	SET	Natural gamma			
19X	523.4	578.277	54.877	0	1.105	SET	Natural gamma			
20X	533.1	588.277	55.177	0	1.104	SET	Natural gamma			
21X	542.8	598.827	56.027	0	1.103	SET	Natural gamma			
401-U1385L-										
2X	376	429.563	53.563	0	1.142	TIE	Natural gamma	F30	373.809	377.71
3X	385.7	438.364	52.664	0	1.137	TIE	Natural gamma	J41	380.333	389.325
4X	395.4	447.489	52.089	0	1.132	TIE	Natural gamma	G42	390.264	399.971
5X	405.1	458.411	53.311	0	1.132	TIE	Natural gamma	J43	398.992	408.396
6X	414.8	467.911	53.111	0	1.128	SET	Natural gamma			
7X	424.5	479.011	54.511	0	1.128	SET	Natural gamma			
8X	434.2	488.811	54.611	0	1.126	SET	Natural gamma			

Table T20. Splice interval table, Holes U1385K and U1385L. CCSF- A = core composite depth below seafloor, Method A. **Download table in CSV format.**

Core	Top section	Top offset	Top depth CSF-A (m)	Top depth CCSF-A (m)	Bottom section	Bottom offset	Bottom depth CSF-A (m)	Bottom depth CCSF-A (m)	Splice type	Data used
401-U1385L-										
2X	1	0	376	429.563	4	81	381.19	434.753	APPEND	Natural gamma
3X	1	0	385.7	438.364	6	53	393.27	445.934	APPEND	Natural gamma
4X	1	0	395.4	447.489	6	66	403.56	455.649	APPEND	Natural gamma
5X	1	0	405.1	458.411	6	140	414	467.311	APPEND	Natural gamma
6X	1	0	414.8	467.911	7	54	424.25	477.361	APPEND	Natural gamma
7X	1	0	424.5	479.011	6	101	433.01	487.521	APPEND	Natural gamma
8X	1	0	434.2	488.811	5	102.9	441.229	495.84	TIE	Natural gamma
401-U1385L-										
10X	4	43.9	441.019	495.84	6	70	444.26	499.081	APPEND	Natural gamma
11X	1	0	445.8	500.077	7	52	455.18	509.457	APPEND	Natural gamma
12X	1	0	455.5	512.077	5	120	462.66	519.237	APPEND	Natural gamma
13X	1	0	465.2	521.677	6	126	473.79	530.267	APPEND	Natural gamma
14X	1	0	474.9	531.127	7	114	484.28	540.507	APPEND	Natural gamma
15X	1	0	484.6	540.927	7	89	494.07	550.397	APPEND	Natural gamma
16X	1	0	494.3	550.877	7	77	503.87	560.447	APPEND	Natural gamma
17X	1	0	504	560.827	7	70	512.84	569.667	APPEND	Natural gamma
18X	1	0	513.7	570.277	5	137	520.94	577.517	APPEND	Natural gamma
19X	1	0	523.4	578.277	7	52	532.43	587.307	APPEND	Natural gamma
20X	1	0	533.1	588.277	7	53	542.56	597.737	APPEND	Natural gamma
21X	1	0	542.8	598.827	7	53	552.19	608.217	APPEND	Natural gamma

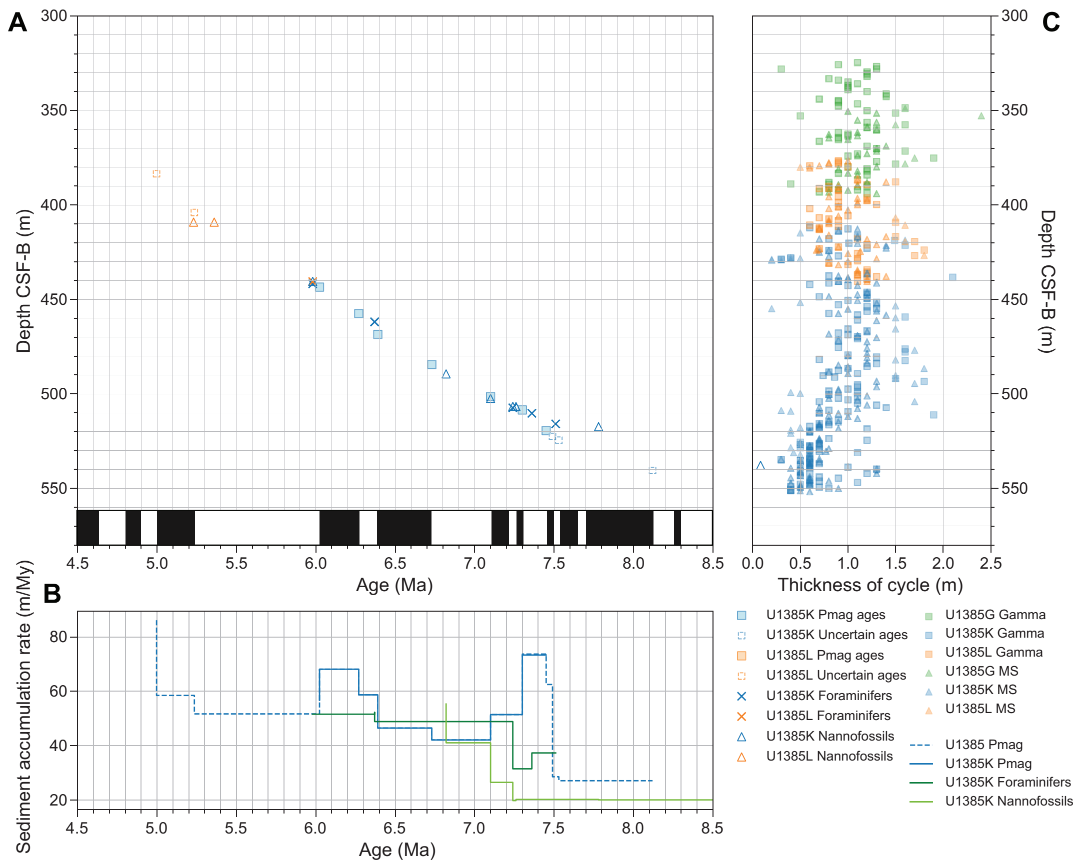

Figure F51. A. Age model tie points, Holes U1385K (blue) and U1385B (orange). B. Sedimentation accumulation rates for each data set (foraminifers, nannofossils, and paleomagnetism). C. Cycle thickness measured on both holes using MS and NGR core data. Only cycles not disturbed by section or core breaks were included in this data set.

Table T21. Top and bottom depth and calculated thickness of cycles in NGR and MS records, Holes U1385K and U1385L. **Download table in CSV format.**

References

Abrantes, F., 2000. 200,000 yr diatom records from Atlantic upwelling sites reveal maximum productivity during LGM and a shift in phytoplankton community structure at 185 000 yr. Earth and Planetary Science Letters, 176(1):7–16. **https://doi.org/10.1016/S0012-821X(99)00312-X**

Acton, G.D., Okada, M., Clement, B.M., Lund, S.P., and Williams, T., 2002. Paleomagnetic overprints in ocean sediment cores and their relationship to shear deformation caused by piston coring. Journal of Geophysical Research: Solid Earth, 107:2067–2081. **https://doi.org/10.1029/2001JB000518**

Ambar, I., Serra, N., Brogueira, M.J., Cabeçadas, G., Abrantes, F., Freitas, P., Gonçalves, C., and Gonzalez, N., 2002. Physical, chemical and sedimentological aspects of the Mediterranean outflow off Iberia. Deep Sea Research, Part II: Topical Studies in Oceanography, 49(19):4163–4177. **https://doi.org/10.1016/S0967-0645(02)00148-0**

Billups, K., 2002. Late Miocene through early Pliocene deep water circulation and climate change viewed from the sub-Antarctic South Atlantic. Palaeogeography, Palaeoclimatology, Palaeoecology, 185(3–4):287–307. **https://doi.org/10.1016/S0031-0182(02)00340-1**

Bulian, F., Jiménez-Espejo, F.J., Andersen, N., Larrasoaña, J.C., and Sierro, F.J., 2023. Mediterranean water in the Atlantic Iberian margin reveals early isolation events during the Messinian Salinity Crisis. Global and Planetary Change, 231:104297. **https://doi.org/10.1016/j.gloplacha.2023.104297**

de Castro, S., Hernández-Molina, F.J., de Weger, W., Jiménez-Espejo, F.J., Rodríguez-Tovar, F.J., Mena, A., Llave, E., and Sierro, F.J., 2021. Contourite characterization and its discrimination from other deep-water deposits in the Gulf of Cadiz contourite depositional system. Sedimentology, 68(3):987–1027. **https://doi.org/10.1111/sed.12813**

De Vleeschouwer, D., Dunlea, A.G., Auer, G., Anderson, C.H., Brumsack, H., de Loach, A., Gurnis, M.C., Huh, Y., Ishiwa, T., Jang, K., Kominz, M.A., März, C., Schnetger, B., Murray, R.W., Pälike, H., and Expedition 356 Shipboard Scientists, 2017. Quantifying K, U, and Th contents of marine sediments using shipboard natural gamma radiation spectra measured on DV JOIDES Resolution. Geochemistry, Geophysics, Geosystems, 18(3):1053–1064. **https://doi.org/10.1002/2016GC006715**

Dorador, J., and Rodríguez-Tovar, F.J., 2015. Application of digital image treatment to the characterization and differentiation of deep-sea ichnofacies. Spanish Journal of Palaeontology, 30(2):265–274. **https://doi.org/10.7203/sjp.30.2.17256**

Emerson, S., and Hedges, J.I., 1988. Processes controlling the organic carbon content of open ocean sediments. Paleoceanography, 3(5):621–634. **https://doi.org/10.1029/PA003i005p00621**

Expedition 339 Scientists, 2013. Site U1385. In Stow, D.A.V., Hernández-Molina, F.J., Alvarez Zarikian, C.A., and the Expedition 339 Scientists, Proceedings of the Integrated Ocean Drilling Program. 339: Tokyo (Integrated Ocean Drilling Program Management International, Inc.). **https://doi.org/10.2204/iodp.proc.339.103.2013**

Flecker, R., Ducassou, E., Williams, T., Amarathunga, U., Balestra, B., Berke, M.A., Blättler, C.L., Chin, S., Das, M., Egawa, K., Fabregas, N., Feakins, S.J., George, S.C., Hernández-Molina, F.J., Krijgsman, W., Li, Z., Liu, J., Noto, D., Raad, F., Rodríguez-Tovar, F.J., Sierro, F.J., Standring, P., Stine, J., Tanaka, E., Teixeira, M., Xu, X., Yin, S., and Yousfi, M.Z., 2025a. Expedition 401 methods. In Flecker, R., Ducassou, E., Williams, T., and the Expedition 401 Scientists, Mediterranean–Atlantic Gateway Exchange. Proceedings of the International Ocean Discovery Program, 401: College Station, TX (International Ocean Discovery Program). **https://doi.org/10.14379/iodp.proc.401.102.2025**

Flecker, R., Ducassou, E., Williams, T., and the Expedition 401 Scientists, 2025b. Supplementary material, **https://doi.org/10.14379/iodp.proc.401supp.2025**. In Flecker, R., Ducassou, E., Williams, T., and the Expedition 401 Scientists, Mediterranean–Atlantic Gateway Exchange. Proceedings of the International Ocean Discovery Program, 401: College Station, TX (International Ocean Discovery Program).

Glazkova, T., Hernández-Molina, F.J., Dorokhova, E., Mena, A., Roque, C., Rodríguez-Tovar, F.J., Krechik, V., Kuleshova, L., and Llave, E., 2022. Sedimentary processes in the Discovery Gap (Central–NE Atlantic): An example of a deep marine gateway. Deep Sea Research Part I: Oceanographic Research Papers, 180:103681. **https://doi.org/10.1016/j.dsr.2021.103681**

Gonthier, E.G., Faugères, J.-C., and Stow, D.A.V., 1984. Contourite facies of the Faro Drift, Gulf of Cadiz. Geological Society, London, Special Publications, 15(1):275–292. **https://doi.org/10.1144/GSL.SP.1984.015.01.18**

Gooday, A.J., 1993. Deep-sea benthic foraminiferal species which exploit phytodetritus: characteristic features and controls on distribution. Marine Micropaleontology, 22(3):187–205. **https://doi.org/10.1016/0377-8398(93)90043-W**

Hernández-Molina, F.J., de Castro, S., de Weger, W., Duarte, D., Fonnesu, M., Glazkova, T., Kirby, A., Llave, E., Ng, Z.L., Mantilla Muñoz, O., Rodrigues, S., Rodríguez-Tovar, F.J., Thieblemont, A., Viana, A.R., and Yin, S., 2022. Contourites and mixed depositional systems: A paradigm for deepwater sedimentary environments. In Rotzien, J.R., Yeilding, C.A., Sears, R.A., and Hernández-Molina, F.J., and Catuneanu, O. (Eds.), Deepwater Sedimentary Systems. Amsterdam (Elsevier), 301–360. **https://doi.org/10.1016/B978-0-323-91918-0.00004-9**

Hernández-Molina, F.J., Larter, R.D., and Maldonado, A., 2017. Neogene to Quaternary stratigraphic evolution of the Antarctic Peninsula, Pacific Margin offshore of Adelaide Island: Transitions from a non-glacial, through glacially-influenced to a fully glacial state. Global and Planetary Change, 156:80–111. **https://doi.org/10.1016/j.gloplacha.2017.07.002**

Hernández-Molina, F.J., Serra, N., Stow, D.A.V., Llave, E., Ercilla, G., and Van Rooij, D., 2011. Along-slope oceanographic processes and sedimentary products around the Iberian margin. Geo-Marine Letters, 31(5):315–341. **https://doi.org/10.1007/s00367-011-0242-2**

Hilgen, F.J., Bissoli, L., Iaccarino, S., Krijgsman, W., Meijer, R., Negri, A., and Villa, G., 2000a. Integrated stratigraphy and astrochronology of the Messinian GSSP at Oued Akrech (Atlantic Morocco). Earth and Planetary Science Letters, 182(3):237–251. **https://doi.org/10.1016/S0012-821X(00)00247-8**

Hilgen, F.J., Iaccarino, S., Krijgsman, W., Villa, G., Langereis, C.G., and Zachariasse, W.J., 2000b. The global boundary stratotype section and point (GSSP) of the Messinian Stage (uppermost Miocene). Episodes Journal of International Geoscience, 23(3):172–178.

Hodell, D., Lourens, L., Crowhurst, S., Konijnendijk, T., Tjallingii, R., Jiménez-Espejo, F., Skinner, L., Tzedakis, P.C., and the Shackleton Site Project Members, 2015. A reference time scale for Site U1385 (Shackleton Site) on the SW Iberian Margin. Global and Planetary Change, 133:49–64. **https://doi.org/10.1016/j.gloplacha.2015.07.002**

Hodell, D.A., Abrantes, F., and Alvarez Zarikian, C.A., 2022. Expedition 397 Scientific Prospectus: Iberian Margin Paleoclimate. International Ocean Discovery Program. **https://doi.org/10.14379/iodp.sp.397.2022**

Hodell, D.A., Abrantes, F., Alvarez Zarikian, C.A., and the Expedition 397 Scientists, 2023. Expedition 397 Preliminary Report: Iberian Margin Paleoclimate. International Ocean Discovery Program. **https://doi.org/10.14379/iodp.pr.397.2023**

Hodell, D.A., Abrantes, F., Alvarez Zarikian, C.A., Brooks, H.L., Clark, W.B., Dauchy-Tric, L.F.B., dos Santos Rocha, V., Flores, J.-A., Herbert, T.D., Hines, S.K.V., Huang, H.-H.M., Ikeda, H., Kaboth-Bahr, S., Kuroda, J., Link, J.M., McManus, J.F., Mitsunaga, B.A., Nana Yobo, L., Pallone, C.T., Pang, X., Peral, M.Y., Salgueiro, E., Sanchez, S., Verma, K., Wu, J., Xuan, C., and Yu, J., 2024a. Site U1385. In Hodell, D.A., Abrantes, F., Alvarez Zarikian, C.A., and the Expedition 397 Scientists, Iberian Margin Paleoclimate. Proceedings of the International Ocean Discovery Program, 397: College Station, TX (International Ocean Discovery Program). **https://doi.org/10.14379/iodp.proc.397.105.2024**

Hodell, D.A., Abrantes, F., Alvarez Zarikian, C.A., Brooks, H.L., Clark, W.B., Dauchy-Tric, L.F.B., dos Santos Rocha, V., Flores, J.-A., Herbert, T.D., Hines, S.K.V., Huang, H.-H.M., Ikeda, H., Kaboth-Bahr, S., Kuroda, J., Link, J.M., McManus, J.F., Mitsunaga, B.A., Nana Yobo, L., Pallone, C.T., Pang, X., Peral, M.Y., Salgueiro, E., Sanchez, S., Verma, K., Wu, J., Xuan, C., and Yu, J., 2024b. Site U1587. In Hodell, D.A., Abrantes, F., Alvarez Zarikian, C.A., and the Expedition 397 Scientists, Iberian Margin Paleoclimate. Proceedings of the International Ocean Discovery Pro-

gram, 397: College Station, TX (International Ocean Discovery Program).
https://doi.org/10.14379/iodp.proc.397.104.2024

Hodell, D.A., Williams, D.F., and Kennett, J.P., 1985. Late Pliocene reorganization of deep vertical water-mass structure in the western South Atlantic: faunal and isotopic evidence. Geological Society of America Bulletin, 96(4):495–503. **https://doi.org/10.1130/0016-7606(1985)96<495:LPRODV>2.0.CO;2**

Hüneke, H., and Henrich, R., 2011. Pelagic sedimentation in modern and ancient oceans. In Hüneke, H., and Mulder, T. (Eds.), Deep-Sea Sediments. Developments in Sedimentology, 63: 215–351. **https://doi.org/10.1016/B978-0-444-53000-4.00004-4**

Hüneke, H., Hernández-Molina, F.J., Rodríguez-Tovar, F.J., Llave, E., Chiarella, D., Mena, A., and Stow, D.A.V., 2021. Diagnostic criteria using microfacies for calcareous contourites, turbidites and pelagites in the Eocene–Miocene slope succession, southern Cyprus. Sedimentology, 68(2):557–592. **https://doi.org/10.1111/sed.12792**

Krijgsman, W., Gaboardi, S., Hilgen, F.J., Iaccarino, S., de Kaenel, E., and van der Laan, E., 2004. Revised astrochronology for the Ain el Beida section (Atlantic Morocco): No glacio-eustatic control for the onset of the Messinian Salinity Crisis. Stratigraphy, 1(1):87–101. **https://doi.org/10.29041/strat.01.1.05**

Li, Z., and Schieber, J., 2018. Detailed facies analysis of the upper Cretaceous Tununk Shale Member, Henry Mountains region, Utah: implications for mudstone depositional models in epicontinental seas. Sedimentary Geology, 364:141–159. **https://doi.org/10.1016/j.sedgeo.2017.12.015**

Lofi, J., Voelker, A.H.L., Ducassou, E., Hernández-Molina, F.-J., Sierro, F.J., Bahr, A., Galvani, A., Lourens, L.J., Pardo-Igúzquiza, E., Pezard, P., Rodríguez-Tovar, F.J., and Williams, T., 2016. Quaternary chronostratigraphic framework and sedimentary processes for the Gulf of Cadiz and Portuguese contourite depositional systems derived from natural gamma ray records. Marine Geology, 377:40–57. **https://doi.org/10.1016/j.margeo.2015.12.005**

Lourens, L., Hilgen, F., Shackleton, N.J., Laskar, J., and Wilson, D., 2004. The Neogene period. In Smith, A.G., Gradstein, F.M. and Ogg, J.G., A Geologic Time Scale 2004. Cambridge, UK (Cambridge University Press), 409–440. **https://doi.org/10.1017/CBO9780511536045.022**

MacEachern, J.A., Bann, K.L., Pemberton, S.G., Gingras, M.K., MacEachern, J.A., Bann, K.L., Gingras, M.K., and Pemberton, S.G., 2007. The Ichnofacies Paradigm: high-resolution paleoenvironmental interpretation of the rock record. In MacEachern, J.A., Bann, K.L., Gingras, M.K., and Pemberton, S.G. (Eds.), Applied Ichnology. SEPM Short Course Notes, 52: 27–64. **https://doi.org/10.2110/pec.07.52.0027**

Maestro, A., Bohoyo, F., López Martínez, Jerónimo, Acosta, J., Gómez-Ballesteros, M., Llave, E., Muñoz, A., Terrinha, P., Dominguez, M., and Fernández-Sáez, F., 2015. Influencia de los procesos tectónicos y volcánicos en la morfología de los márgenes continentales ibéricos. Boletín Geológico y Minero, 126(2–3):427–482. **http://hdl.handle.net/10486/678099**

Magill, C.R., Ausín, B., Wenk, P., McIntyre, C., Skinner, L., Martínez-García, A., Hodell, D.A., Haug, G.H., Kenney, W., and Eglinton, T.I., 2018. Transient hydrodynamic effects influence organic carbon signatures in marine sediments. Nature Communications, 9(1):4690. **https://doi.org/10.1038/s41467-018-06973-w**

Meyers, P.A., 1997. Organic geochemical proxies of paleoceanographic, paleolimnologic, and paleoclimatic processes. Organic Geochemistry, 27(5–6):213–250. **https://doi.org/10.1016/S0146-6380(97)00049-1**

Morigi, C., Negri, A., Giunta, S., Kouwenhoven, T., Krijgsman, W., Blanc-Valleron, M.-M., Orszag-Sperber, F., and Rouchy, J.-M., 2007. Integrated quantitative biostratigraphy of the latest Tortonian–early Messinian Pissouri section (Cyprus): an evaluation of calcareous plankton bioevents. Geobios, 40(3):267–279. **https://doi.org/10.1016/j.geobios.2007.02.002**

Nisancioglu, K.H., Raymo, M.E., and Stone, P.H., 2003. Reorganization of Miocene deep water circulation in response to the shoaling of the Central American Seaway. Paleoceanography, 18(1):1006–1018. **https://doi.org/10.1029/2002PA000767**

Raffi, I., Backman, J., Fornaciari, E., Pälike, H., Rio, D., Lourens, L., and Hilgen, F., 2006. A review of calcareous nannofossil astrobiochronology encompassing the past 25 million years. Quaternary Science Reviews, 25(23):3113–3137. **https://doi.org/10.1016/j.quascirev.2006.07.007**

Raffi, I., Wade, B.S., Pälike, H., Beu, A.G., Cooper, R., Crundwell, M.P., Krijgsman, W., Moore, T., Raine, I., Sardella, R., and Vernyhorova, Y.V., 2020. The Neogene Period. In Gradstein, F.M., Ogg, J.G., Schmitz, M.D., and Ogg, G. (Eds.), Geologic Time Scale 2020. (Elsevier), 1141–1215. **https://doi.org/10.1016/B978-0-12-824360-2.00029-2**

Rider, M.H., 1986. The Geological Interpretation of Well Logs: Houston, TX (Gulf Publishing Company).

Rodríguez-Tovar, F.J., 2022. Ichnological analysis: a tool to characterize deep-marine processes and sediments. Earth-Science Reviews, 228:104014. **https://doi.org/10.1016/j.earscirev.2022.104014**

Rodríguez-Tovar, F.J., and Dorador, J., 2014. Ichnological analysis of Pleistocene sediments from the IODP Site U1385 "Shackleton Site" on the Iberian margin; approaching paleoenvironmental conditions. Palaeogeography, Palaeoclimatology, Palaeoecology, 409:24–32. **https://doi.org/10.1016/j.palaeo.2014.04.027**

Ruttenberg, K.C., and Goñi, M.A., 1997. Phosphorus distribution, C:N:P ratios, and $\delta^{13}C_{oc}$ in arctic, temperate, and tropical coastal sediments: tools for characterizing bulk sedimentary organic matter. Marine Geology, 139(1):123–145. **https://doi.org/10.1016/S0025-3227(96)00107-7**

Schieber, J., Southard, J., and Thaisen, K., 2007. Accretion of mudstone beds from migrating floccule ripples. Science, 318(5857):1760–1763. **https://doi.org/10.1126/science.1147001**

Schönfeld, J., 1997. The impact of the Mediterranean Outflow Water (MOW) on benthic foraminiferal assemblages and surface sediments at the southern Portuguese continental margin. Marine Micropaleontology, 29(3):211–236. **https://doi.org/10.1016/S0377-8398(96)00050-3**

Schönfeld, J., 2002a. A new benthic foraminiferal proxy for near-bottom current velocities in the Gulf of Cadiz, northeastern Atlantic Ocean. Deep Sea Research, Part I: Oceanographic Research Papers, 49(10):1853–1875. **https://doi.org/10.1016/S0967-0637(02)00088-2**

Schönfeld, J., 2002b. Recent benthic foraminiferal assemblages in deep high-energy environments from the Gulf of Cadiz (Spain). Marine Micropaleontology, 44(3):141–162. **https://doi.org/10.1016/S0377-8398(01)00039-1**

Schönfeld, J., and Zahn, R., 2000. Late Glacial to Holocene history of the Mediterranean Outflow. Evidence from benthic foraminiferal assemblages and stable isotopes at the Portuguese margin. Palaeogeography, Palaeoclimatology, Palaeoecology, 159(1–2):85–111. **https://doi.org/10.1016/S0031-0182(00)00035-3**

Stow, D., and Smillie, Z., 2020. Distinguishing between deep-water sediment facies: turbidites, contourites and hemipelagites. Geosciences, 10(2):68. **https://doi.org/10.3390/geosciences10020068**

Stow, D.A.V., and Faugères, J.C., 2008. Contourite facies and the facies model. In Rebesco, M., and Camerlenghi, A. (Eds.), Contourites. Developments in Sedimentology, 60: (Elsevier), 223–256. **https://doi.org/10.1016/S0070-4571(08)10013-9**

Sykes, T.J.S., Ramsay, A.T.S., and Kidd, R.B., 1998. Southern hemisphere Miocene bottom-water circulation: a palaeobathymetric analysis. Geological Society, London, Special Publications, 131(1):43–54. **https://doi.org/10.1144/GSL.SP.1998.131.01.03**

Szarek, R., Nomaki, H., and Kitazato, H., 2007. Living deep-sea benthic foraminifera from the warm and oxygen-depleted environment of the Sulu Sea. Deep Sea Research Part II: Topical Studies in Oceanography, 54(1):145–176. **https://doi.org/10.1016/j.dsr2.2006.02.017**

Terrinha, P., Pinheiro, L.M., Henriet, J.P., Matias, L., Ivanov, M.K., Monteiro, J.H., Akhmetzhanov, A., Volkonskaya, A., Cunha, T., Shaskin, P., and Rovere, M., 2003. Tsunamigenic-seismogenic structures, neotectonics, sedimentary processes and slope instability on the southwest Portuguese Margin. Marine Geology, 195(1):55–73. **https://doi.org/10.1016/S0025-3227(02)00682-5**

Thomson, J., Nixon, S., Summerhayes, C.P., Schönfeld, J., Zahn, R., and Grootes, P., 1999. Implications for sedimentation changes on the Iberian margin over the last two glacial/interglacial transitions from (230Thexcess)0 systematics. Earth and Planetary Science Letters, 165(3):255–270. **https://doi.org/10.1016/S0012-821X(98)00265-9**

Traykovski, P., Geyer, W.R., Irish, J.D., and Lynch, J.F., 2000. The role of wave-induced density-driven fluid mud flows for cross-shelf transport on the Eel River continental shelf. Continental Shelf Research, 20(16):2113–2140. **https://doi.org/10.1016/S0278-4343(00)00071-6**

Uenzelmann-Neben, G., Weber, T., Grützner, J., and Thomas, M., 2017. Transition from the Cretaceous ocean to Cenozoic circulation in the western South Atlantic — a twofold reconstruction. Tectonophysics, 716:225–240. **https://doi.org/10.1016/j.tecto.2016.05.036**

van Aken, H.M., 2000. The hydrography of the mid-latitude northeast Atlantic Ocean: I: The deep water masses. Deep Sea Research Part I: Oceanographic Research Papers, 47(5):757–788. **https://doi.org/10.1016/S0967-0637(99)00092-8**

Yawar, Z., and Schieber, J., 2017. On the origin of silt laminae in laminated shales. Sedimentary Geology, 360:22–34. **https://doi.org/10.1016/j.sedgeo.2017.09.001**

Zhu, X., 2001. Characteristics of Uvigerina in the northwestern Indian Ocean: paleo-environmental implications. Chinese Science Bulletin, 46(1):116–119. **https://doi.org/10.1007/BF03187250**